Measurement of the Momentum Spectrum of Cosmic Ray Muons at a depth of 320 mwe

DISSERTATION
zur Erlangung des akademischen Grades eines
Doktors der Naturwissenschaften

vorgelegt von
M.Sc. Nadir Omar Hashim
aus Mombasa-Kenia

genehmigt vom Fachbereich Physik
der Universität Siegen

Siegen Juni 2007

Gutachter der Dissertation: Prof. Dr. Claus Grupen
Siegen University, Siegen

Prof. Dr. Michael Schmelling
Max-Planck-Institute for Nuclear Physics
Heidelberg

Tag der mündlichen Prüfung: 22.06.2007

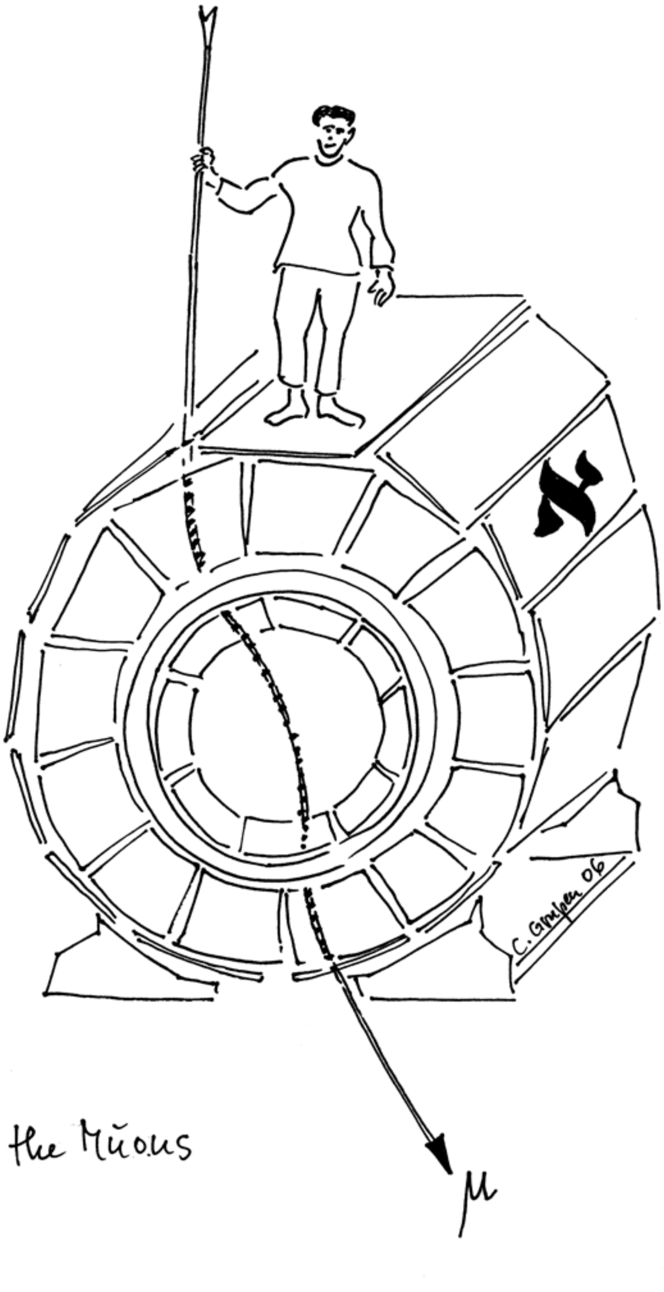

Master of the Mŭons

To my family

Abstract

Cosmic ray muons are produced through interactions of primary cosmic radiation in the atmosphere. They are a component of extensive air showers which can also be measured underground. The CosmoALEPH experiment used the ALEPH detector at the European Centre for Particle Physics, CERN, to measure cosmic ray muon events at a depth of 320 mwe underground. Measurements of the momentum spectrum and charge ratio of the cosmic ray muons are presented in this work. The results are compared with the expectations from MC simulations based on different hadronic interaction models.

Contents

Chapter 1

Introduction

In this Chapter a brief introduction to the presence of cosmic radiation and the measurement of cosmic ray muons by CosmoALEPH.

1.1 Cosmic Radiation

Great progress has been made in recent years towards understanding the Universe, the galactic and extra-galactic spaces, what they are made of, the kind of radiation environments they offer and so on. Although alot is known about the Universe, there are still *'mysteries'* yet to be understood. The current technology, however, does not allow direct observation of all the phenomena in the entire Universe. The main limitation is due to the vast distances and the very low energies involved, for example the extremely low energy neutrinos from the *Big Bang*. The radiation, known as *'cosmic microwave background radiation'*, carries a lot of information about the processes in the Universe. Interpreting this information is the subject of *'cosmology'* and it enables one to understand the very beginnings of the Universe and also to speculate on the possible fate of the Universe.

Since the discovery of cosmic rays [1] the field of cosmic ray physics has rapidly advanced, particularly towards the understanding of the origin of the most highly energetic particles that constitute primary cosmic rays, their interaction processes in the galactic and extra galactic media, and also in the Earth's atmosphere [2].

The interaction of the primary cosmic ray particles in the Earth's atmosphere leads to the production of a cascade of secondary particles or Extensive Air Showers (EAS) with various components - hadronic, muonic and electromagnetic components (Figure 1.1). There are a variety of theoretical models to describe these interactions [3].

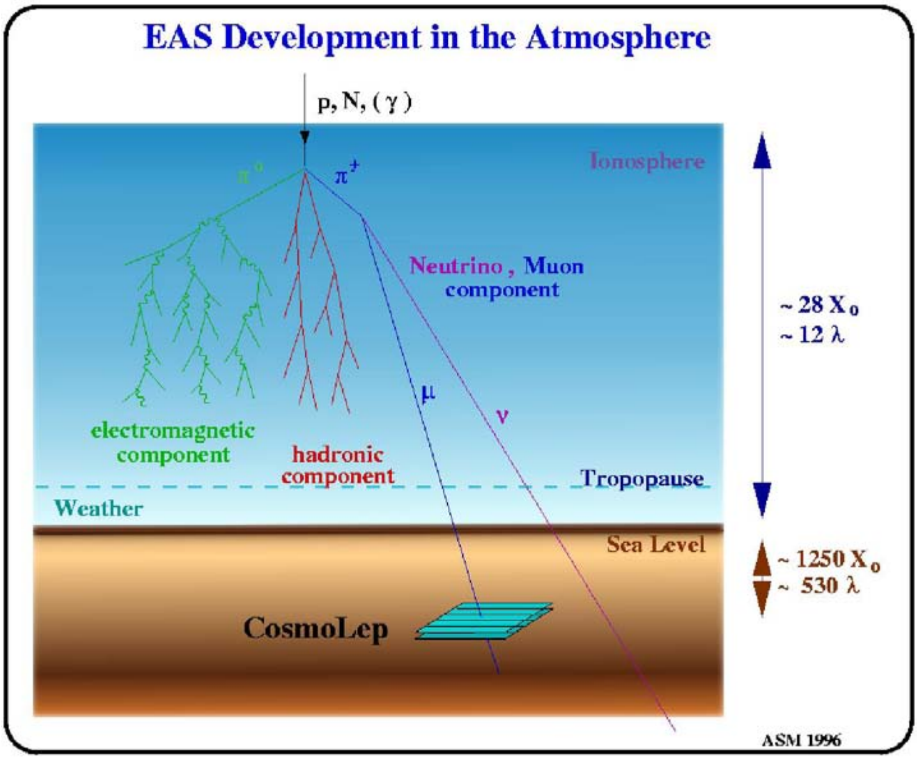

Figure 1.1: Development of extensive air showers in the atmosphere [4]. X_0 represents the radiation lengths, while λ represents the interaction lengths.

The measurement of cosmic radiation can be done either through the measurement of the primary or the secondary cosmic radiation. This can be achieved at some altitudes, on the Earth's surface or even at some underground depths. Many cosmic ray experiments have used a combination of the observables or components of the EAS, both on the Earth's surface and underground, to measure the cosmic radiation. These measurements provide, for example, an understanding of the hadronic interactions and also shed some light on the chemical composition of the primary particles.

The cosmic ray muon flux, which is also a component of the EAS, provides a useful tool for the calculations of neutrino fluxes, which are rather difficult to measure directly. Together with the other EAS components, the muon flux also enables reconstruction of the EAS and they can serve as a test of the various theoretical models that describe the hadronic interactions of the cosmic ray particles.

1.2 Cosmic ray Muons in ALEPH

The ALEPH[1] together with the L3, DELPHI and OPAL detectors were constructed for experiments on electron - positron collisions in the LEP[2] ring at the European Laboratory for Particle Physics, CERN. This was a powerful tool for the observations of, for example the processes,

$$e^+ + e^- \rightarrow l^+ + l^- \; (l = e, \mu, \tau) \,, \tag{1.1}$$

$$e^+ + e^- \rightarrow \text{hadrons} \,, \tag{1.2}$$

$$e^+ + e^- \rightarrow Z^o \,, \tag{1.3}$$

and, with an on-shell Z^o the decays,

$$Z^o \rightarrow q + \bar{q} \rightarrow \text{hadrons} \,, \tag{1.4}$$

$$Z^o \rightarrow \nu_l + \bar{\nu}_l \; (l = e, \mu, \tau) \,, \tag{1.5}$$

$$Z^o \rightarrow l^+ + l^- \; (l = e, \mu, \tau) \tag{1.6}$$

which include some final state muons. A display of such events in the ALEPH apparatus is shown in Figure 1.2. The Z-boson in Figure 1.2(a) decays into a quark-antiquark pair leading to the observation of jets of hardons. The events are graphically illustrated using the special software program, DALI[3] [6, 7]. This is a program for the visualisation of the events detected in ALEPH and has formed the basis of event displays for future high-energy physics experiments, for example the ATLAS[4] currently being built at the CERN's Large Hadron Collider (LHC).

---

[1] **A**pparatus for **LE**P **PH**ysics

[2] **L**arge **E**lectron **P**ositron collider

[3] **D**isplay of **AL**EPH **I**nteractions

[4] **A** **T**oroidal **L**HC **A**pparatu**S**

The ALEPH apparatus was capable of measuring muon momentum and direction with high precision. Cosmic ray muons were also observed in many instances, an early event dating back to 1989 was named as a *'cosmic debugger'* [10]. This was a cosmic ray muon event with a high multiplicity (≥ 100) that enabled one to identify detector modules that did not respond to the event. An example of a similar cosmic ray muon event with a high muon multiplicity is shown in Figure 1.3. Such events led to the conception of the CosmoLEP experiment with the main aim to search for correlations of EAS. The CosmoALEPH experiment, which was the pilot experiment in CosmoLEP [5, 8], used the ALEPH apparatus together with some scintillator stations to measure the muon component of EAS. Preliminary results [11, 12, 13] have recently shown that the momentum spectrum and charge ratio for cosmic muons measured by CosmoALEPH are consistent with the a recent compilation of the cosmic ray muon data [14].

The performance of the ALEPH apparatus to measurement of cosmic ray muon events is studied in this work. The aim is to measure the momentum spectrum and charge ratio of the cosmic ray muons detected. This thesis is organised as follows; Chapter 2 provides a brief description of cosmic ray muons - their production in the atmosphere and propagation underground. The CosmoALEPH experimental set-up is briefly described in Chapter 3. The study on the performance of the ALEPH apparatus is presented in Chapter 4, while Chapter 5 describes the data analysis techniques to unfold the effects of smearing on the momentum measurements due to detector resolution. The momentum spectrum and charge ratio measured in this work is presented in Chapter 6. A comparison is made with the results of previous measurements and also the predictions of the hadronic interaction models. A summary of the main results of this work is presented in Chapter 7.

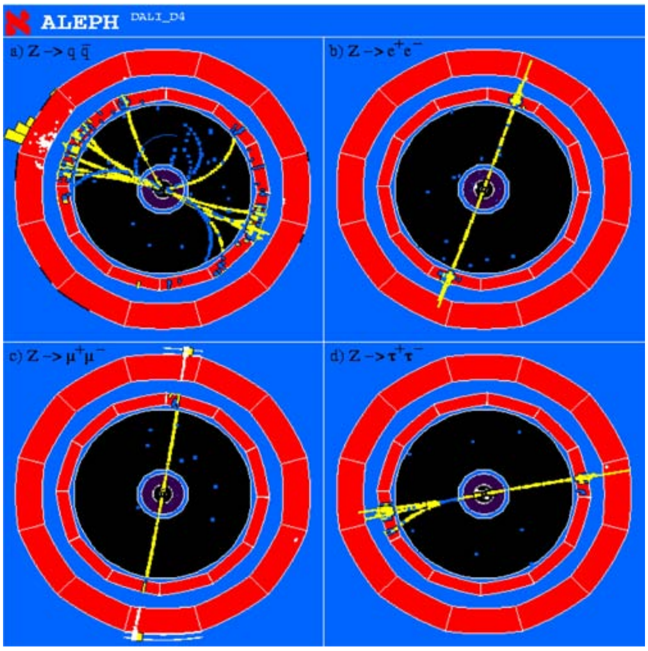

Figure 1.2: Display of e + e− interactions in ALEPH [6].

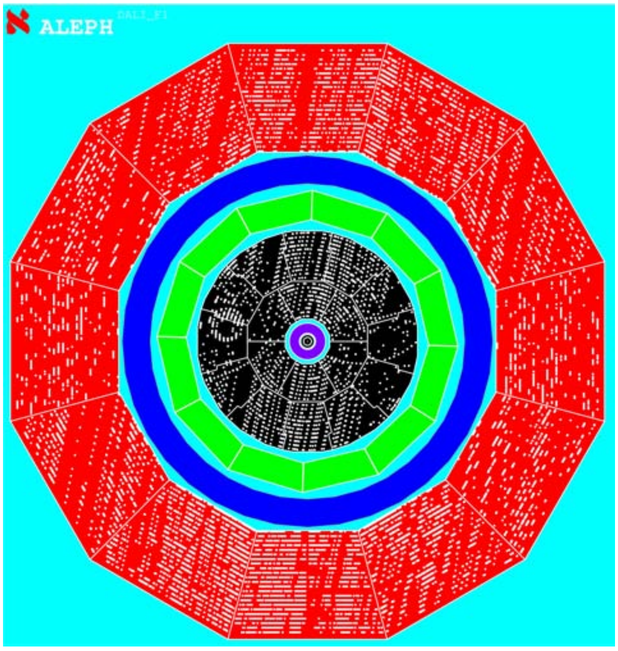

Figure 1.3: A cosmic ray multi-muon event in ALEPH [6].

Chapter 2

Cosmic Ray Particles

A brief account of cosmic ray particles and their interactions in the Earth's atmosphere is given in this Chapter.

2.1 Primary and Secondary Cosmic Radiation

The term *primary cosmic radiation* refers to the cosmic rays that reach the Earth's atmosphere from outer space. These include, among others, energetic photons, neutrinos and charged particles. The charged component of the primary cosmic radiation constitutes mainly protons ($\approx$ 85%) and α particles ($\approx$ 12%). A further 3% consists of particles with nuclear charge $Z \geq 3$.

The interaction of the primary cosmic ray particles leads to the production of secondary cosmic ray particles or *secondary cosmic radiation.* For example, a primary proton can interact with a nucleus in the Earth's atmosphere to produce pions,

$$p + \text{ nucleus } \rightarrow \pi^+ + \pi^- + \pi^0 + \text{ anything}\,, \tag{2.1}$$

which in turn decay to produce muons, neutrinos and photons,

$$\pi^+ \rightarrow \mu^+ + \nu_\mu\,, \tag{2.2}$$

$$\pi^- \rightarrow \mu^- + \bar{\nu}_\mu\,, \tag{2.3}$$

$$\pi^0 \rightarrow \gamma + \gamma. \tag{2.4}$$

Similar processes occur in the decay of kaons producing muons with high momenta. These cosmic ray muons decay into electrons and neutrinos,

$$\mu^+ \rightarrow e^+ + \nu_e + \bar{\nu}_\mu \,, \tag{2.5}$$

$$\mu^- \rightarrow e^- + \bar{\nu}_e + \nu_\mu . \tag{2.6}$$

Such cosmic ray muons follow closely the direction of the incident protons and constitute the bulk of the *down-going* cosmic ray muons. In some cases, energetic primary neutrinos can interact with the (primary) protons or neutrons to produce the so-called *neutrino-induced* cosmic ray muons,

$$\nu_\mu + n \rightarrow \mu^- + p \,, \tag{2.7}$$

$$\bar{\nu}_\mu + p \rightarrow \mu^+ + n \,. \tag{2.8}$$

The neutrino-induced cosmic ray muons are usually observed as *up-going* cosmic ray muons through the Earth. There are experiments, for example AMANDA[1], which measure the up-going muons. These events are rare but they provide information on the atmospheric neutrino flux and indeed *neutrino oscillations*. The *down-going* neutrino-induced muons are not easy to identify because of the rather large background of atmopsheric muons.

2.2 The Cosmic Ray Energy Spectrum

Figure 2.1 shows the all particle cosmic ray energy spectrum [15]. The low-energy particles $E \leq 10^{15}$ eV originate mostly from within the Galaxy while the particles at the highest energies are of extra-galactic origin. The cosmic ray flux can be described by,

$$\frac{\mathrm{d}N}{\mathrm{d}E} \sim E^{-\gamma}. \tag{2.9}$$

The parameter γ is sensitive to the chemical composition of the primary particles and it describes the slope of the all-particle cosmic ray energy spectrum, which is shown in Figure 2.1.

---

[1] **A**ntarctic **M**uon **A**nd **N**eutrino **D**etector **A**rray

The slope of the spectrum changes from -2.7 to -3.0 at energies above 10^{15} eV . This is known as the *'knee'* of the spectrum. A further change in the slope occurs at about 10^{19} eV, and this is known as the *'ankle'* on the spectrum. In order to illustrate these features, it is common to scale data on the all-particle spectrum as shown on the Figures 2.1 and 2.2.

There are several experiments that have measured the energy spectrum in the knee of the of cosmic ray spectrum [19, 21]. However, the chemical composition of the cosmic ray particles around and above the knee region is not well understood. Many attempts have been made to explain the knee and this is very sensitive to the chemical composition and indeed the sources of the cosmic rays at these energies [16, 17, 18]. The KASCADE[1] experiment [20] has measured cosmic ray particles in the region of the knee on the cosmic ray spectrum. The knee is considered to be due to different light and also heavy primary cosmic ray particles [24]. There are several models to explain this feature of the spectrum. The models refer to the chemical composition of the particles, their acceleration and propagation in the galactic space. For example, the *poly-gonato* model for the knee of the cosmic ray spectrum, the contribution of the chemical elements and their respective solar modulations are taken into account [16]. This is illustrated on Figure 2.3.

Just below the knee, the spectrum is dominated by a light composition, while just beyond the knee, the heavier elements dominate the spectrum. Particles beyond the ankle are believed to be of extra-galactic origin. Protons with energies greater than 6×10^{19} eV are likely to interact with photons of the *cosmic microwave background* $\gamma_{2.7K}$, via photo-pion production,

$$p \, + \, \gamma_{2.7K} \, \rightarrow \, n \, + \, \pi^{+} \, , \tag{2.10}$$

$$p \, + \, \gamma_{2.7K} \, \rightarrow \, p \, + \, \pi^{0} \, , \tag{2.11}$$

or pair-production,

$$p \, + \, \gamma_{2.7K} \, \rightarrow \, p \, + \, e^{+} \, + \, e^{-} \, , \tag{2.12}$$

losing a large fraction of their energy.

---

[1] **KA**rlsruhe **S**hower **C**ore and **A**rray **DE**tector

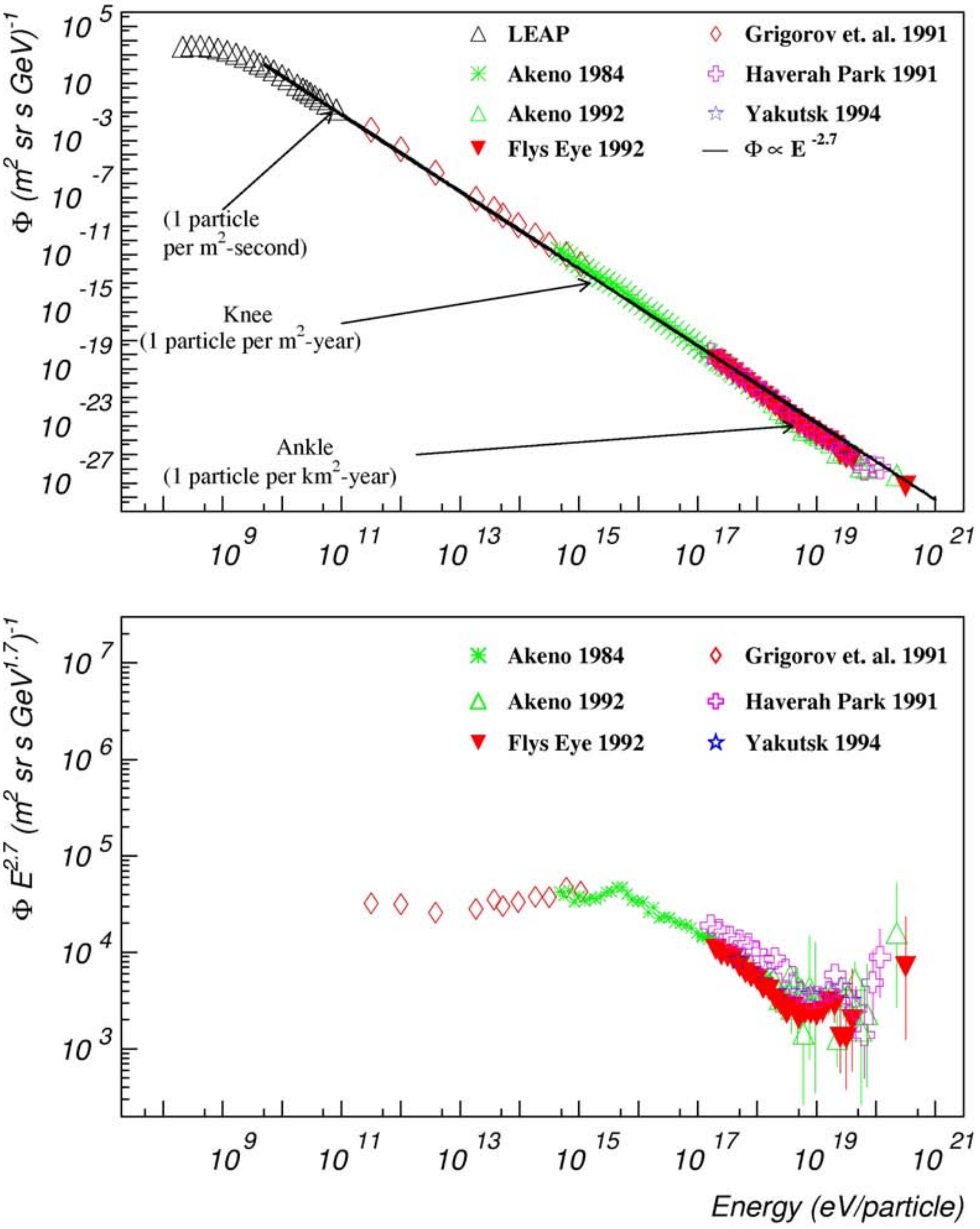

Figure 2.1: The all - particle cosmic energy ray spectrum. The data are scaled with $E^{2.7}$ in order to illustrate the changes in the slope of the spectrum, i.e at the *knee* and *ankle*. The data and the original version of this illustration are available from [15]
$http://astroparticle.uchicago.edu/cosmic\_ray\_spectrum\_picture.htm$

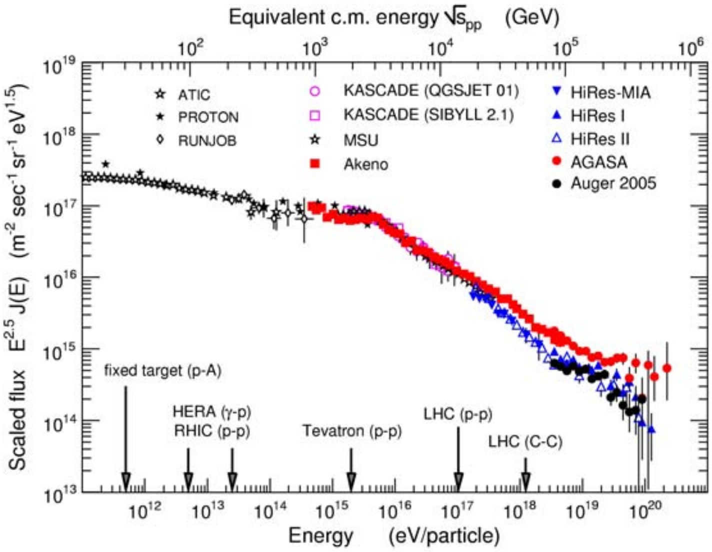

Figure 2.2: The primary cosmic ray flux[3]. The data are scaled with $E^{2.5}$. The references are contained in [3].

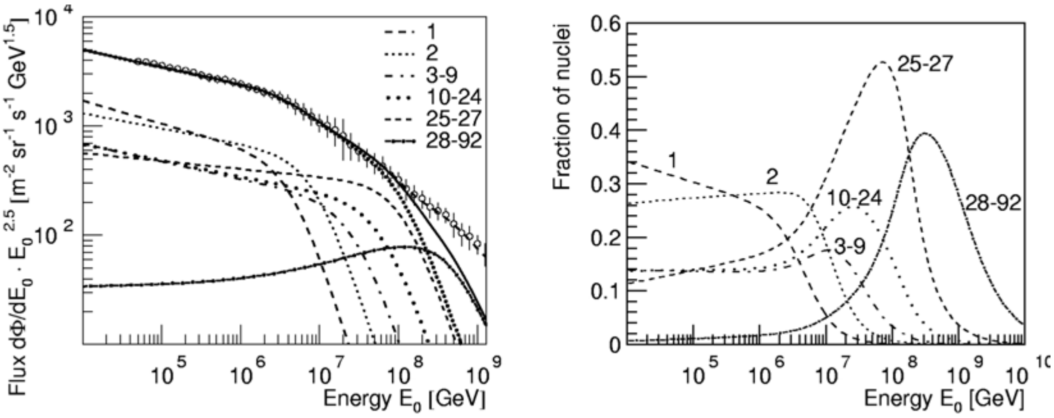

Figure 2.3: The flux and chemical composition in the knee of the cosmic ray spectrum according to the *poly-gonato* model [25]. The elemental contributions to the knee are indicated by the nuclear charge numbers.

Heavier nuclei of mass A suffer photo-disintegration,

$$A + \gamma_{2.7K} \rightarrow (A - 1) + N\,, \tag{2.13}$$

$$A + \gamma_{2.7K} \rightarrow (A - 2) + 2N\,, \tag{2.14}$$

or pair-production,

$$A + \gamma_{2.7K} \rightarrow A + e^{+} + e^{-}\,, \tag{2.15}$$

where N is a nucleon. These processes lead to a drastic cut-off on the cosmic ray energy spectrum at those energies and is known as the GZK[1] cut-off [26, 27].

Recent measurements by the AGASA[2] and HiRes[3] experiments provided conflicting data for cosmic ray particles at the highest energies. Results from the AGASA experiment are a hint to the existence of highly energetic particles beyond the GZK cut-off contrary to the other experimental data. The discrepancy is probably related to the differences in the measurement techniques. The AGASA experiment uses an array of surface detectors while the HiRes experiment uses fluorescence techniques.

Cosmic ray data at energies beyond 10^{19} eV have rather large statistical uncertainties making it difficult to model the mass composition, the sources of these particles and indeed the interaction mechanisms [28]. A combination of both galactic and extra-galactic sources provides reasonable fit of the existing data at those energies, which is not sensitive to the energy scales of the experiments[29].

The currently largest astrophysics experiment, the AUGER[4] observatory is a hybrid combination of a very large array of surface detectors and fluorescence detectors [30]. The observatory is designed to cover an area of about 3000 km^2 with an acceptance of 7200 km^2 sr for zenith angles up to 65^0 [31]. This makes it possible to detect cosmic ray particles at the highest energies, i.e. *Ultra -High Energy Cosmic Rays* (UHECR) with high statistics.

---

[1] **G**reisen-**Zatsepin**-**K**uzmin

[2] **A**keno **G**iant **A**ir **S**hower **A**rray

[3] **Hi**gh **Res**olution Flys's Eye Detector

[4] Pierre Auger Observatory

Construction of the AUGER observatory is at an advanced stage and the first results [33] are consistent with the other data as illustrated in Figure 2.2. Such large detector arrays should be able to provide further tests to the existence of the GZK cut-off and also the orgin of the highest energy cosmic ray particles.

2.3 Cosmic Ray Muons in the Atmosphere

Cosmic ray muons are produced by the interaction of primary cosmic ray particles in the Earth's atmosphere. For the understanding of these interactions and the subsequent propagation of the particles produced, the atmospheric depth X, measured in g/cm^2 is defined as;

$$X = \int_{h_{\text{obs.}}}^{\infty} \rho(h)\,\mathrm{d}h\,, \tag{2.16}$$

where $h_{\text{obs.}}$ is the observation level and $\rho(h)$ is the altitude dependent atmospheric density in g/cm^3. Assuming a constant atmospheric temperature, the relationship between the atmospheric depth X and the altitude h can simply be expressed as;

$$X = X_0 \exp(-h/h_0)\,, \tag{2.17}$$

where $X_0 = 1.03\,g/cm^2$ is the atmospheric depth at sea level and h_0 is the scale height in the atmosphere [22]. A more accurate description of the atmospheric depth takes into account the variation of atmopheric temperature with altitude. For zenith angles $\theta \leq 60^0$ the atmospheric depth is scaled with cos θ, giving the *slant depth*. This is the flat-Earth approximation. The curvature of the Earth has to be accounted for when calculating the atmospheric depth and/or modelling the atmospheric parameters for particles at large zenith angles. The interpretation of experimental results from air shower measurements requires a correct description of the atmospheric profiles and indeed the atmospheric conditions during the data taking. See for example, the detailed study of the atmospheric conditions for the AUGER observatory [32].

2.3.1 The Flux of Cosmic Ray Muons

The cosmic ray particles interact with air molecules as they propagate in the Earth's atmosphere. Their *mean free path* λ_{int} is given by,

$$\lambda_{int} = \frac{m_{air}}{\sigma_{int}} \quad (\mathrm{g/cm^2})\,, \tag{2.18}$$

where m_{air} is the average atomic weight of air molecules and σ_{int} is the interaction cross section in the atmosphere. This cross section includes all possible interactions. The probability of a particle to traversing the atmosphere without the interactions is given by,

$$P_{int} \sim e^{-\frac{\lambda}{\lambda_{int}}} \tag{2.19}$$

where λ is the atmospheric layer traversed. Using the appropriate transport equations and taking into account the mean free paths, an analytical approximation can be developed for the flux of the particles and also their respective secondaries in the atmosphere.

The production spectrum $P_j(E_j, X)$ for particles of type j with energy E_j at a depth X is expressed as the sum of all contributions from the decay of particles of type i [22, 23],

$$P_j(E_j, X) = \sum_i \int_{E_j(min.)}^{E_j(max.)} \frac{dg_{i,j}\,(E_j, E_i)}{dE_j}\, D_i(E_i, X)\, dE_i \tag{2.20}$$

where $dg_{i,j}\,(E_j, E_i)/dE_j$ is the spectrum of the particles of type j from the decay of particles of type i with energy E_i and $D_i(E_i, X)$ is the spectrum of the decaying particles of type i.

Assuming a primary proton flux of $1.8E^{-2.7}(\mathrm{cm^2\,s\,sr\,GeV})^{-1}$, and considering the production of muons from the two-body decays of pions and kaons, this approach yields an analytical form of the muon spectrum [23, 38],

$$\frac{\mathrm{dN}_\mu}{\mathrm{dE}_\mu} \simeq \frac{0.14}{\mathrm{cm^2\,s\,sr\,GeV}}\, \mathrm{E}_\mu^{-2.7} \left(\frac{1}{1 + \frac{1.1\,\mathrm{E}_\mu \cos\theta}{115\,\mathrm{GeV}}} + \frac{0.054}{1 + \frac{1.1\,\mathrm{E}_\mu \cos\theta}{850\,\mathrm{GeV}}} \right) \tag{2.21}$$

where the contributions from pion and kaon decays are given by the two terms in the square brackets respectively.

At the critical energy of 115 GeV for the charged pions and 850 GeV for the charged kaons, these particles have a probability of 1/2 to decay. At low energies, muons lose a large fraction of their energies due to ionisation, which is not accounted for in this approximation. Therefore the Equation 2.21 is only valid for the high energy muons which lose rather smaller fractions of their energies as they propagate in the Earth's atmosphere. Another parameterisation of the muon flux is of the form [62],

$$D_\mu(p, \theta \approx 0^\circ) = C \cdot p^{-(\gamma_0 + \gamma_1 \log p + \gamma_2 \log^2 p + \gamma_3 \log^3 p)} \tag{2.22}$$

with fit parameters shown in Table 2.1. This is a semi-analytical fit of numerical calculations of the muon flux at sea level taking into account the energy-dependent discrete and continuous energy losses for vertical muons.

Table 2.1: Fit parameters to calculate the muon flux at the Earth's surface using Equation 2.22 [62]

Momentum range (GeV/c)	C $(\text{cm}^2\ \text{s sr GeV})^{-1}$	γ_0	γ_1	γ_2	γ_3
$1 - 930$	$2.95 \cdot 10^{-3}$	0.3061	1.2743	-0.263	0.0252
$930 - 1590$	$1.781 \cdot 10^{-2}$	1.791	0.304		
$1590 - 4.2 \cdot 10^5$	$1.435 \cdot 10^1$	3.672			
$> 4.2 \cdot 10^5$	10^3	4			

Figure 2.4 illustrates a comparison of the above parameterisations for the cosmic ray muon flux. Both forms of the parameterisations are in good agreement for muon energies greater than 200 GeV.

The form of the muon flux described by Equation (2.22) is favoured as a standard reference spectrum in a recent compilation of cosmic ray muon data [14] as illustrated in Figure 2.5.

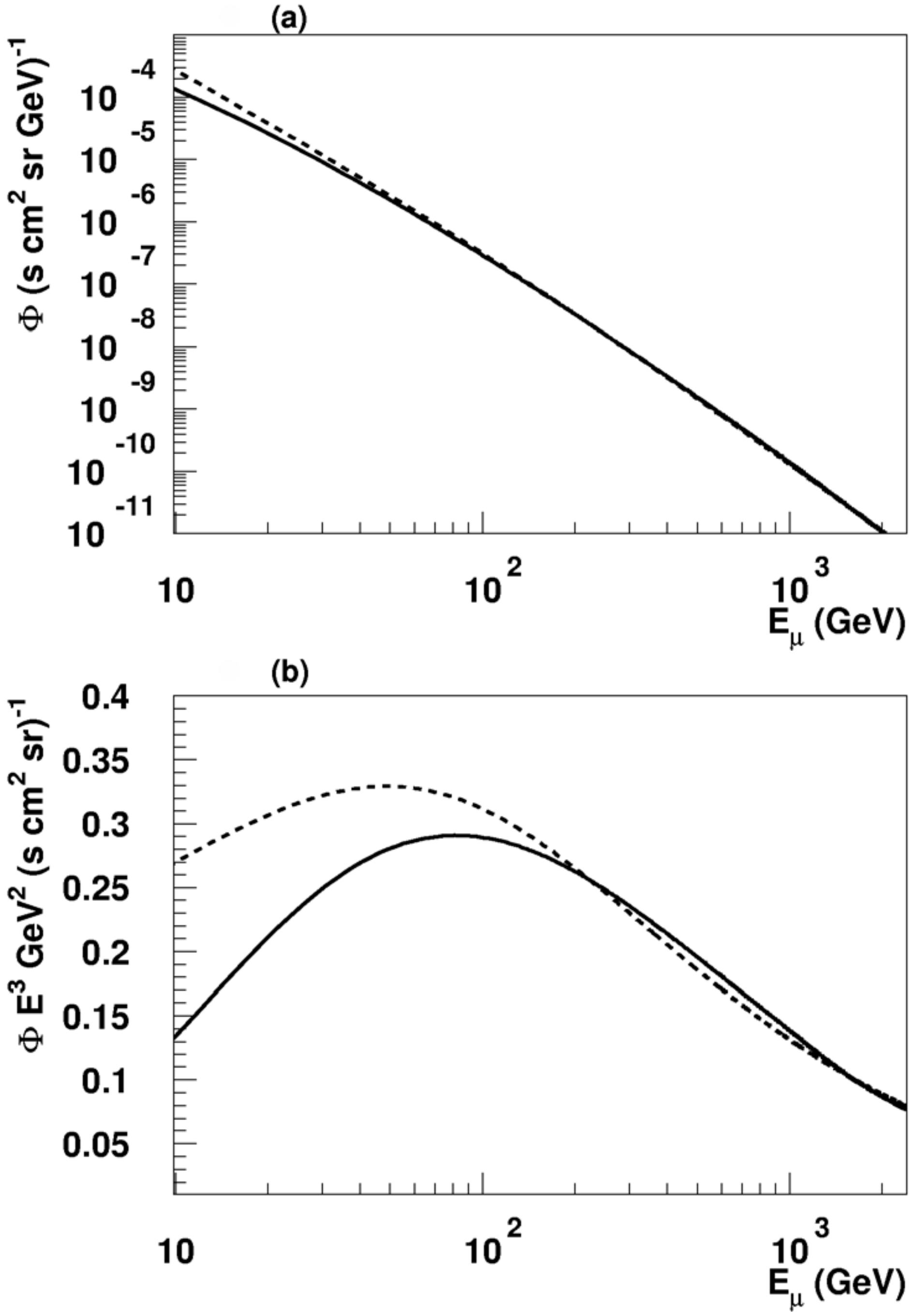

Figure 2.4: Approximation of the cosmic ray muon flux. The approximations are for vertical muons, i.e. $\theta = 0^0$. The solid and dashed lines illustrate the analytical forms described by the Equations 2.22 and 2.21 respectively. The flux on Figure (b) is scaled with E^3.

The parameterisation of the data set considered in the compilation of cosmic ray muon data shown in Figure 2.5, is of the form [14],

$$F(p) = C \cdot 10^{H(y)} \, (\mathrm{m}^2 \, \mathrm{sr} \, \mathrm{s} \, \mathrm{GeV/c})^{-1} \tag{2.23}$$

with

$$\begin{aligned} H(y) &= H_1 \cdot (y^3/2 - 5y^2/2 + 3y) \\ &+ H_2 \cdot (-2y^3/3 + 3y^2 - 10y/3 + 1) \\ &+ H_3 \cdot (y^3/6 - y^2/2 + y/3) \\ &+ S_2 \cdot (y^3/3 - 2y^2 + 11y/3 - 2) \\ y &= lg(p) \end{aligned}$$

The fit variables H_1, H_2 and H_3 represent the logarithm of the differential flux at 10, 100 and 1000 GeV, S_2 represents the exponent of the differential flux at 100 GeV.

The data reported for muon momenta beyond 200 GeV/c are scarce and associated with large uncertainties. There is therefore a need for high quality measurements at those energies. This will not only be useful for the parameterisations of experimental data but also for the theoretical description of the production of cosmic ray muons.

2.3.2 The Charge Ratio of Cosmic Ray Muons

Since protons constitute the main part of primary cosmic rays, it follows therefore that more positively charged particles are produced in the primary interactions. This is manifested by an excess of positively charged secondary particles. The muon charge ratio defined as,

$$R_\mu = \frac{N_{\mu^+}}{N_{\mu^-}} \tag{2.24}$$

indicates an excess of positive pions produced in EAS. Figure 2.6 shows a recent compilation of the cosmic ray charge ratio [14].

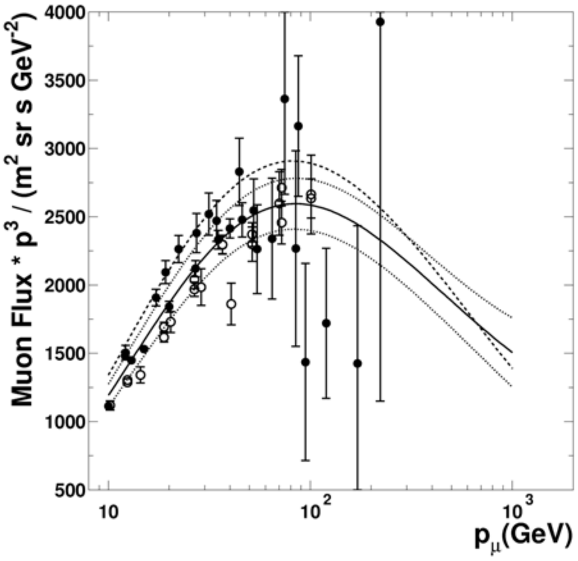

Figure 2.5: Parameterisation of cosmic ray muon data [14]. The solid line represents a fit of all the data points and the dotted lines indicate the uncertainty in the fit as described in [14]. The dashed line represents the parameterisation of the muon flux [62] as described by Equation 2.22.

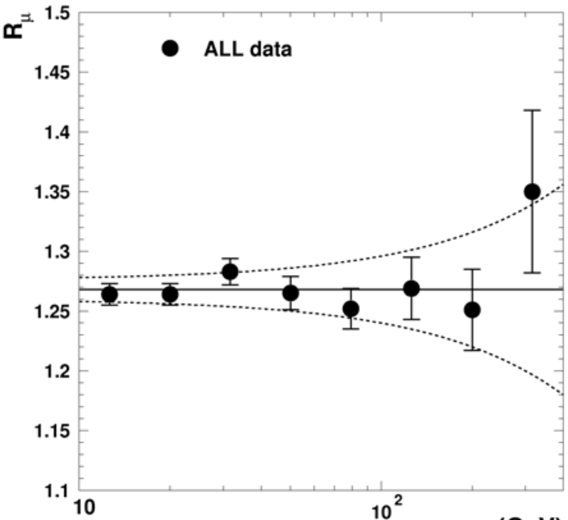

Figure 2.6: Parameterisation of the charge ratio of cosmic ray muons [14].

The parameterisation of the charge ratio in Figure 2.6, based on a sample of the cosmic ray muon data compiled in [14] is of the form,

$$R_\mu = 1.268 \pm [0.008 + 0.0002 \cdot p/\mathrm{GeV/c}] \tag{2.25}$$

which is momentum independent [14].

2.4 Cosmic Ray Muons Underground

Due to their high energies and relativistic speeds, the cosmic muons reach the Earth's surface with sufficient energies to be detected and measured underground. As they propagate through the Earth, the muons suffer energy losses due to ionisation, bremsstrahlung, nuclear interactions, and direct electron-positron pair production. The knowledge of these processes allows an accurate description of the propagation of cosmic ray muons in standard rock. The energy-loss processes are described by,

$$-\frac{\mathrm{d}E}{\mathrm{d}x} = a + b\,E_\mu. \tag{2.26}$$

The parameter a describes the energy loss due to ionisation, while b is a sum of the following contributions,

$$b(E_\mu) = b(E_\mu)_{\mathrm{bremsstrahlung}} + b(E_\mu)_{\mathrm{nucl.\ interactions}} + b(E_\mu)_{\mathrm{pair\ production}}. \tag{2.27}$$

The values of both parameters a and b depend on the energy E_μ of the muon and also the material through which the muons propagate. An evaluation of the energy losses requires a treatment of the propagation of muons in matter and the respective differential cross-section of the muon-matter interactions. Detailed descriptions of these processes are provided elsewhere, for example in [34, 35, 36, 37]. The total energy loss for muons in various elements and compounds is computed in [37]. Values of the parameters a and b at selected muon energies are presented in Table 2.2. These values are used to calculate the total energy loss of the muons in standard rock using Equation 2.26 as shown in Figure 2.7.

Table 2.2: Parameters for muon energy loss in standard rock [38].

E_μ (GeV)	R km.w.e.	a (MeV $\mathrm{g}^{-1}\mathrm{cm}^{-2}$)	$b_{\text{brems.}}$ ——	b_{pair} (10^{-6} g^{-1} cm^{-2})	 ——	$b_{\text{nucl.}}$	$\sum b_i$
10	0.05	2.17	0.70	0.70		0.50	1.90
100	0.41	2.44	1.10	1.53		0.41	3.04
1000	2.45	2.68	1.44	2.07		0.41	3.92
10000	6.09	2.93	1.62	2.27		0.46	4.35

A parameterisation for a and b allows an accurate determination of the total muon energy losses,for example [39],

$$a(E_\mu) = 0.201\log_{10}(\mathrm{E}_\mu) + 1.97 \quad (\mathrm{MeV\,g^{-1}\,cm^2}) \tag{2.28}$$

$$b(\mathrm{E}_\mu) = (-0.205(\log_{10}(\mathrm{E}_\mu))^2 + 1.861\log_{10}(\mathrm{E}_\mu) + 0.245) \times 10^{-6}(\mathrm{g^{-1}\,cm^2}) \tag{2.29}$$

as illustrated on Figure 2.7. The total energy loss of muons in standard rock calculated from the parameterisations in Equations 2.28 and 2.29 are in very good agreement with the computed values [37]. In addition, a comparison is made for the energy loss calculation using approximated values $a = 2.2\mathrm{MeV/gcm^2}$ and $b = 0.004\mathrm{cm^2/g}$.

Assuming constant values of a and b, then Equation 2.26 can be integrated to estimate the range R,

$$R = \int_E^0 \frac{\mathrm{d}E}{-\mathrm{d}E/\mathrm{d}x} = \frac{1}{b}\ln(1 + \frac{b}{a}E_\mu), \tag{2.30}$$

for the cosmic ray muons in standard rock as illustrated on Figure 2.8. It follows that high energy muons can be measured at depths underground where the other EAS components do not reach. The intensity of the muons, however decreases quite significantly with increasing depth.

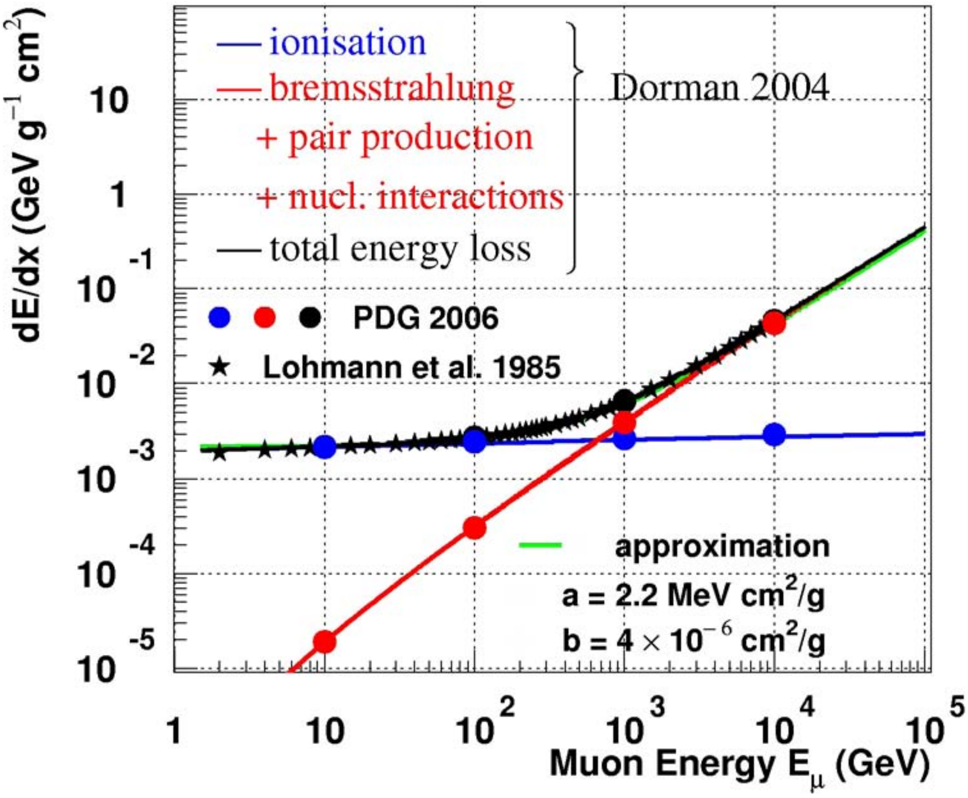

Figure 2.7: The energy loss and range of cosmic ray muons in standard rock. The computations by Lohman et al. 1985 and data by the particle data group PDG 2006 are contained in [37, 38], while the parameterisations by Dorman 2004 are described in [39].

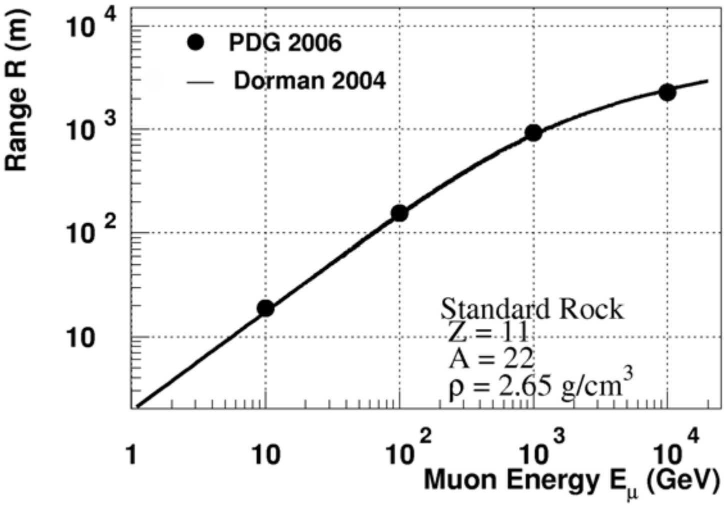

Figure 2.8: The range of cosmic ray muons in standard rock.

In this work, the cosmic ray muon energy $\mathrm{E}_{\aleph}$ measured in ALEPH at the depth $R = 325$mwe, is extrapolated to the obtain the corresponding energy at the surface E_{μ} using the relation,

$$E_{\mu} = \frac{a}{b}\left(e^{bR/\cos\theta} - 1\right) + E_{\aleph} \cdot e^{bR/\cos\theta} \,, \tag{2.31}$$

which takes into account the energy losses due to ionisation, bremsstrahlung, nuclear interactions and direct electron pair production described by the terms a and b respectively. In this extrapolation, the approximated values for a and b are used. Systematic uncertainties related to this approximation are investigated in Section 6.2.

2.5 EAS Simulation

The devlopment of extensive air showers (EAS) in the Earth's atmosphere is described by the physical processes of the respective particle interactions. There are several measurements and also analytical computations made to understand these processes. CORSIKA[1] [40] is the most widely used program for the simulation of EAS.

---

[1] **CO**smic **R**ay **SI**mulation for **KA**scade

The CORSIKA program includes various theoretical models to describe the interactions of cosmic ray particles in the Earth's atmosphere. The low energy models are mainly based on parameterisations of data, i.e. the interaction cross-sections obtained at accelerator energies. They include:

- GHEISHA (Gamma Hadron Electron Interaction SHower code) [41]
- FLUKA [42]
- UrQMD (Ultra-relativistic Quantum Molecular Dynamics) [43]

The high energy models are inspired by QCD[1] physics, i.e. based on parton - parton interactions within the hadrons. In this work, the following high-enrgy models have been used for the EAS simulations,

- DPMJET 2.55 (Dual Parton Model with JETs) [44]
- NEXUS 3.97 (NEXt generation of Unified Scattering approach) [45]
- QGSJET 01, II (Quark Gluon String model JETs) [46, 47]
- SIBYLL 2.1 [48]
- VENUS 4.12 (Very Energetic NUclear Scattering) [49]
- EPOS [50]

A detailed account of the models is provided elsewhere [3] and is rather beyond the scope of this work. However, it is important to note that the models differ in the way they predict, for example, the muon multiplicities in EAS. This is due to the different predictions of the interaction cross sections for the primary particles in the air. An example is illustrated in Figure 2.9 for the interaction of protons with air.

---

[1] **Q**uantum **C**hromo**D**ynamics

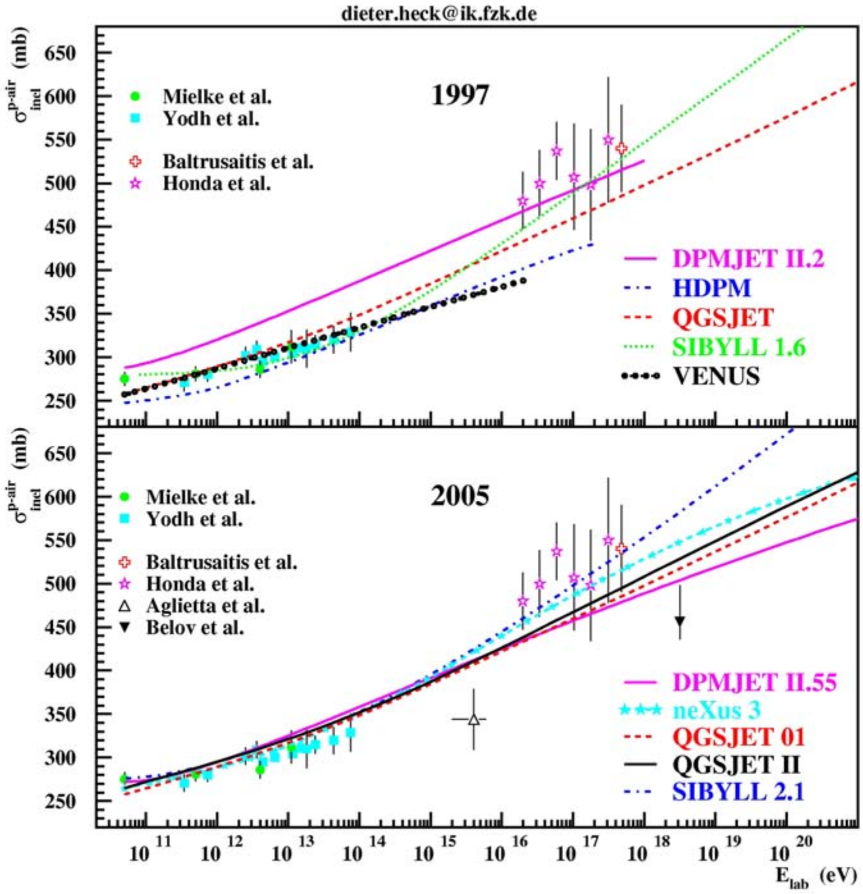

Figure 2.9: Comparison of p-air inelastic cross sections [77].

The model predictions are essentialy an extrapolation of the measurements. The currently used model predictions for the inelastic cross-sections are fairly close at low energies, for example in the energy range below 10^{14} eV relevant to the range of primary particle energies assumed in the Monte Carlo simulations in this work. Larger discrepancies are observed at higher energies. These discrepancies are reflected in the production of secondary particles, for example kaons and pions as shown in Figure 2.10. This affects the ability of the models to accurately describe data from cosmic ray experiments. The fine-tuning of the models, especially at high energies, is heavily impaired by the low statistics of data from Monte Carlo simulations. In some cases the data exceed the simulations by about a factor of 10 [3].

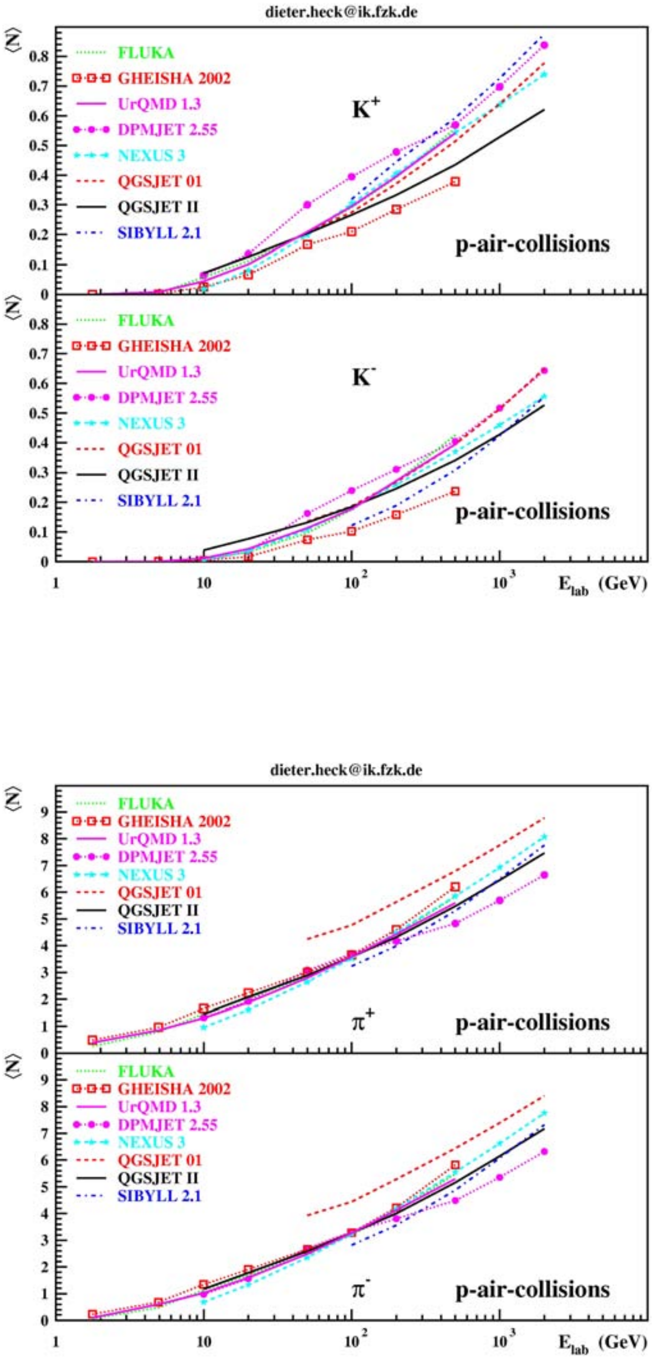

Figure 2.10: Production of kaons and pions from p-air collisions [77].

Chapter 3

The CosmoALEPH Experiment

The CosmoALEPH Experiment used the ALEPH apparatus in the LEP ring at CERN for measurements of cosmic ray muon events. A description of the experimental setup is provided in this chapter.

3.1 The ALEPH Apparatus at LEP

The location of the ALEPH apparatus and it's reference system in the LEP ring is sketched in Figure 3.1.

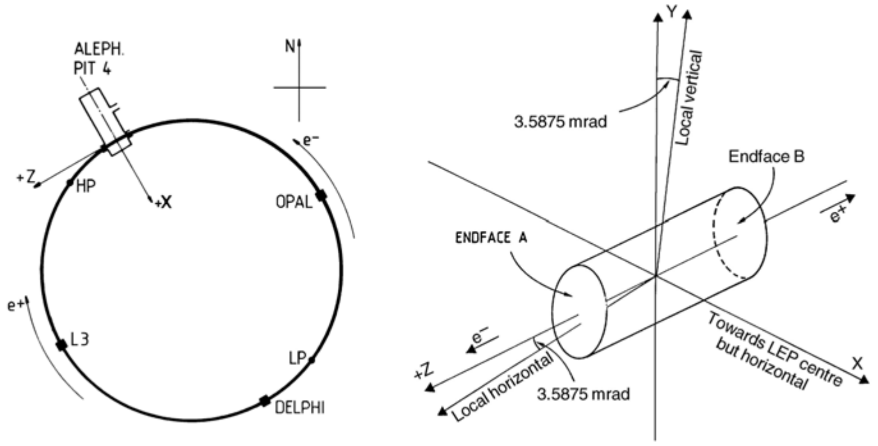

Figure 3.1: The location and reference system of ALEPH at LEP [51]. The direction of the north is indicated by N.

The LEP ring was inclined by $\approx 1.42\%$ and had an average diameter of 8486 m, corresponding to ≈ 27 km circumference. The floor of the counting hall in Pit 4, where ALEPH was located, was at a depth of 143 m underground. The pit was 70 m long in the radial direction of LEP, 21.4 m wide along the beam line and about 16 m high. The theoretical point where the beam crossing point is adopted to be the centre of the reference system. The positive z-axis is along the e^- beam direction while the positive x-axis points towards the LEP centre.

A general view and a sectional view of the ALEPH aparatus is presented in Figures 3.2 and 3.3 respectively showing the various sub-detectors. The entire system of sub-detectors and their respective components is refered to as the ALEPH Apparatus.

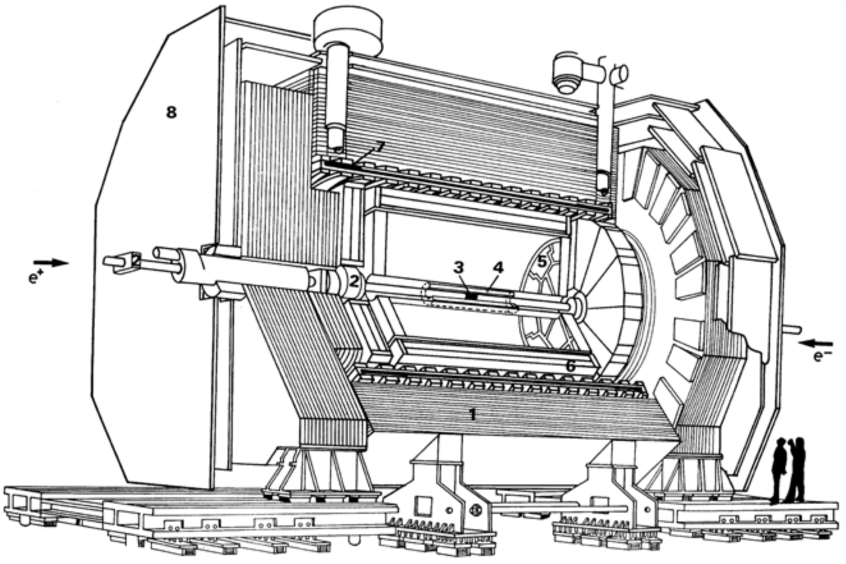

Figure 3.2: The ALEPH Apparatus [51]. Hadron Calorimeter (1), Luminosity Monitors (2), Vertex Detector (3), Inner Track Chamber (4), Time Projection Chamber (5), Electromagnetic Calorimeter (6), Superconducting Magnet Coil (7), Muon Chambers (8).

The ALEPH apparatus was built for the physics of e^+e^- collisions. The collisions took place at the center of the apparatus. This is known as the *interaction point.* A cylindrical design of the whole apparatus along the beam pipe provided an optimal geometry to record as much information over the solid angle as possible. A superconducting coil created a magnetic field of 1.5 Tesla, bending the trajectory of the charged particles and thus allowing the measurement of the particles' momenta in the TPC.

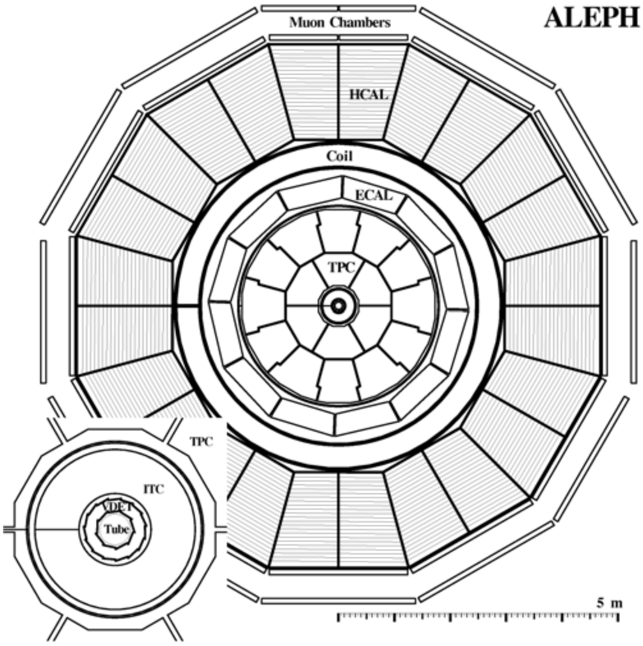

Figure 3.3: A sectional view of the ALEPH apparatus [51]. The inset shows the Inner track Chamber (ITC), the Vertex DETector (VDET) and the beam pipe.

The normal e^+e^- data taking required that all the detector components be operational. The muon chambers enabled a pre-selection of cosmic ray muon events recorded during the normal data taking periods. These data are used in this work to determine the trigger efficiency for the HCAL. During the dedicated CosmoALEPH runs, only the HCAL and the TPC were used to measure cosmic ray muons. Early *cosmic runs*, dating back to 1991 proved useful to the alignment of some parts of the detector, for example the TPC and the ITC [53].

3.1.1 The Hadron Calorimeter

The hadron calorimeter consisted of a central barrel and two end-caps as shown in Figure 3.4. The barrel consisted of 12 modules, each with 22 slabs, each of 5cm thickness and an extra slab of 10 cm thickness. The slabs were made of iron. The total thickness of the calorimeter was 120 cm corresponding to about 7.16 interaction lengths at 90^0 with respect to the beam line [51]. This value is, however, modulated in azimuthal angle by the *dodecagonal* structure of the modules, from 120 cm at the centre of the module to 124cm at the edges. The additional iron rods used to provide mechanical stability of the whole structure contributed to an insensitive area of about 3.4% of the full azimuthal angle.

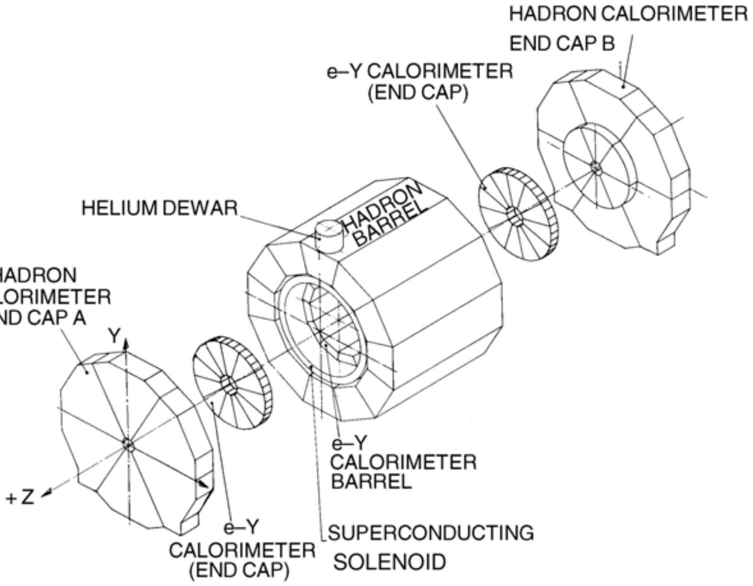

Figure 3.4: The Hadron Calorimeter (HCAL) [51].

The end-caps consisted of six petals, each with 22 slabs of 5cm thickness and an extra slab of 10cm thickness. All slabs were separated by 2.2cm gaps for the detector layers.

3.1.2 The Time Projection Chamber

In the ALEPH apparatus, the TPC served as the central detector for the measurement of charged particles. It was 4.4 m long, 3.6 m in diameter and filled with argon (91%) + methane (9%) at an operational pressure of 7-8 mbar above the barometric pressure in the experimental zone. The TPC had two main components; the field cages (inner and outer cylinders) and the two end-plates. Between the two end-plates was a high-voltage central membrane as shown in Figure 3.5. The membrane, made from 25 μm mylar, was coated on both sides with graphite paint and maintained at a negative high-voltage so that a drift field of about 115 V/cm is maintained in parallel to the axis of the TPC. This corresponds to a drift velocity of about 5.22 $cm/\mu sec$ and a drift length of 220 cm.

The motion of charged particles ionises the gas mixiture in the TPC producing electron-ion pairs. The electrons drift towards the wire chambers at the end-plates of the TPC. Due to the electric (**E**) and magnetic (**B**) fields in the TPC, the electrons experience the Lorentz force (**F**) which can be expressed as follows,

$$\mathbf{F} \;=\; e\,(\mathbf{E} \,+\, \mathbf{v} \,\times\, \mathbf{B}) \tag{3.1}$$

where e and $\mathbf{v}$ are the electric charge and velocity of the electrons respectively. The drift velocity $\mathbf{v_d}$ which can the be expressed as follows,

$$\mathbf{v_d} \;=\; \frac{\mu}{1+(\omega\tau)^2}\left(\mathbf{E} \,+\, (\omega\tau)\,\frac{\mathbf{E}\times\mathbf{B}}{|\mathbf{B}|} + (\omega\tau)^2\,\frac{(\mathbf{E}\cdot\mathbf{B})\,\mathbf{B}}{|\mathbf{B}|^2}\right) \tag{3.2}$$

where τ is the mean drift time between the collisions, and

$$\mu \;=\; \frac{e\,\tau}{m}$$

$$\omega \;=\; \frac{e\,\mathbf{B}}{m\,c}$$

are the the particle mobility and cyclotron frequency respectively.

The uniformity of the electric and magnetic fields therefore play an important role in determining the drift velocity of the electrons and hence the

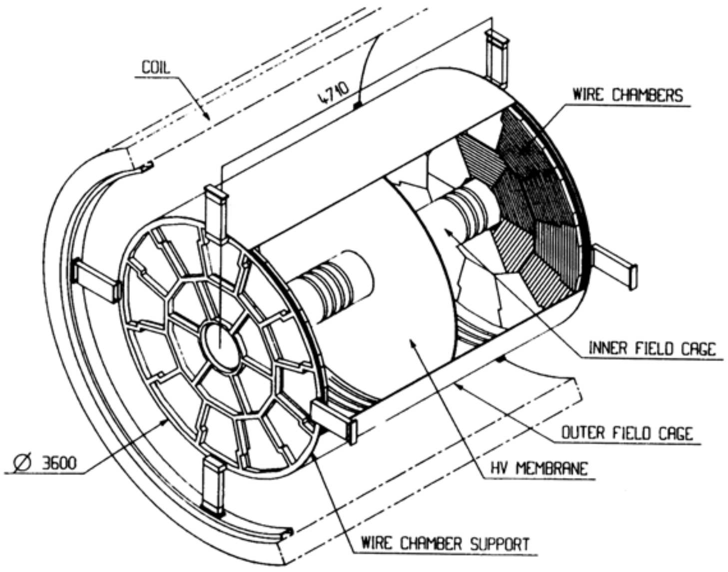

Figure 3.5: The Time Projection Chamber (TPC) [51].

projections of the tracks onto the wire chambers at the end-plates of the TPC. The tolerance of the electric field in the ALEPH TPC is ± 6V, while the tolerance of the magnetic field is defined by [51],

$$\int_0^{220} \frac{B_r}{B_z}\, dz \;<\; 2\text{mm} \tag{3.3}$$

where B_r and B_z (= 1.5 Tesla) are the radial and main field components respectively. This integral determines the distortions of the sagitta, which is an important parameter for particle tracking in the TPC.

The main advantage of the TPC is its homogeneity in r and ϕ providing a high track resolution of $\approx 160\ \mu m$. The particles are identified from their respective energy losses by ionisation, $\mathrm{d}E/\mathrm{d}x$ whose parametrisation is of the form,

$$\frac{\mathrm{d}E}{\mathrm{d}x} \approx \frac{1}{1 + \mathrm{C}\ln(\Delta\mathrm{x}/\Delta\mathrm{r})}\,, \tag{3.4}$$

where $\Delta r = 0.4$ cm is the distance between the wires in the TPC and Δx is the corresponding track length [51].

Chapter 4

Simulations and Measurements

In this Chapter a brief account of the Monte Carlo simulations and measurements of the muon component of extensive air showers (EAS) in the CosmoALEPH experiment is presented.

4.1 Air Shower Simulations

The simulation of EAS in this work aims at studying the response of the ALEPH apparatus to measurement of cosmic ray muons. The scheme of the simulations and measurements is illustrated in Figure 4.1. The CORSIKA program [40] is used to simulate the muon component of extensive air showers (EAS) in the CosmoALEPH experiment. This is a detailed Monte Carlo program for the four dimensional simulation of EAS and takes into account the various particle interactions, their decays and also their deflection in the Earth's magnetic field. The program incorporates different hadronic interaction models as described in [40]. A wide range of primary particles can be used for the simulations. They include photons, protons and heavier nuclei (He, Fe, etc.). In this work only protons were chosen as the primary particles in the energy range 100 GeV to 10 PeV (see Appendix 1). The slope of the primary protons simulated is $\gamma = 2.7$ as explained by Equation 2.9. The primary protons interact in the Earth's atmopshere leading to the production of cascades of secondary particles (see Section 2.1).

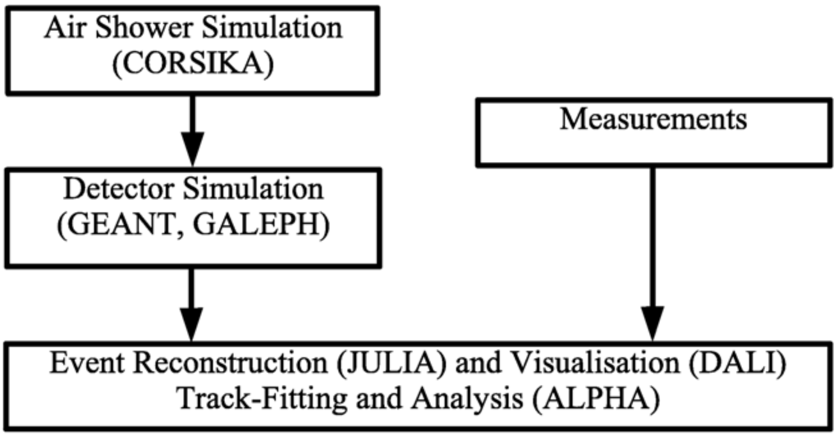

Figure 4.1: Simulation and measurements cosmic ray muons in this work.

The hadronic and electromagnetic components of the EAS are not included in the simulations. The muon component, also known as the *hard component* of the EAS is sufficiently energetic to reach the Earth surface. The momentum and zenith angle distributions of the muons predicted by the hadronic interaction models as shown in Figures 4.2 and 4.3. The low energy interaction model, GHEISHA [41] is used for the simulations. The models exhibit some slight differences in the way they generate the zenith angle distributions for cosmic ray muons at the Earth's surface. The shapes of the momentum distributions are nevertheless similar. Therefore, this allows one to select the cosmic ray muon component from one of the components to study cosmic ray muon measurements underground. The muon component simulated using the VENUS model is used in this work to study the response of the ALEPH apparatus to cosmic ray muon measurements. At the Earth's surface, the muons are uniformly distributed in azimuth angle as illustrated in Figure 4.4.

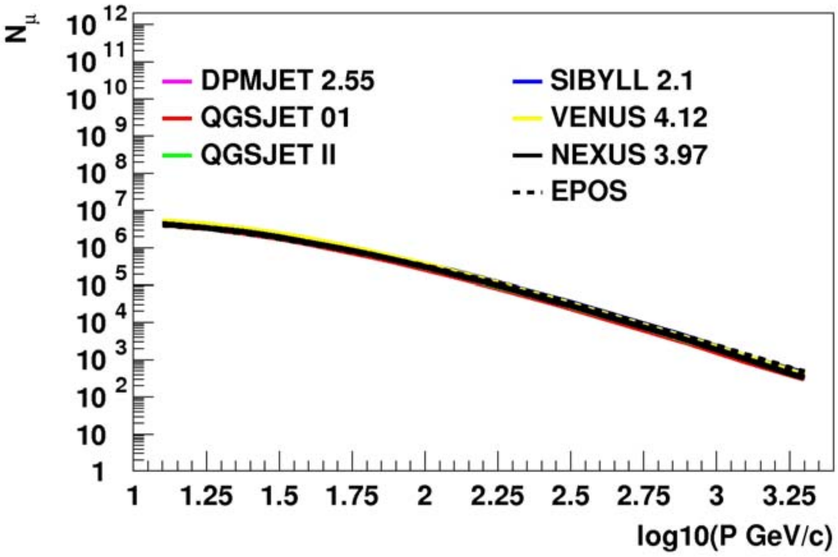

Figure 4.2: Simulated momentum distributions of cosmic ray muons at zenith angles $\theta \leq 89^0$.

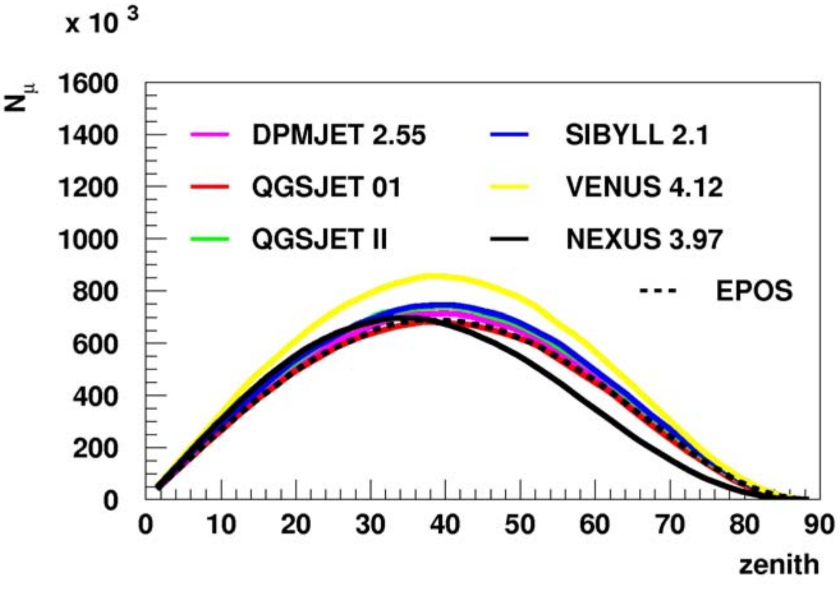

Figure 4.3: Simulated zenith angle distributions of cosmic ray muons.

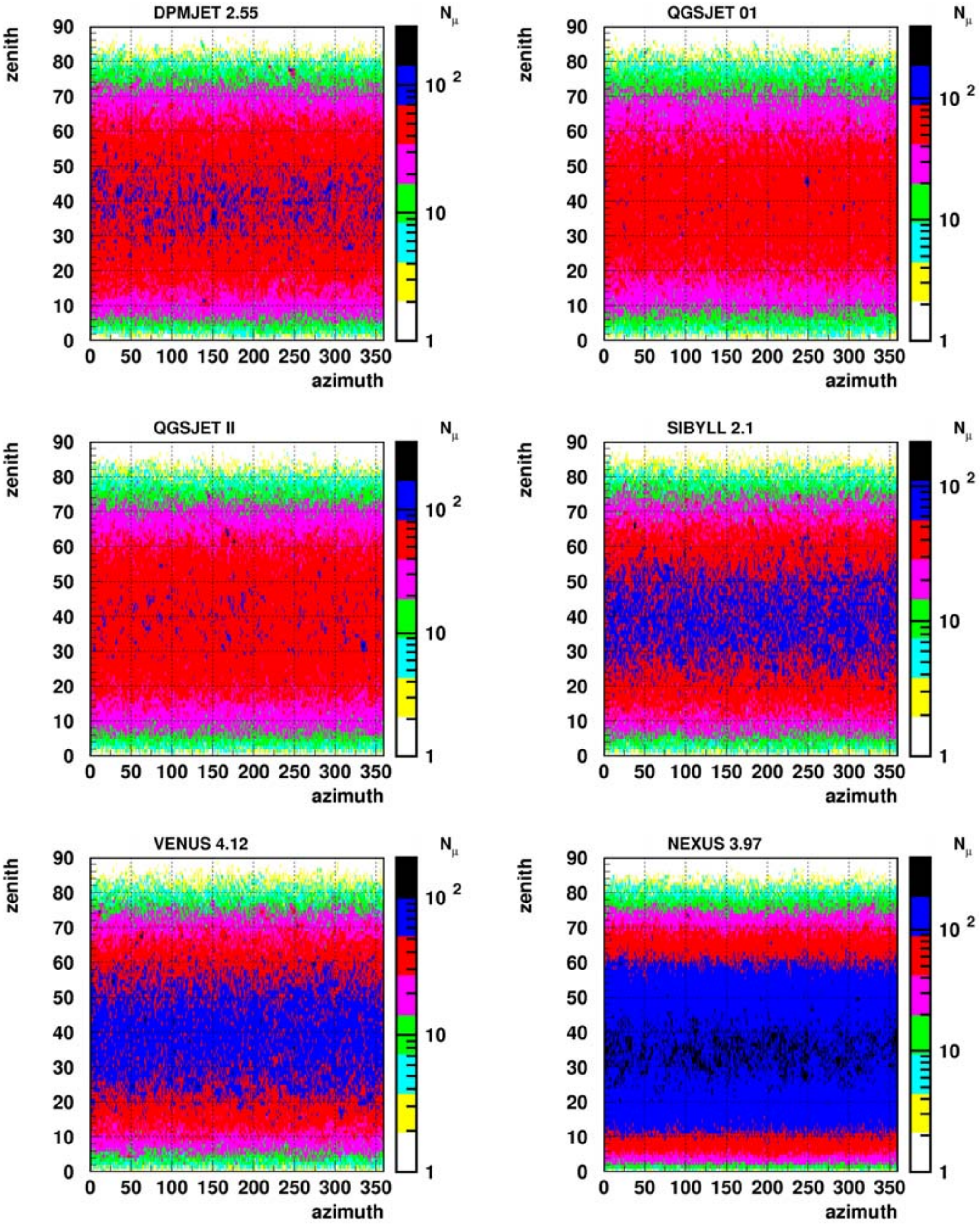

Figure 4.4: Zenith-azimuth angle distributions for cosmic ray muons simulated using different hadronic interaction models

4.2 Detector Simulations

The simulated muon component at the Earth's surface is then propagated through the overburden to the ALEPH level, at 143 m underground (Figures 8.1 and 8.2) using the GEANT simulation program [56]. The GEANT program simulates the physical processes like energy losses and interactions of the cosmic ray muons in the overburden. The muons are then tracked in the ALEPH apparatus using the GALEPH[1] program [57]. This is a detailed Monte Carlo simulation of particle interactions and physics processes in the detector components of ALEPH. All the technical details like digitisation of the hits in the TPC are included in this simulation. Figures 4.5 and 4.6 show a comparison between measured data and simulations of the zenith and azimuth angle distributions of cosmic ray muons in ALEPH. Due to the longerr path lengths at zenith angles $\theta \geq 20^0$, the inclined muons suffer significant energy losses in the overburden.

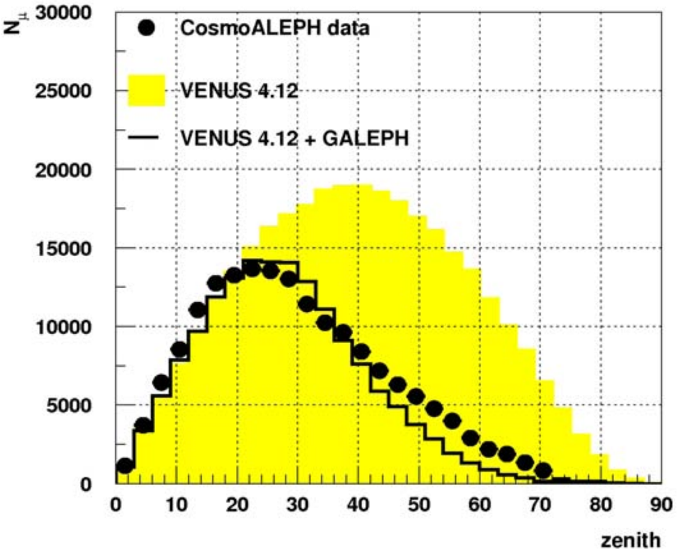

Figure 4.5: Zenith angle distribution. The Monte Carlo simulations are normalised to the data.

---

[1] **G**EANT for **ALEPH**

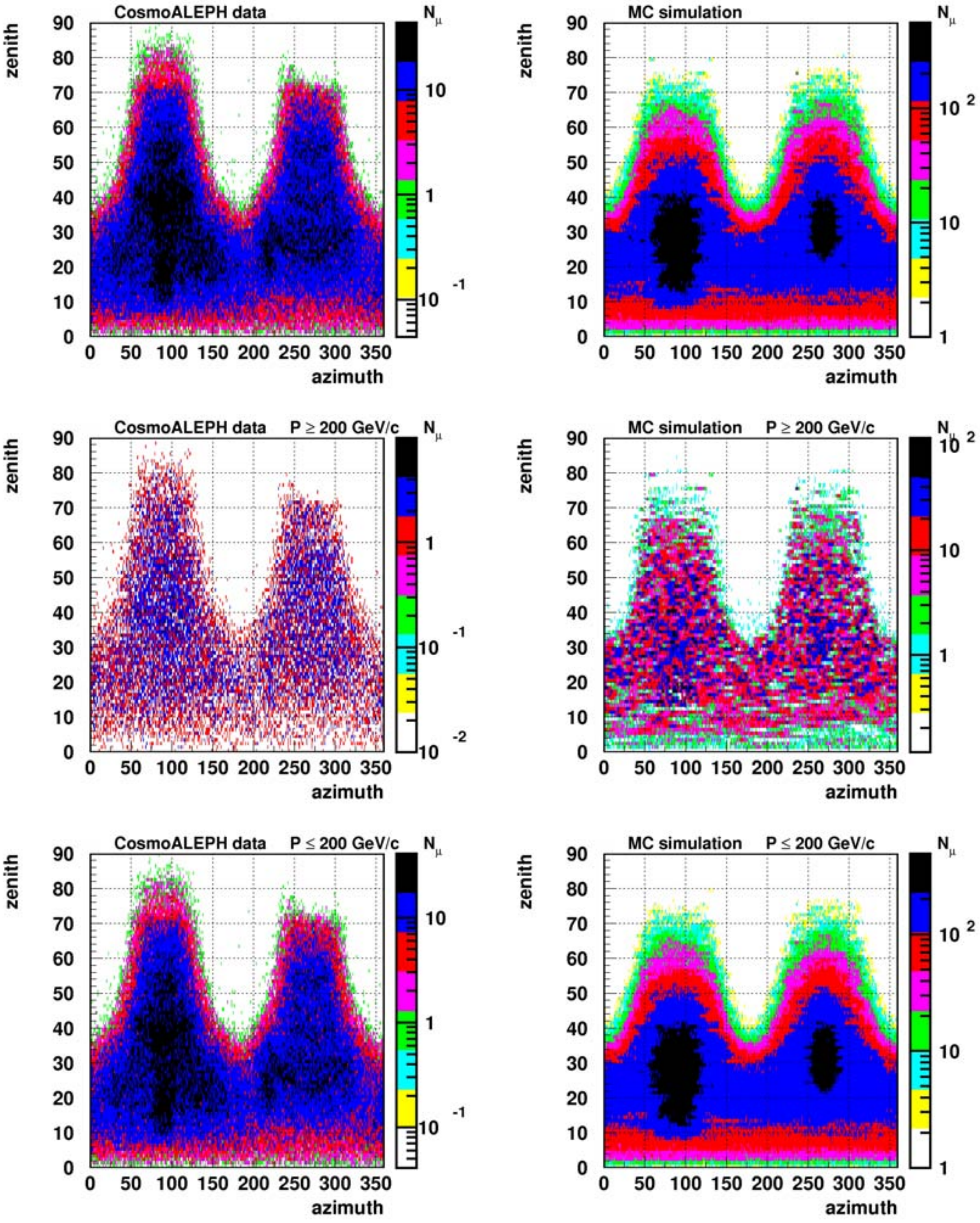

Figure 4.6: Zenith-azimuth angle distribution. The data are compared with Monte Carlo simulations. Note the effects of the access shafts in the P4 experimental zone allowing more low energy muons.

The trigger conditions in the CosmoALEPH data result in some asymetry in the distribution of the cosmic ray muons with respect to the azimuth angle. These factors lower muon fluxes particularly evident for zenith angles larger than 20 degrees. It is also interesting to note that the constructions surrounding the ALEPH apparatus also contribute to the asymetrical distributions of the measured muons. For example, the access shafts to the P4 experimental zone are large enough to allw low energy muons to reach the ALEPH level. This causes a localised increase in flux for muons with momenta $P \leq 200$ GeV/c. This effect is also observed in the Monte Carlo Simulations. Figure 4.7 shows a sample of the simulated cosmic ray muons through the overburden.

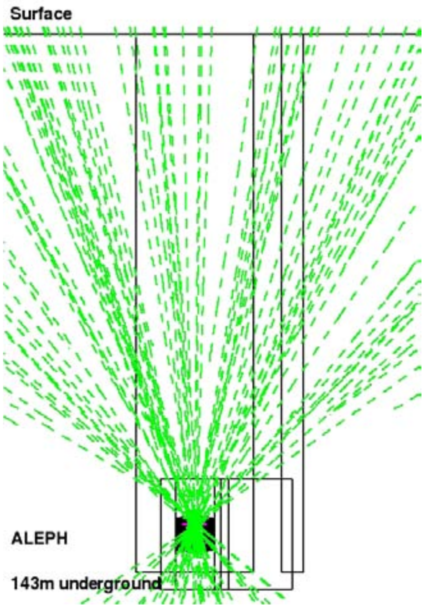

Figure 4.7: Simulated cosmic ray muon events through the overburden.

The Jura mountains *shield* the ALEPH apparatus to cosmic ray muons inclined beyond 70 degrees in zenith. This effect is observed in the data for muons in the azimuth range between 250 and 300 degrees. Figures 4.5 and 4.6 show that the of cosmic ray muons measured at zenith angles $\theta \leq 20^0$ are uniform, hence the analsis requires no consideration of the angular acceptance of the ALEPH apparatus.

4.3 Performance of the ALEPH TPC

The performance of the ALEPH TPC for the physics of e^+e^- collisions has been reported elsewhere [58]. In this work a uniformly-distributed sample of muons with momentum values in the range of 5 GeV/c to 3 TeV/c were generated on top of ALEPH such that the entire mid-plane of the TPC ($y = 0$) is uniformly illuminated. The sample was isotropic arround the vertical up to zenith angles of 30^0. Simulations of the muon interactions and measurements were implemented using the GALEPH program. The aim of these simulations is to determine the performance of the TPC for the measurements of cosmic ray muons.

4.3.1 Effective Area

Cosmic ray muons generally hit the entire region of the TPC. It is however important to determine the effective area for the high quality measurements. For this study, the uniform sample of muons are generated in the entire geometrical area of the TPC $\approx 16m^2$ and reconstructed. The coordinates of the tracks at the midplane of the TPC ($y = 0$) are shown on Figure 4.8

Along the central membrane of the TPC ($z = 0$), there is a reduced concentration of the measured tracks. This effect is not observed in the simulated tracks. An investigation of the tracks through the membrane reveal some sort of misaligned track reconstruction for the mesured data. A sample track is shown in Figure 4.9. A comparison is made with the Monte Carlo data. Slight differences between the drift velocity used in the reconstruction and the true physical value is a possible reason for the misalignment of tracks.

From the Monte Carlo simulations, it is shown that the muon events generated at the edges of the TPC can not be measured. In order to understand this pattern, the number of hits for tracks in the TPC as a function of the distance x from the beam line is illustrated on Figure 4.10.

The cylindrical design of the TPC and the requirement of more than 5 hits in the TPC per track limits the measurement area of the muons. Therefore, measurements are only confined to within a 150 cm radius of the TPC. This corresponds to about 83% of the geometrical area $\sim$ 16m^2.

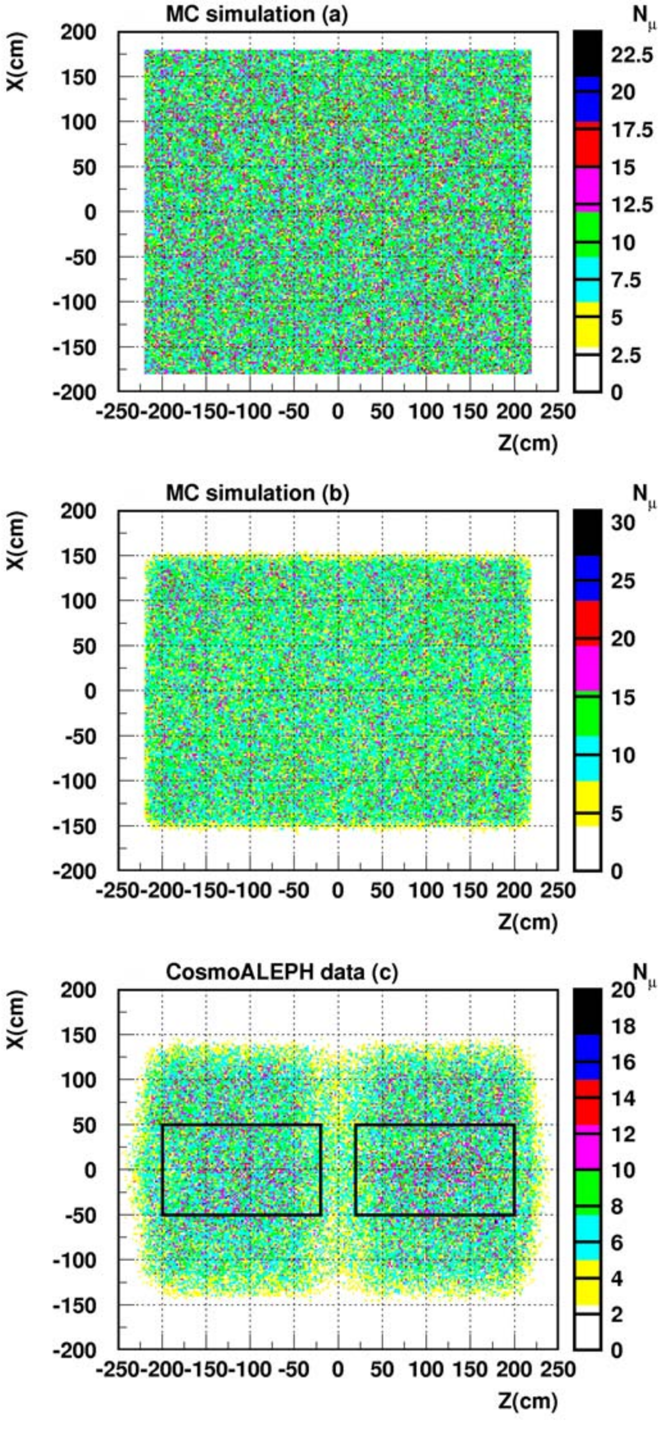

Figure 4.8: The effective area of the TPC for measurement of cosmic ray muons ($\theta \leq 20^0$). The Figure illustrates coordinates of the tracks at the midplane of the TPC ($y = 0$). For the Monte Carlo simulations (a) and (b) represent the generated and reconstructed tracks respectively.

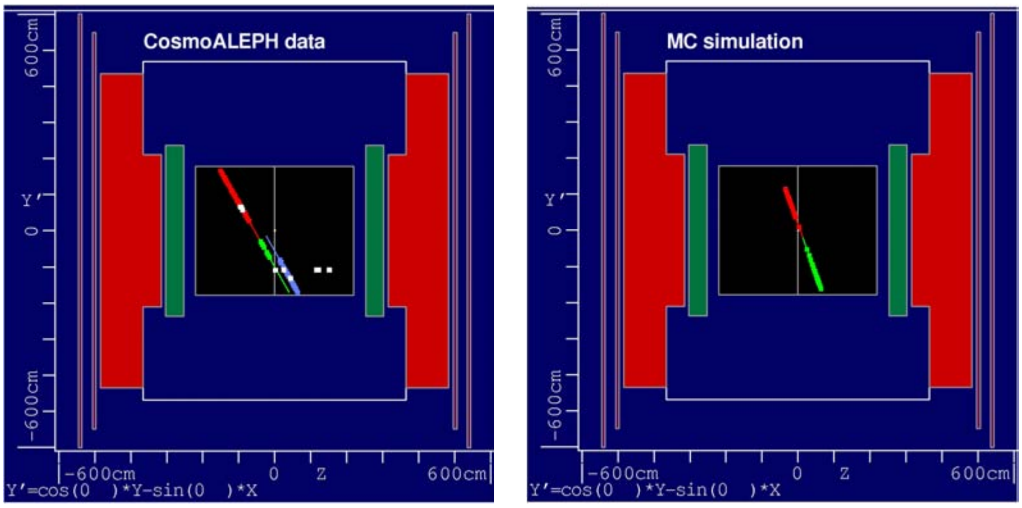

Figure 4.9: The track of a measured and simulated cosmic ray muon through the membrane of the TPC. Note the misaligned segments of the measured track.

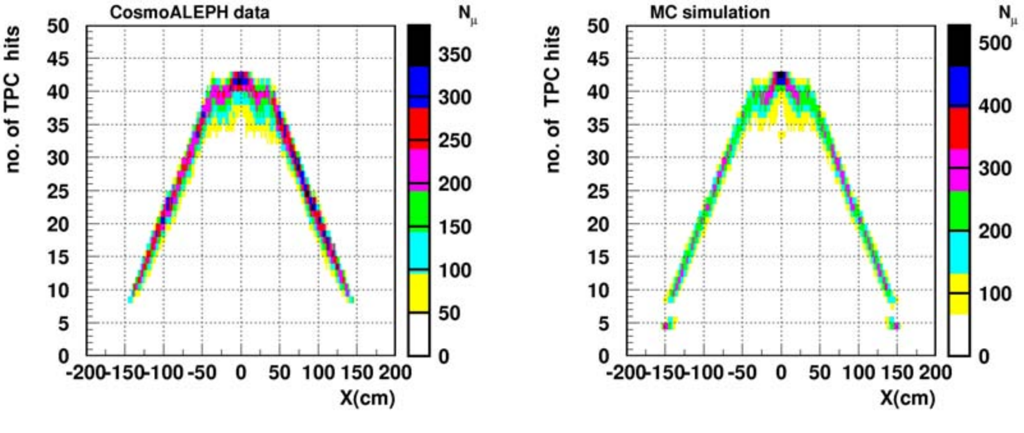

Figure 4.10: Distribution of track hits in the TPC. The data are compared with Monte Carlo simulations. Note the requirement of at least 6 hits on tracks in the TPC restricts measurements to within ±150 cm on the X-axis.

The Monte Carlo simulations do not reproduce the effect of the central membrane observed in the data. Therefore the analysis is restricted to the range between 20cm $\leq |z| \leq$ 200cm. In addtion, in order to have uniformly bes momentum resolution, tracks with coordinates $|x| \leq$ 50cm at the midplane $y = 0$ of the TPC are considered for analysis. This therefore defines the fiducial area of the TPC for high quality measurements. The area on the mid-plane of the TPC defined by $|x| \leq$ 50cm and 20cm $\leq |z| \leq$ 200cm is referred to as the *central part of the TPC* and illustrated by the boxes in Figure 4.8 (c).

4.3.2 Track Fitting

When considering cosmic ray muons in the ALEPH TPC, the energies are sufficiently high such that the force due to the magnetic field is much higher than that due to the electric field. This allows the first term of Equation 3.1 to be ignored so that the Lorentz force can be expressed as;

$$\mathbf{F} \simeq q_\mu \mathbf{V} \times \mathbf{B}, \tag{4.1}$$

where q_μ and $\mathbf{V}$ are the charge and velocity of the muon respectively. Just like other charged particles in a uniform magnetic field, the trajectory of the cosmic ray muons can therefore be described by a helix. The electron-ion pairs produced by the muons provide three-dimensional hit information on the path of the muons. The position of the hits in the TPC are then fitted to determine the particles' momentum. The track fitting for cosmic ray muons simulated in the TPC, follows the same procedure as for normal track-fitting in ALEPH [59]. The procedure is done typically in three steps;

- a circle fit in the x-y plane,
- a straight line fit in the $S_{x,y}$ plane, and
- simultaneous Newtonian iterations in all helix parameters.

Figure 4.11 illustrates track fitting in the ALEPH TPC. The χ^2-probability of the track fit, shown on Figure 4.12, is an indicator of the quality of the track fitting. A comparison is made between data and Monte Carlo simulations.

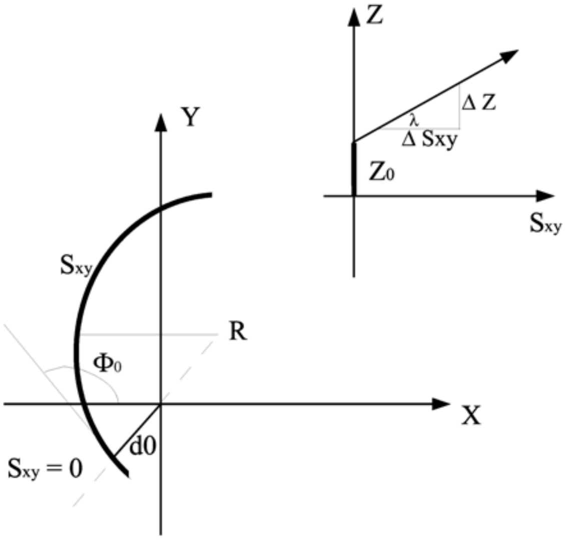

Figure 4.11: Track fitting in the ALEPH TPC[59]

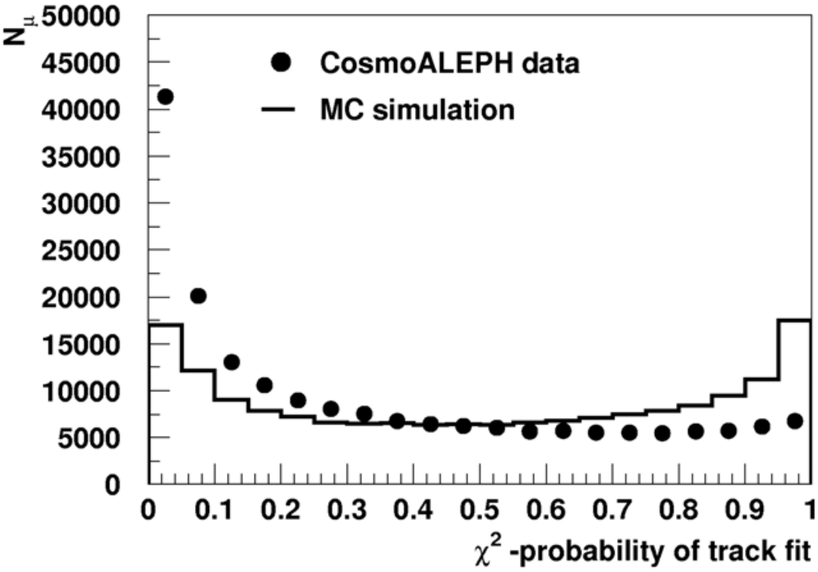

Figure 4.12: χ^2 -Probability of track fitting in the ALEPH TPC. Data and Monte Carlo both refer to tracks fitted in the entire area of the TPC.

In both cases, the χ^2-probability of track fitting is non-uniform. This indicates that a helix model, though acceptable for the fitting of tracks in the TPC, does not perfectly describe the trajectory of the muons in the TPC.

4.3.3 Momentum Measurement

From the track fitting procedure, the track radius R and the inclination λ of the straight-line fit in the $S_{x,y}$ plane are obtained. This allows to determine the transverse component of the muon momentum,

$$\mathbf{P_t} = R\, q\, \mathbf{B} = \frac{A}{\omega}\,, \tag{4.2}$$

where q = particle charge and **B** = magnetic field in the TPC. The total momentum is therefore,

$$P = P_t\,(1\, +\, t^2)^{1/2}\,, \tag{4.3}$$

with $t\ =\ \tan(\lambda)$. Figure 4.13 shows the reconstructed muon momenta in the TPC.

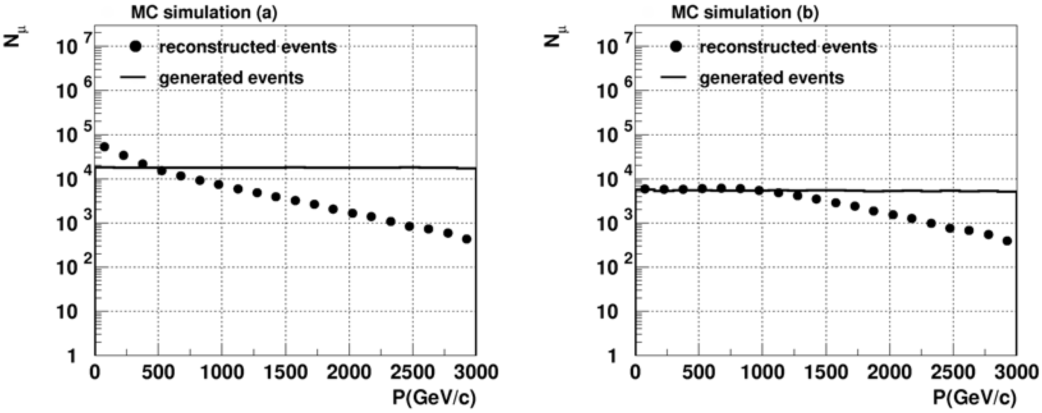

Figure 4.13: Reconstructed Momentum in the TPC. Figure (a) is for the entire TPC area. Figure (b) is for the central part of the TPC.

The Monte Carlo data show that the measurement of the momentum at the central part of the TPC are most accurate. Tracks at the edges of the TPC are associated with low number of hits in the TPC and hence leading to poor track fitting and reconstruction.

4.3.4 Measurement Uncertainties

A simple treatment of error propagations can be applied to determine the uncertainties associated with the momentum measurement. This is expressed as

$$\frac{dP}{P} = \sqrt{\frac{C_{\omega\,\omega}}{\omega^2} - \frac{2\,t\,C_{\omega\,t}}{\omega\,(1\,+\,t^2)} + \frac{t^2\,C_{t\,t}}{(1\,+\,t^2)^2}}\,, \tag{4.4}$$

with, $C_{\omega\,\omega}, C_{\omega\,t}, C_{t\,t}$, being the covariances obtained from the track fitting. The measurement uncertainties depend on the number of hits in the TPC as illustrated on Figure 4.14.

In all cases, the uncertainties are linearly related to the measured momenta. The profiles of the measurement uncertainties, shown in Figures 4.15 and 4.16 for the Monte Carlo simulations and measured data, show that the central part of the TPC provides measurements with better momentum resolution.

The *pull* parameter,

$$pull(P) = \frac{1/P_{true}\;-\;1/P_{rec}}{\sigma\,(1/P_{rec})}\,, \tag{4.5}$$

is often used for statistical analyses of the calculations. The obtained distribution, shown on Figure 4.17, is well described by a Gaussian function with a standard deviation $\sigma \;\approx\; 1$. This is an indication that the measurement uncertainties are statistical in nature and that they are correctly estimated by the fit.

In addition, d(1/P) has been evaluated both for Monte Carlo simulations and measured data. This is shown on Figure 4.18. A good agreement is observed between data and Monte Carlo Simulation. The measurement uncertainties are low for tracks in the central part of the TPC, i.e. $x \leq$ 50cm. As already illustrated on Figure 4.10, the tracks in the central part of the TPC

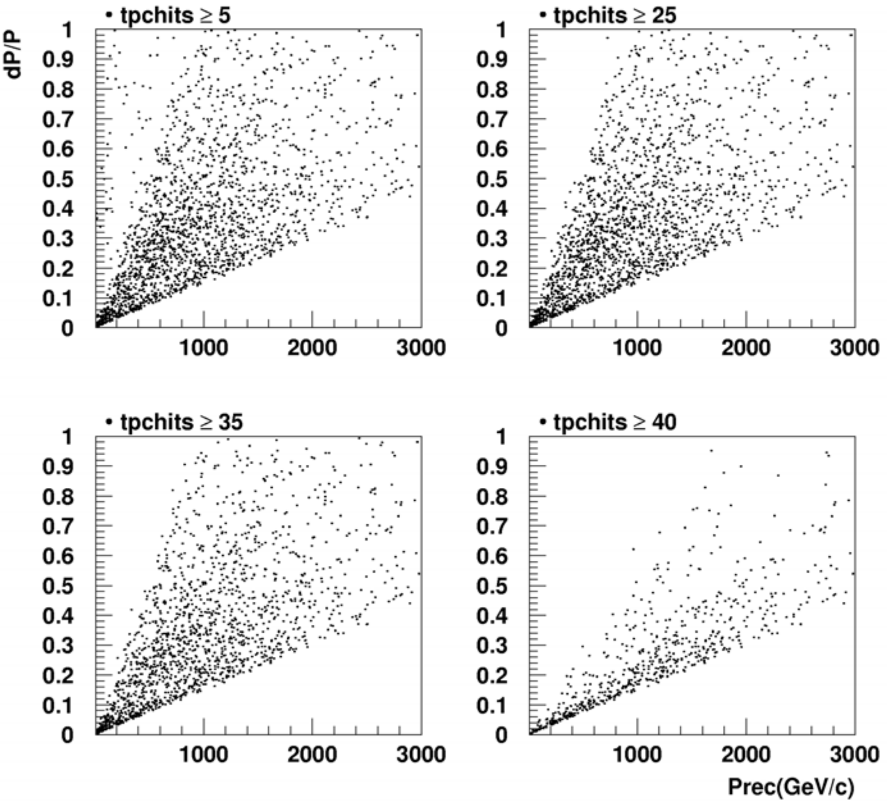

Figure 4.14: Measurement Uncertainties

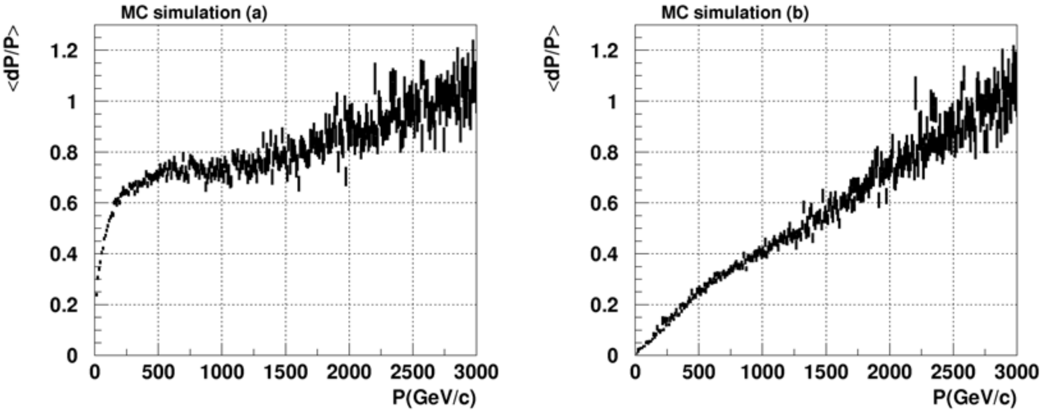

Figure 4.15: Measurement uncertainties from MC data. Figure (a) is for the entire TPC area. Figure (b) is for the central part of the TPC.

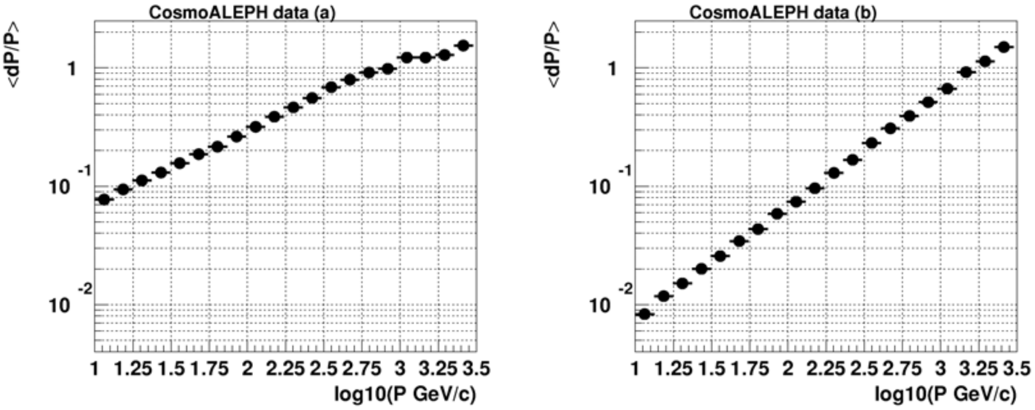

Figure 4.16: Measurement uncertainties from CosmoALEPH data (a) in the entire TPC area, (b) in the central part of the TPC.

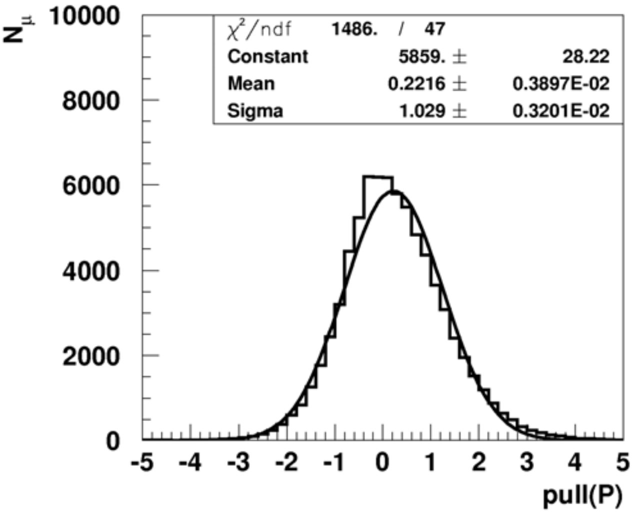

Figure 4.17: Pull distribution for tracks fitted in the entire area of the TPC.

have the highest number of hits and hence low measurement uncertainties. In both data and MC simulations, the χ^2-probability of track fitting and the measurement uncertainties are not correlated. This allows data analysis without neccessarily imposing further requirements based on the χ^2-probability track-fitting.

4.3.5 Track Reconstruction Efficiency

Figure 4.19 shows the tracks of single cosmic ray muon events in the ALEPH detector fitted by the ALEPH reconstruction program JULIA[1][59]. Both segments of the track in (a) are successfully reconstructed. However, in some cases as shown in (b), the JULIA program fails to fully reconstruct one or both segments of a track in the TPC. This program was mainly developed for the reconstruction of particle tracks from e^+e^- events. Those tracks originated from the interaction point in the centre of the detector.

An estimate of the track reconstruction efficiency as a function of the muon momentum extrapolated to the surface is shown in Figure 4.20. The *true events generated* refer to muons generated in the central part of the TPC. Events will be accepted in the analysis if the reconstructed momentum in the TPC is $P \geq 10$ GeV/c with the estimated uncertainty $dP/P \leq 1$ and zenith angle $\theta \leq 20^0$. The *true events reconstructed* refers to the true momenta of the events accepted in the analysis. The ratio of the *true events reconstructed* to the *true events generated* gives an estimate of the track reconstruction efficiency as a function of the true momentum. Momentum smearing is not considered at this point. The low track reconstruction efficiency at low momenta $P \leq 100$ GeV/c is due to the momentum cut-off by the overburden. The poor momentum resolution at higher momenta $P \geq 1$ TeV/c leads to a drop in the track reconstruction efficiency.

---

[1] **J**ob to **U**nderstand **L**ep **I**nteractions in **A**LEPH

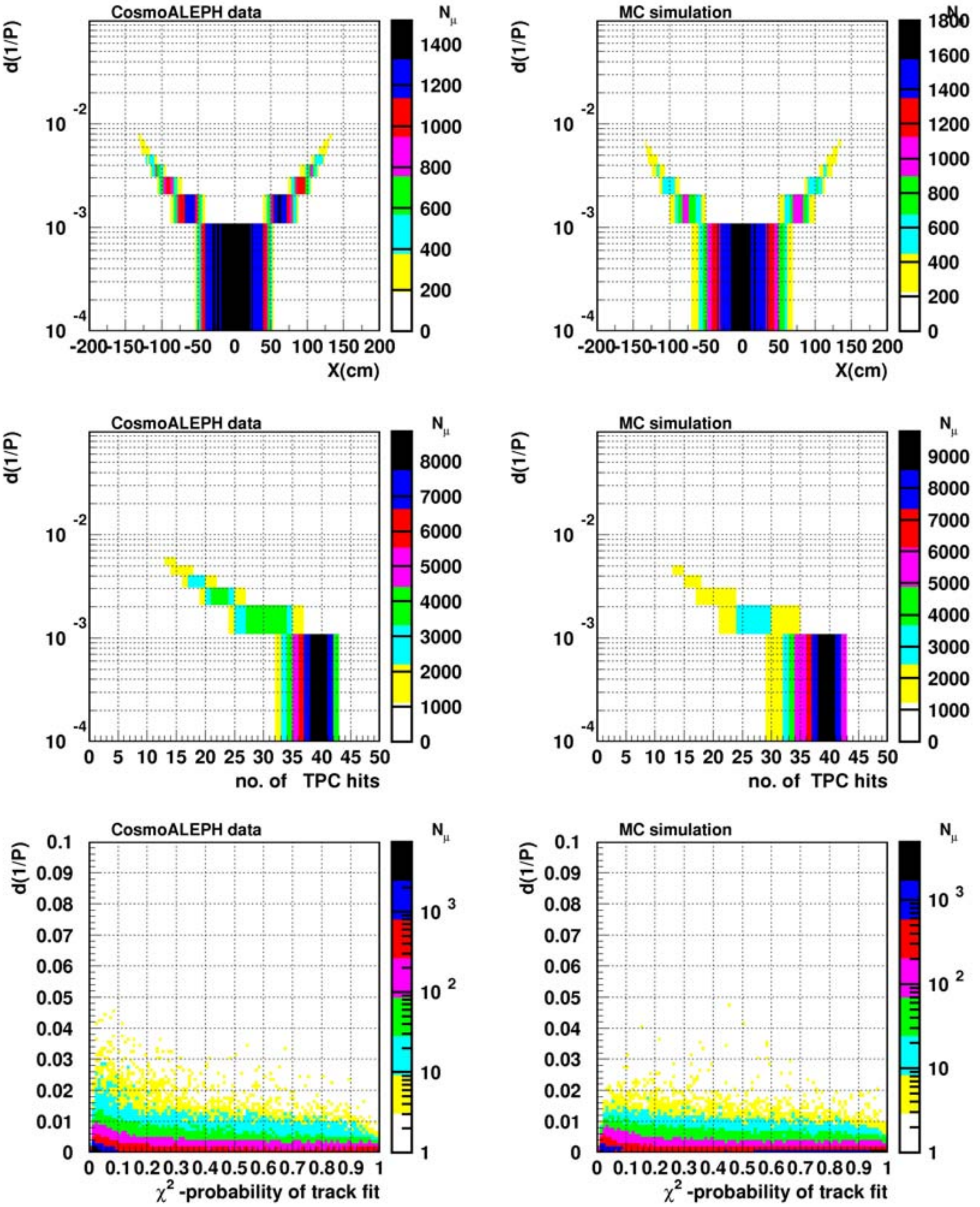

Figure 4.18: Measurement uncertainties in the TPC in relation to; the postion of the track along the x-axis, the number of hits for the track and the χ^2-probability of track fitting.

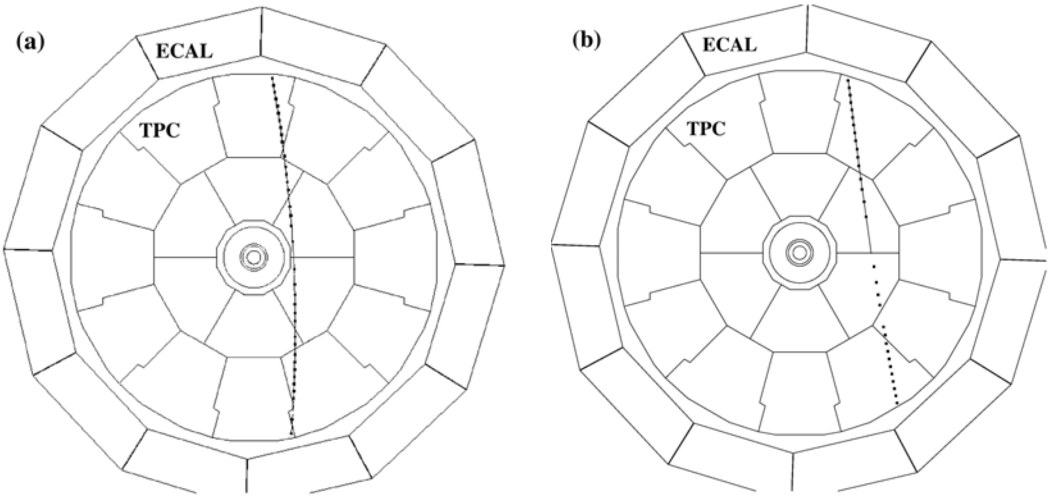

Figure 4.19: Reconstruction of single cosmic ray muon events in the TPC. The track in (a) is a fully reconstructed while that in (b) is partially reconstructed.

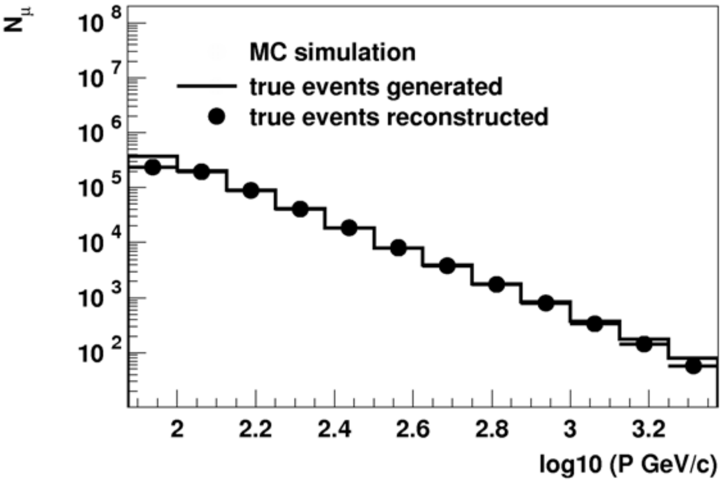

Figure 4.20: Track reconstruction in TPC.

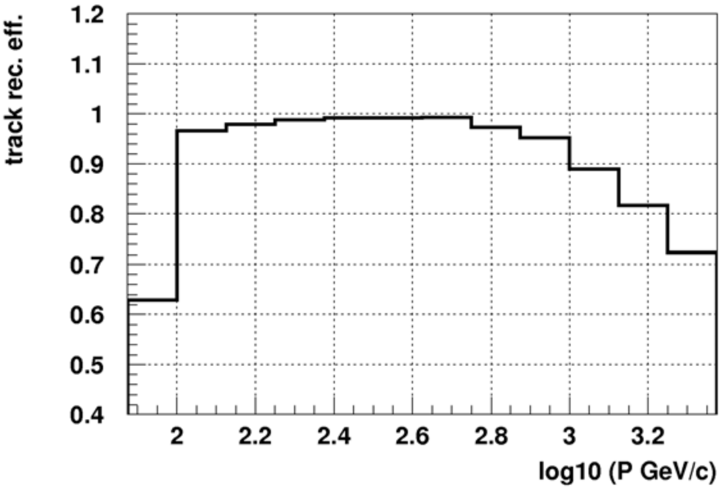

Figure 4.21: Track reconstruction efficiency in TPC.

4.4 Trigger Efficiency of the HCAL

During the dedicated CosmoALEPH runs for cosmic ray muon measurements, the trigger requirement was at least eight hits in two or more modules of the hadron calorimeter (HCAL). The modules had to be directly oposite to each other or neighbouring to the opposite module (“1:3 scheme”) as described in the *CosmoALEPH Handbook* [54].

Cosmic ray muon measurements taken during normal ALEPH data taking periods of 1999 and 2000 were used to determine the *trigger efficiency* of the hadron calorimeter. The data selection, sketched in Figure 4.22, is as follows;

- at least one hit in the muon chambers and at least one hit in both the upper and lower modules of the HCAL. This represents a sample **N** of cosmic ray muon tracks.
- at least one hit in the muon chambers and at least eight hits in the upper and lower modules of the HCAL. This subsample **n** represents data taken with the CosmoALEPH trigger condition.

Figure 4.23 shows tracks of single cosmic ray muon events measured in the ALEPH detector with hits in the muon chambers, hadron calorimeter (HCAL)

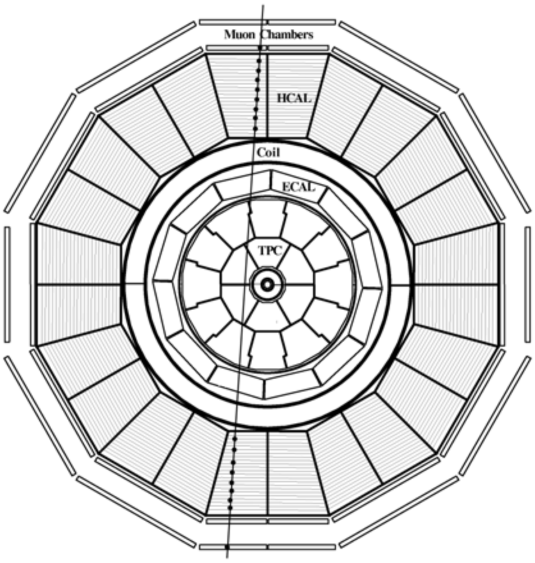

Figure 4.22: The CosmoALEPH trigger condition for measurement of cosmic ray muons in ALEPH. A detailed description is provided in [54].

and the time projection chamber (TPC).

The combination of at least one hit in the muon chambers and eight hits in the upper and lower parts of the hadron calorimeter ensures the selection of a data sample for cosmic ray muon events with tracks through the barrel of the hadron calorimeter only. Cosmic ray muon events with tracks through the *end-caps* of the hadron calorimeter are not considered in this analysis.

This is an essential requirement for the data taken during dedicated cosmic runs by CosmoALEPH. The ratio of these two data sets (n and N) provides an estimate of the trigger efficiency ε_{HCAL},

$$\varepsilon_{HCAL} = \frac{n}{N} \, , \tag{4.6}$$

as illustrated in Figure 4.24. The requirement of at least eight hits in both upper and lower modules of the hadron calorimeter reduces the number of cosmic ray muon tracks especially at high muon energies. The calculated trigger efficiency ε_{HCAL} is fitted by polynomials of the form,

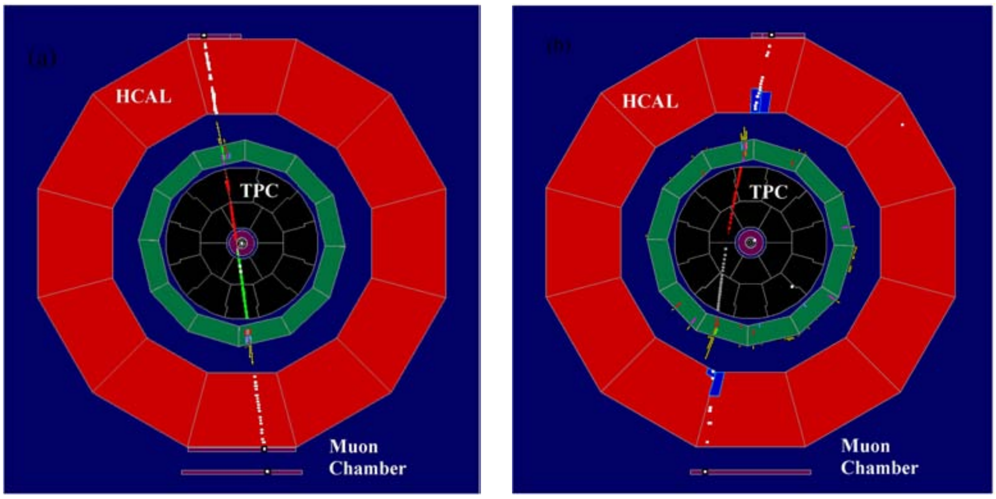

Figure 4.23: Cosmic ray muon events in ALEPH. Both tracks have hits in the muon chambers. Figure (a) shows a track with more than 8 hits in both modules the HCAL, while the track in Figure (b) has less than 8 hits in the lower modules of the HCAL.

$$p(n) = \sum_{i=0}^{n} A_i \, P_\mu^i \,, \tag{4.7}$$

where n is the order of the polynomial, A_i are the fit parameters and P_μ is the momentum of the muons measured in the TPC. The fit results are shown in Table 4.1

Table 4.1: Results of polynomial fit to the trigger efficiency of HCAL

$p(n)$	A_0	A_1	χ^2 /doF
$p(0)$	0.855 ± 0.006	–	0.710
$p(1)$	0.866 ± 0.007	-0.894 ± 0.003	0.209

The polynomial fits of the trigger efficiency take into account only the statistical uncertainties. The polynomial $p(0)$ represents a constant fit to the trigger efficiency of the HCAL. The calculated value $\varepsilon_{HCAL} = 85.6 \pm 0.6\%$ is in agreement with the documented value of 86% [9, 51] and also previous parameterisations based on detailed Monte Carlo simulations of the hadron calorimeter [4]. At higher muon momenta the value of the HCAL efficiency reduces significantly. A linear fit $p(1)$ provides a momentum-dependent correction to the measured data needed especially at higher muon momenta. Production of secondaries in the HCAL complicates the pattern recongnition hence a simple arithmetic calculation of the efficiency yields large uncertainties.

As already seen in the previous sections, muons lose energy as they propagate through matter. The total thickness of the HCAL corresponds to 7.16 interaction lengths, causing the muons to lose energy before they reach the TPC. The effect the CosmoALEPH trigger condition for low energy muons is investigated in this work. Figure 4.25 shows tracks of cosmic ray muons simulated in ALEPH. Both events are generated at a zenith angle of 10^0. The low energy muon (5 GeV) loses enough energy to be bent by the 1.5 Tesla magnetic field such that the track fails to meet the CosmoALEPH trigger condition. In order not to be sensitive to this effect, a minimum momentum of 10 GeV/c is applied in the analysis.

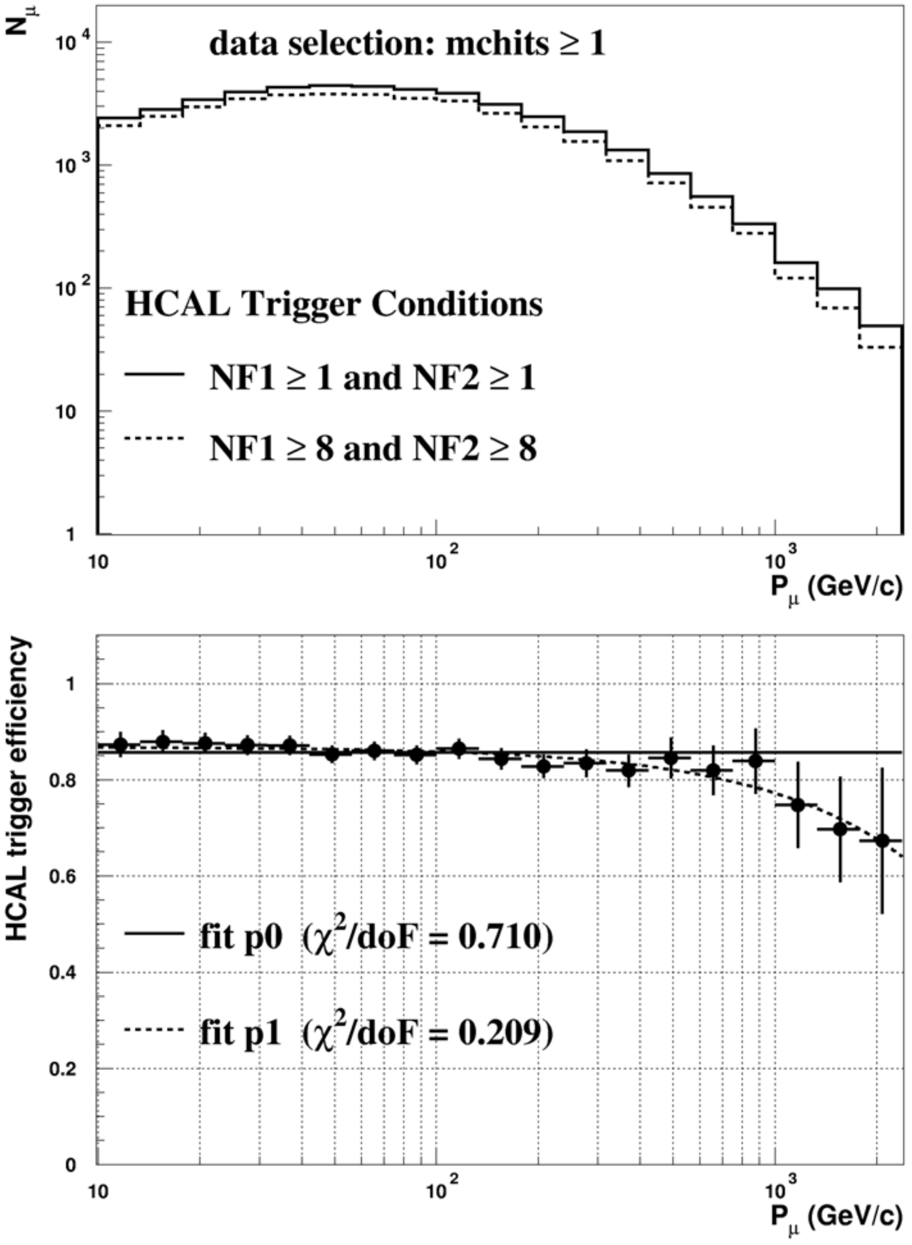

Figure 4.24: Calculation of Trigger Efficiency in HCAL. The term **mchits** denotes the number of hits in the muon chambers. **NF1** and **NF2** are the hits in the upper and lower modules of the hadron calorimeter respectively.

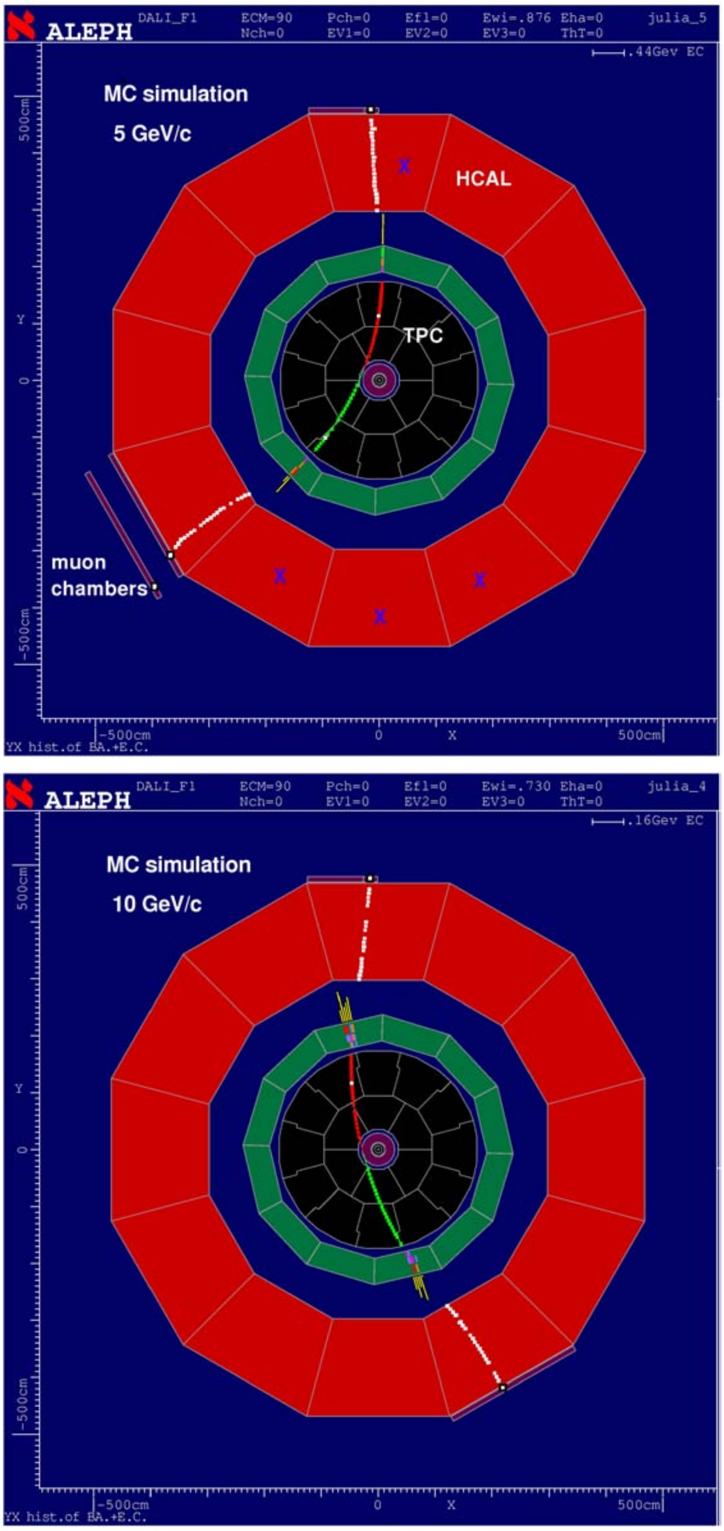

Figure 4.25: The track of a muon through the TPC. Note the 5 GeV/c muon bent out of the CosmoALEPH trigger condition marked by X

Chapter 5

Unfolding Experimental Data

A general formulation of the unfolding problem and a brief outline of the techniques to unfold experimental data is presented in this Chapter. Most of the concepts presented are based on the lecture notes [60]

5.1 Formulation of the Unfolding Problem

Experimental measurements are subject to statistical fluctuations and also systematic uncertainties due to factors such as detector resolution or non-uniform efficiency of the measurement apparatus. Apart from the statistical fluctuations, the measurements $a(x)$ can be described by a convolution of the true distribution $b(y)$ and the response function $g(x, y)$ of the measurement apparatus,

$$a(x) = \int dy \, g(x, y) \, b(y). \tag{5.1}$$

The function $g(x, y)$ describes how the apparatus responds to the measurements undertaken and includes typically effects like bias or efficiency of the measurement device(s) [60]. The aim of any measurement is to determine the true values or the true distribution of the values measured. This can be obtained by *unfolding* the measured distribution. This task is mathematically demanding but possible if one knows the response function. The relation (5.1) can be conveniently expressed in discrete form,

$$a_i = \sum R_{i,j}\, b_j \tag{5.2}$$

in which a_i is the vector containing the measured values and $R_{i,j}$ is the response matrix of the apparatus. Therefore, the problem of unfolding data is then reduced to solving the matrix equation (5.2) which can be inverted to obtain the true values b_j,

$$b_j = \sum (R_{i,j})^{-1}\, a_i. \tag{5.3}$$

This technique to unfold experimental data is known as *matrix inversion*. The detector response function or matrix can be effectively determined by:

- calibration experiments, if the true values are known, or,
- MC simulation based on physical processes in the detector.

In some practical or more complicated situations the response matrix is not a simple diagonal matrix, hence the inversion of such a matrix is relatively complicated. In some cases one needs some iterative procedures to obtain reasonable results.

5.2 Techniques to Unfold Data

There are a variety of techniques that can be used to unfold data from experimental measurements. Following is a brief description of the techniques considered in this work.

5.2.1 Correction Factors

The method of applying *correction factors* to a set of measurements is the simplest and widely used technique to unfold data from simple measurements. This method requires, however, a knowledge of the true distribution. The correction factors c_k are obtained by dividing the true distribution to the measured distribution,

$$c_k = \frac{b_i}{a_j}\,, \tag{5.4}$$

so that a multiplication of the actual measurements with the correction factors yields the *corrected distribution* [60]. The correction factors, also referred to as *bin-to-bin corrections*, depend explicitly on the assumption about the true distribution (Equation 5.1),

$$c_k = \frac{b_i}{\sum R_{i,j}\, b_j}. \tag{5.5}$$

It is important to note that the correction factors are only valid if the assumed input true values are identical to the physical truth. In the extreme case where $b_i = 0$, the correction factor is also zero and the measured values are simply ignored. This may cause loss of information. One solution here is to work out the correction factors iteratively.

5.2.2 Regularisation

The calculation of the correction factors iteratively is, to some approximation, a matrix inversion procedure provided the unfolded distribution is positive. However, this kind of inversion often enhances statistical fluctuations which result in an *amplification* of the noise in the measurements. Expressing the unfolding problem in an appropriately chosen basis, the technique of *Regularisation* ignores the correction factors dominated by such noise.

5.2.3 Reduced Cross Entropy

The method of reduced cross entropy (MRX) assumes a prior knowledge of the shape of the true distribution to counteract the statistical fluctuations in a consistent manner [61]. This is achieved by a probability distribution p proportional to the true distribution $b = N\, p$, which is consistent with the measured data and at the same time deviates as little as possible from an assumed prior distribution ϵ. The agreement with the experimental data is quantified by,

$$\chi^2 = (a \,-\, G\, b)^T\, C^{-1}\, (a \,-\, G\, b)\,, \tag{5.6}$$

where C is the covariance matrix of the measurement a. The deviation from the prior distribution ϵ is measured by the so-called *cross-entropy*,

$$S = \sum p \ln \frac{p}{\epsilon} \,. \tag{5.7}$$

To satisfy both conditions at the same time, minimisation of the linear combination,

$$F = S + w\,\frac{\chi^2}{2}\,, \tag{5.8}$$

is used to determine the unfolded distribution. The parameter w is known as the *regularisation parameter* and it is used to adjust the relative weights of the measurements with respect to the cross entropy term S. From Equation 5.8, two distinct situations are then possible,

- in the limit $w \to \infty$ leads to the *Method of Minimum Cross Entropy (MMX)* ,
- for $\epsilon =$ constant leads to the *Method of Maximum Entropy (MME).*

It is also important to note that Equation 5.8 reduces to the *least squares method* for very small measurement errors or large regularisation parameter w. The *Method of Reduced Cross Entropy (MRX)* combines the principle of least squares and the method of minimum cross entropy. A detailed description is provided elsewhere [61].

5.2.4 Bayesian Unfolding

This method is based on Bayes' theorem [63], which can be expressed using the above notations in the form of conditional probabilities,

$$\mathrm{P(true\,i\,|\,observed\,j)} = \frac{\mathrm{P(observed\,j\,|\,true\,i)\,\cdot\,P(true\,i)}}{\sum_{\mathrm{i}}\mathrm{P(observed\,j\,|\,true\,i)\,\cdot\,P(true\,i)}}\,, \tag{5.9}$$

that the true value is in bin i if the observed value is in bin j. This allows to correct for smearing effectts described by the response matrix. Taking into account the efficiencies, ϵ_i, the expected number of events observed corresponding to each of the true event is thus,

$$b_i \;=\; \frac{\sum_j \mathrm{P(true\,i\,|\,observed\,j)}\; a_j}{\epsilon_i} \;= \sum_j \; R_{ij}\, a_j \;, \tag{5.10}$$

The conditional probabilities can be used to construct the two-dimensional *unfolding matrix* $R_{i,j}$. The unfolding problem therefore involves an iterative process to estimate the true distribution x_i as follows,

$$b_i^{k+1} = \frac{1}{\sum_{j=1}^{m} R_{ji}} \sum_{j=1}^{m} \frac{R_{ji} b_i^k}{\sum_{l=1}^{n} R_{jl} b_l^k} a_j \;, \tag{5.11}$$

where b_i^k is the estimated solution after k iteration steps. This method, like the others, clearly depends on the number of iterations involved and the condition(s) to stop the iterations.

5.3 Test of the Algorithms to Unfold Data

It is important to test any algorithm before applying it to real data analyses. The Monte Carlo simulations described in Chapter 4, have provided the momentum distributions for the true and also reconstructed cosmic ray muon events, from which response matrix of the detector has been constructed. This matrix describes all the detector effects like momentum resolution, digitisation of the signals from the measurements of cosmic ray muons. The large scattering of the matrix is due to the fact that at high momenta the resolution is rather poor.

As an example, using the response matrix shown in Figure 5.1 the reconstructed Monte Carlo generated events are unfolded using the Bayes' technique described in the previous sections. The aim here is to test the accuracy of the algorithms used for the unfolding techniques.

The results of the above tests show that the algorithm is accurate and can be applied to unfold data distributions. Unfolding of the data is essential for measurements done using the entire area of the TPC. However, if the measurements are confined to the central part of the TPC, the deviations of the measured events from the Monte Carlo truth are much less as observed in Figure 5.1.

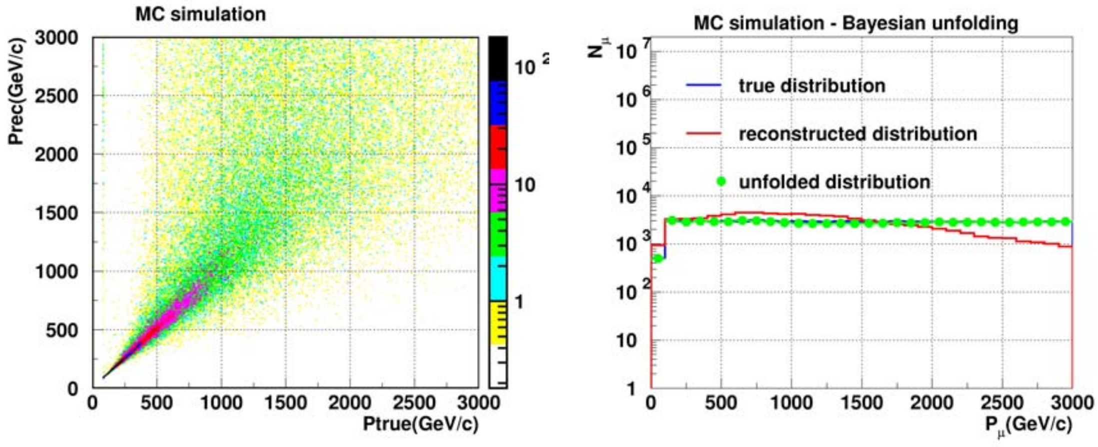

Figure 5.1: Application of Bayesian unfolding to Monte Carlo data set from the central part of the TPC.

The data shown in Figure 5.1 are a set of the cosmic ray muons uniformly generated in the TPC. The purpose was to determine the performance of the TPC for measurements of cosmic ray muons with high statistics at high energies. In oder to study the response of the TPC to cosmic ray muons, the uniformly distributed data are weighted by $E^{-\gamma}$, with a spectral index $\gamma = 2.7$. This is an approximation which corresponds to the form of the all-particle cosmic ray spectrum. The scaled data are shown in Figure 5.2. For muons accepted by the analysis, the true and the reconstructed momentum spectra are displayed. The ratio of these two spectra, shown in Figure 5.3, gives the correction factors for momentum smearing for the central part of the TPC. The deviations of the measured events from the truth are only small, i.e within $\pm 10\%$ and hence do not neccessarily require advanced unfolding techniques to correct the data. The bin-to-bin corrections have therefore been applied to correct the measured data.

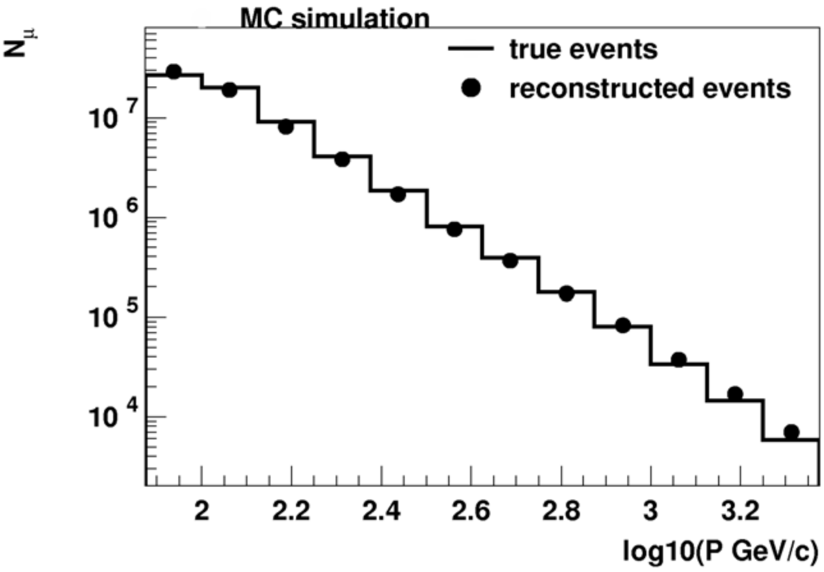

Figure 5.2: Reconstruction of muon events in the TPC.

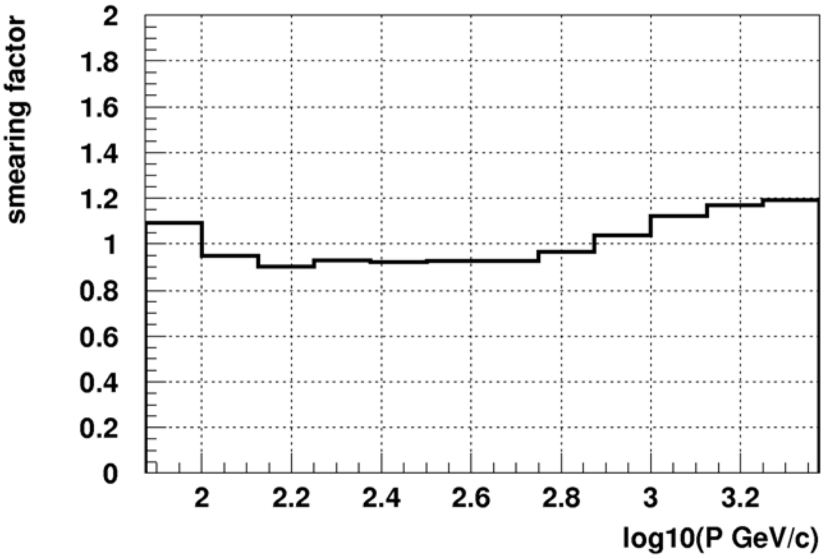

Figure 5.3: Response of the ALEPH TPC to measurements of cosmic ray muons.

.

Chapter 6

Momentum Spectrum and Charge Ratio

The momentum and charge ratio of the measured cosmic ray muons measured are presented in this Chapter. A comparison is made with the expectations from Monte Carlo Simulations and other measurements.

6.1 Calculation of the Muon Flux

The data selection in this work is based on the following criteria,

- muon momentum, $P_\mu \geq 10\,\mathrm{GeV/c}$,
- momentum uncertainty $dP/P \leq 1$,
- zenith angle, $\theta \leq 20^0$
- TPC fiducial area, $|x| \leq 50\,\mathrm{cm}$, $20 \leq |z| \leq 200\,\mathrm{cm}$

The flux calculated using these criteria is used as the reference flux Φ_0 in the evaluation of the systematic uncertainties described in Section 6.2. The momentum distribution of the cosmic ray muons measured in this work in Figure 6.1. The muon momenta at the surface are obtained by an extrapolation of the momenta measured in ALEPH using Equation 2.31. At low momenta, $P \leq 100$ GeV/c, the muons lose a large fraction of their energy due to ionisation. The energy cut-off (80 GeV) for CosmoALEPH also leads to the low number of muons measured at those energies.

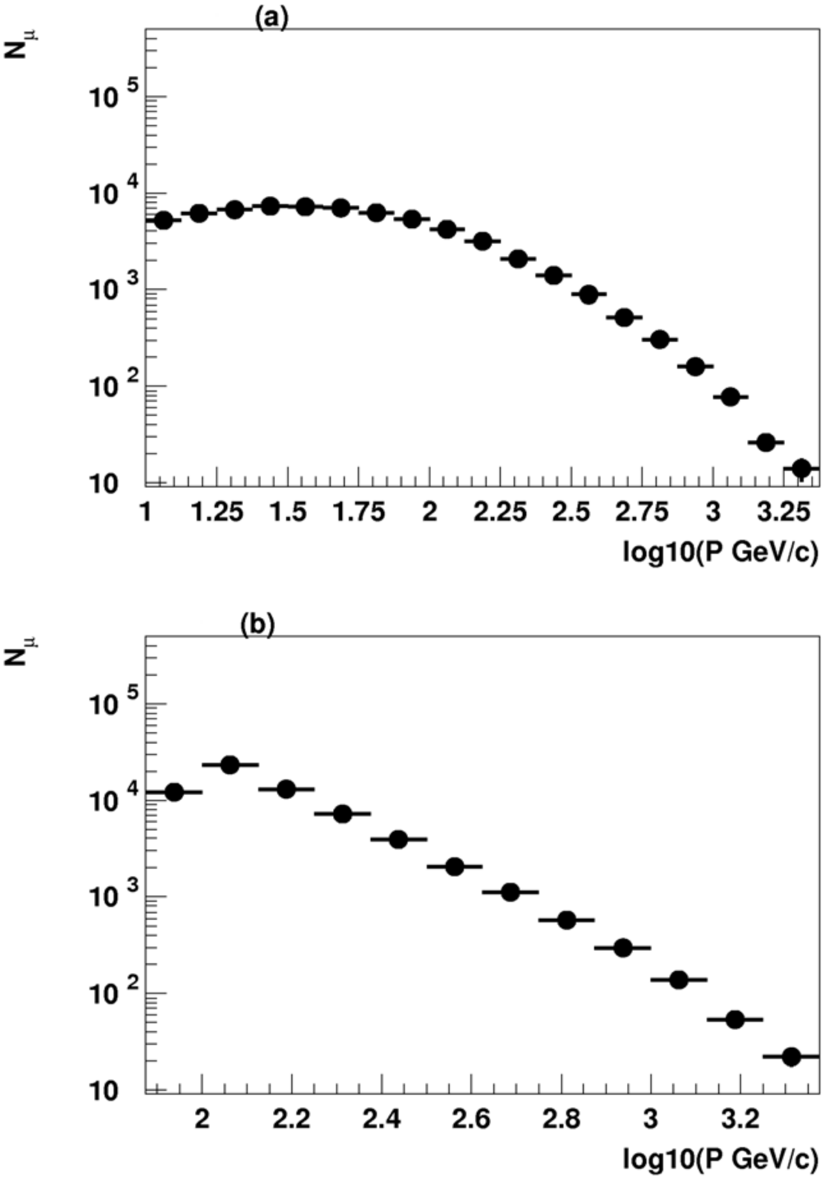

Figure 6.1: Momentum distribution of the cosmic ray muons (a) measured in ALEPH (b) extrapolated to the surface.

The muon flux Φ_μ is calculated from the momentum distribution of the muons extrapolated to the surface Figure 6.1 (b) as follows,

$$\Phi_\mu = \frac{N_\mu(p, p + \Delta p)}{\varepsilon_{\text{trig.}} \cdot \varepsilon_{\text{rec.}} \cdot \Delta t \cdot S_{\text{eff}} \cdot \Omega \cdot \Delta p}\,, \tag{6.1}$$

where, $N_\mu(p, p+\Delta p)$ is the number of muons with momentum within $(p, p+\Delta p)$ at the surface, $\varepsilon_{\text{trig.}} = (85.5 \pm 0.6)\%$ is the trigger efficiency of HCAL as described in Section 4.4, $\varepsilon_{\text{rec.}}$ is the track reconstruction efficiency in the TPC as described in Section 4.3.5.

For measurements of cosmic ray muons up to $\theta = 20^0$ in zenith angle, the solid angle Ω is calculated by,

$$\Omega \;=\; 2\,\pi \int_0^{20} \sin\theta \,\mathrm{d}\theta \;= 0.379\,\text{sr}. \tag{6.2}$$

The effective run time for data taking, Δt, is obtained from the following considerations. From the measured trigger rate of (2.53 ± 0.126) Hz and the effective area of the HCAL (10.4 ± 0.3)m^2, the measured integrated flux of cosmic ray muons in CosmoALEPH is $F = 0.243 \pm 0.014$ Hz/m^2 [68]. The effective area for the central part of the TPC corresponds to $S_{\text{eff}} = 3.6\,\text{m}^2$. The effective run time Δt is therefore obtained by;

$$\Delta t \;=\; \frac{N_0 \,/\, \varepsilon_{\text{trig}}}{S_{\text{eff}} \;\cdot\; F} \;=\; \frac{291803 \,/\, 0.855}{3.6m^2 \;\cdot\; 0.243\,\text{Hz}\,\text{m}^{-2}} \;=\; 4.51\,\text{days}. \tag{6.3}$$

N_0 respresents the total number of cosmic ray muon events with at least one track reconstructed in the central part of the TPC. Here no restrictions in the minimum momenta, momentum resolution or zenith angles apply. The efficiency for these tracks is close to 100 %. Substituting Equation 6.3 into Equation 6.1 yields,

$$\Phi_\mu = \frac{N_\mu(p, p + \Delta p) \;\cdot\; F}{\varepsilon_{\text{rec}} \;\cdot\; N_0 \;\cdot\; \Omega \;\cdot\; \Delta p} \tag{6.4}$$

which is used to for the calculations of the muon flux. The efficiency $\varepsilon_{\text{rec.}}$ is a product of the track reconstruction efficiency and the smearing factors shown in Figures 4.21 and 5.3 respectively.

6.2 Evaluation of the Uncertainties

Measurement of the cosmic ray muon flux is associated with both statistical and systematic uncertainties. The relative size of the statistical errors is given by,

$$\frac{\sigma_{stat}}{N} = \frac{1}{\sqrt{N}} \, . \tag{6.5}$$

The data selection criteria are systematicaly varied as indicated in the Table 6.1 with the aim to investigate the systematic effects on the calculated muon spectrum.

Table 6.1: Variation of the data selection criteria

Data selection criteria		Systematic variation
zenith angle	$\theta \leq 20^0$	$\pm\ 1^0$
momentum uncertainty	dP/P ≤ 1	$\pm$ 0.1
minimum momentum	$P_\mu \geq 10$ GeV/c	$\pm$ 1.0 GeV/c
fiducial area of the TPC	$\lvert x\rvert \leq 50$ cm	$\pm$ 1 cm
	$\lvert z\rvert \geq 20$ cm	$\pm$ 1 cm
	$\lvert z\rvert \leq 200$ cm	$\pm$ 1 cm

In addition, the systematic uncertainties related to the extrapolation of the muon energies to the surface are investigated. This is achieved by varying the thickness of the overburden R = 325.3 ± 7 m.w.e. and also by using the parametrised values of a and b described in Equations 2.28 and 2.29 respectively. The systematic variation of the data selection criteria and the thickness of the overburden yield two estimates of the flux, Φ_j^+ and Φ_j^-, so that the average flux from each set of the systematic variations is,

$$\bar{\Phi}_j = \frac{1}{3}\left(\Phi_0 + \Phi_j^+ + \Phi_j^-\right) \tag{6.6}$$

with Φ_0 as the measured reference flux obtained from the data selection criteria described in Section 6.1. In the calculations of the fluxes Φ_j^+ and Φ_j^-, considerations are made to use the correct values of the solid angle Ω and the

TPC fiducial area as required by Equation 6.4. The uncertainties σ_j are then evaluated by,

$$\sigma_j = \sqrt{\frac{1}{n-1}\sum_{i=1}^{n}(\Phi_i - \bar{\Phi}_j)^2} \qquad (n = 3)\,, \tag{6.7}$$

with $n = 2$ for the case of the parameterisation of a and b. The results are illustrated in Figure 6.2.

The components σ_j of the systematical uncertaintainties, described in Table 6.1 are added quadratically,

$$\sigma_{syst.} = \sqrt{\sum_{j=1}^{6}\sigma_j^2} \tag{6.8}$$

as illustrated in Figure 6.2. The total uncertainties are a quadratic sum of the systematic and statistical uncertainties,

$$\sigma_{total} = \sqrt{\sigma_{stat.}^2 \;+\; \sigma_{syst.}^2} \tag{6.9}$$

as illustrated in Figure 6.3.

The various contributions to the systematic uncertainties, illustrated on Figure 6.2, are mostly within ±10% with the exception of the choice of the minimum momentum at 10 GeV/c and also the measurement uncertainties. The systematic variation of the minimum momentum affects only the low energy muons mainly due to the significant energy losses at those momenta. The other important aspects are the thickness of the overburden and also the propagation of the muon energies to the surface. In both cases they contribute to larger systematic uncertainties at lower momenta. At higher momenta the measurement resolution dominates the contribution of the systematic uncertainties. Statistical uncertainties dominate at higher momenta.

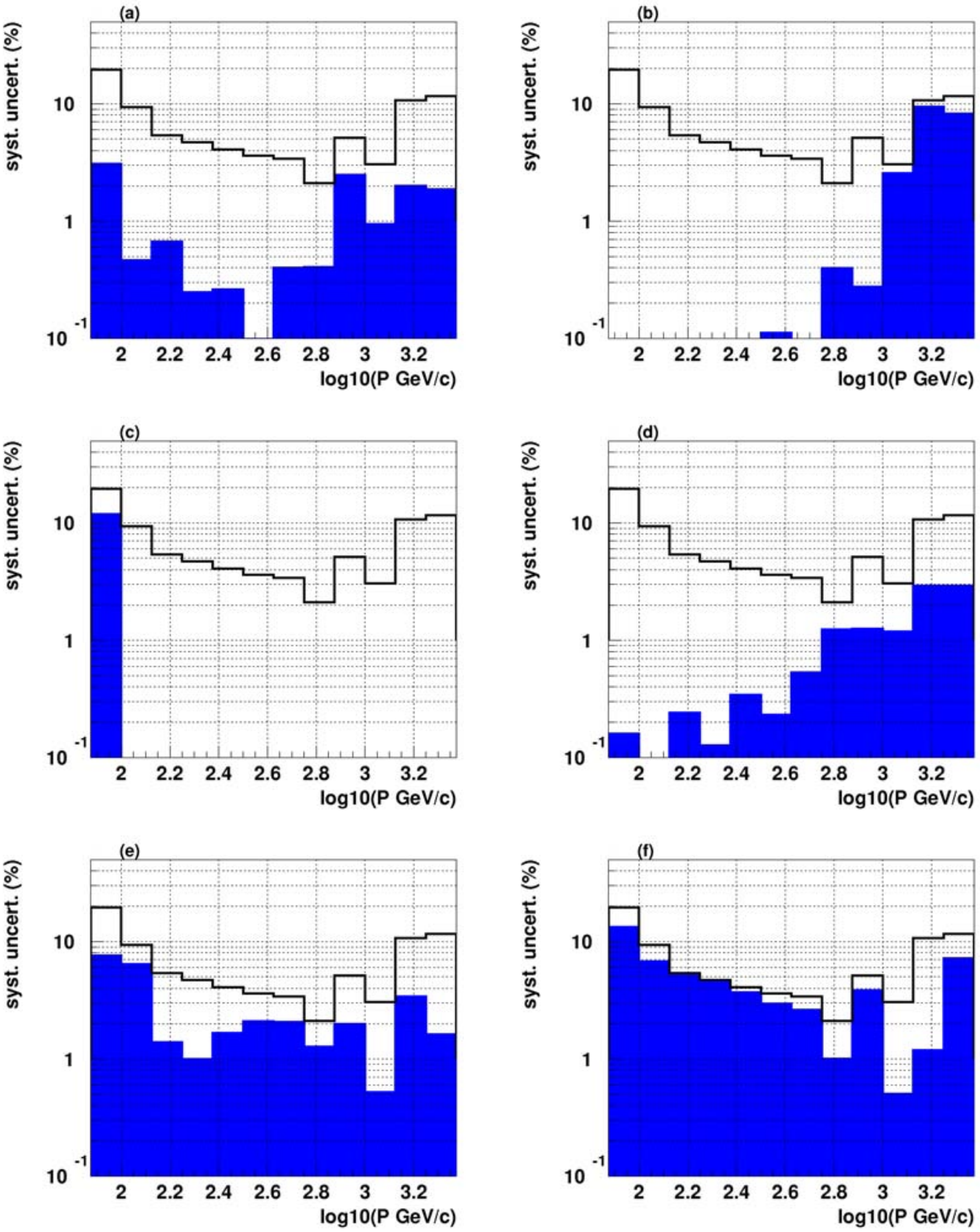

Figure 6.2: The systematic uncertainties on the muon flux. The shaded areas represent the contributions due to (a) zenith angle, (b) measurement uncertainties, (c) minimum momentum, (d) TPC area, (e) approximation of the energy-loss parameters, (f) the thickness of the overburden. The solid line represents the quadratic sum of all the systematic uncertainties as described by Equation 6.8.

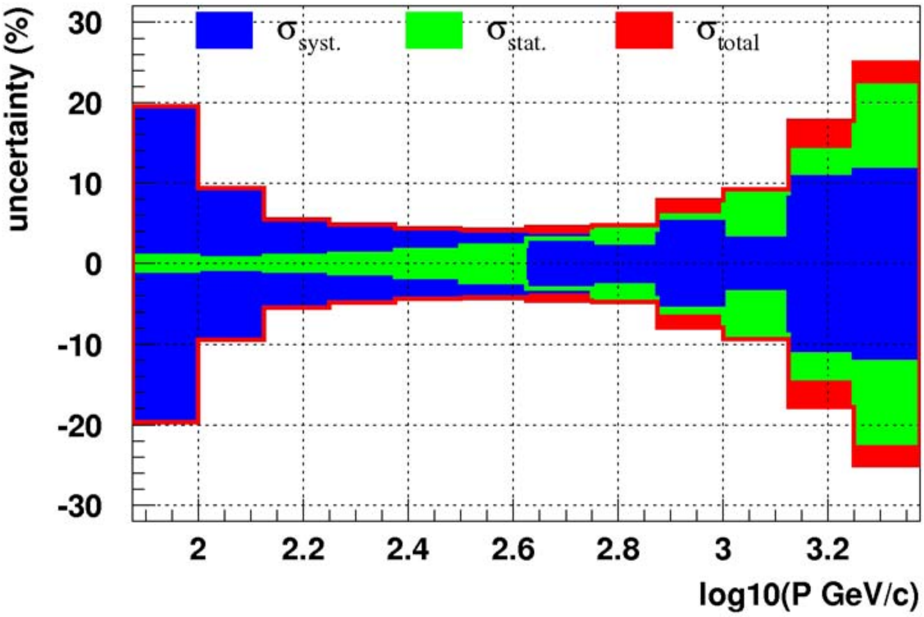

Figure 6.3: Systematic and statistical uncertainties on the calculated muon flux. The total systematic uncertainty is a quadratic sum of the systematical and statistical uncertainties as described by Equation 6.9.

6.3 The Momentum Spectrum

The values of the muon flux are shown in Table 6.2 and in Figure 6.4. The error bars indicate the quadratic sum of the systematic and statistical uncertainties which are shown in Table 6.2.

Table 6.2: The cosmic ray muon flux measured in this work. The momentum ranges are indicated in the brackets.

Momentum		Flux Φ_μ	$\pm\Delta\Phi_\mu$
P_μ GeV/c	log10(P_μ)	—— $(\text{s cm sr GeV/c})^{-1}$ ——	
115 (100 − 133)	2.02	0.154E − 06	± 0.014E − 06
154 (134 − 177)	2.19	0.642E − 07	± 0.035E − 07
205 (178 − 237)	2.31	0.266E − 07	± 0.012E − 07
274 (238 − 316)	2.44	0.108E − 07	± 0.005E − 07
365 (317 − 421)	2.56	0.425E − 08	± 0.018E − 08
487 (422 − 562)	2.69	0.174E − 08	± 0.080E − 9
649 (563 − 750)	2.82	0.680E − 09	± 0.032E − 9
865 (751 − 1000)	2.94	0.2616E − 09	± 0.021E − 9
1154 (1001 − 1334)	3.06	0.915E − 10	± 0.085E − 10
1539 (1335 − 1778)	3.19	0.267E − 10	± 0.047E − 10
2053 (1779 − 2371)	3.31	0.814E − 11	± 0.203E − 11

As already observed in the azimuth-zenith angle distributions, the momentum spectrum calculated up to 20^0 in zenith angles needs no further corrections for geometrical acceptance and/or effects of the angular distribution around the vertical. The error bars do not include a global normalisation uncertainty of $\approx 6\%$ resulting from the error in the measured integral flux $F = 0.243 \pm 0.014\,\text{Hz/m}^2$. The statistical errors on the correction factors $\varepsilon_{\text{rec.}}$ are negligible due to the fact that the Monte Carlo data set is large. In Figure 6.5 measured spectrum is compared with data from previous experiments, a prametrisation of the cosmic ray muon data [14] and the analytical approximations described by Equations 2.22 and 2.21.

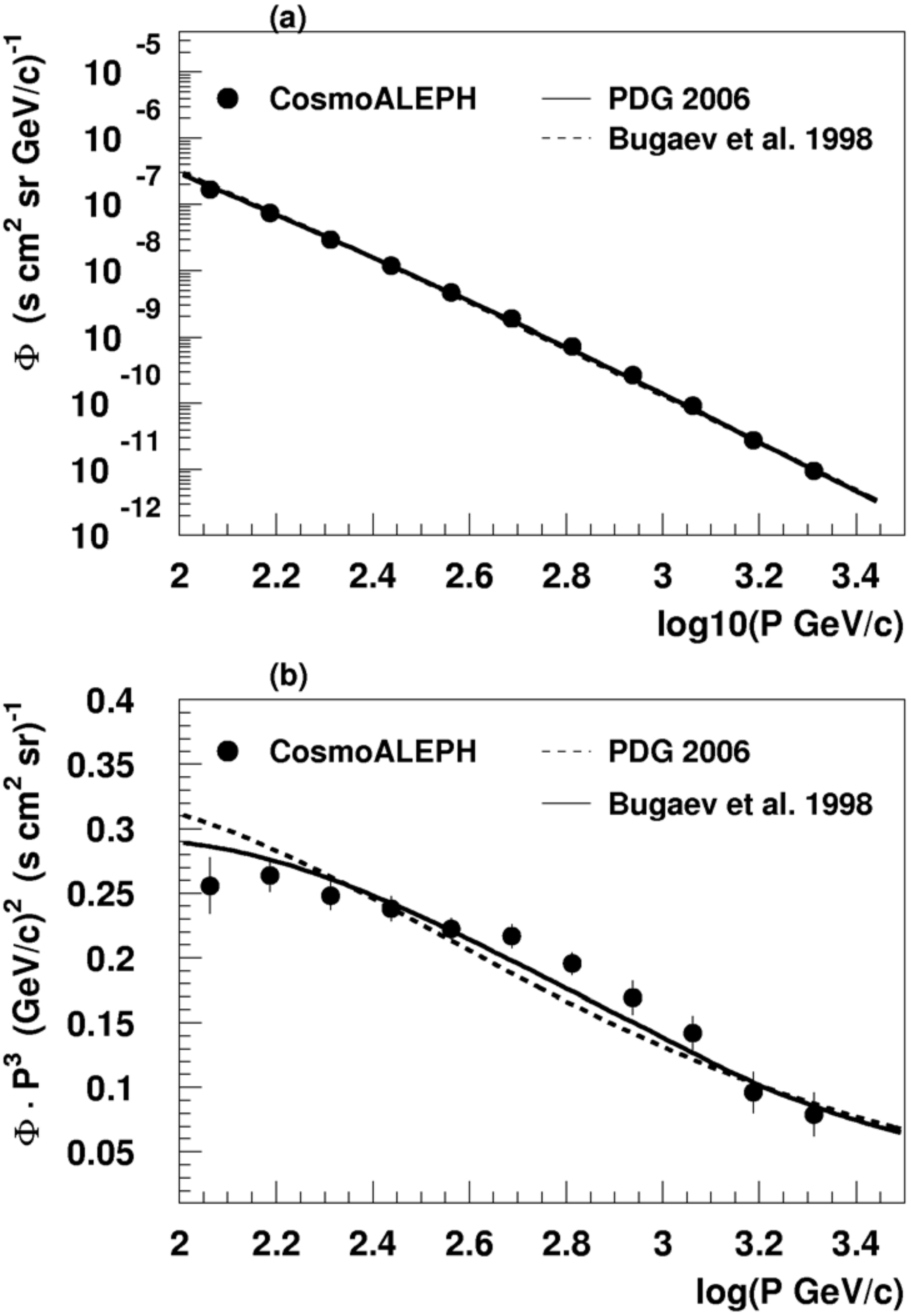

Figure 6.4: The flux of cosmic ray muons at the surface. The solid and dashed lines illustrate the analytical forms described by the Equations (2.22 and 2.21) respectively. The data are scaled with P^3 in order to illustrate the form of the flux. The error bars indicate the quadractic sum of systematic and statistical uncertainties.

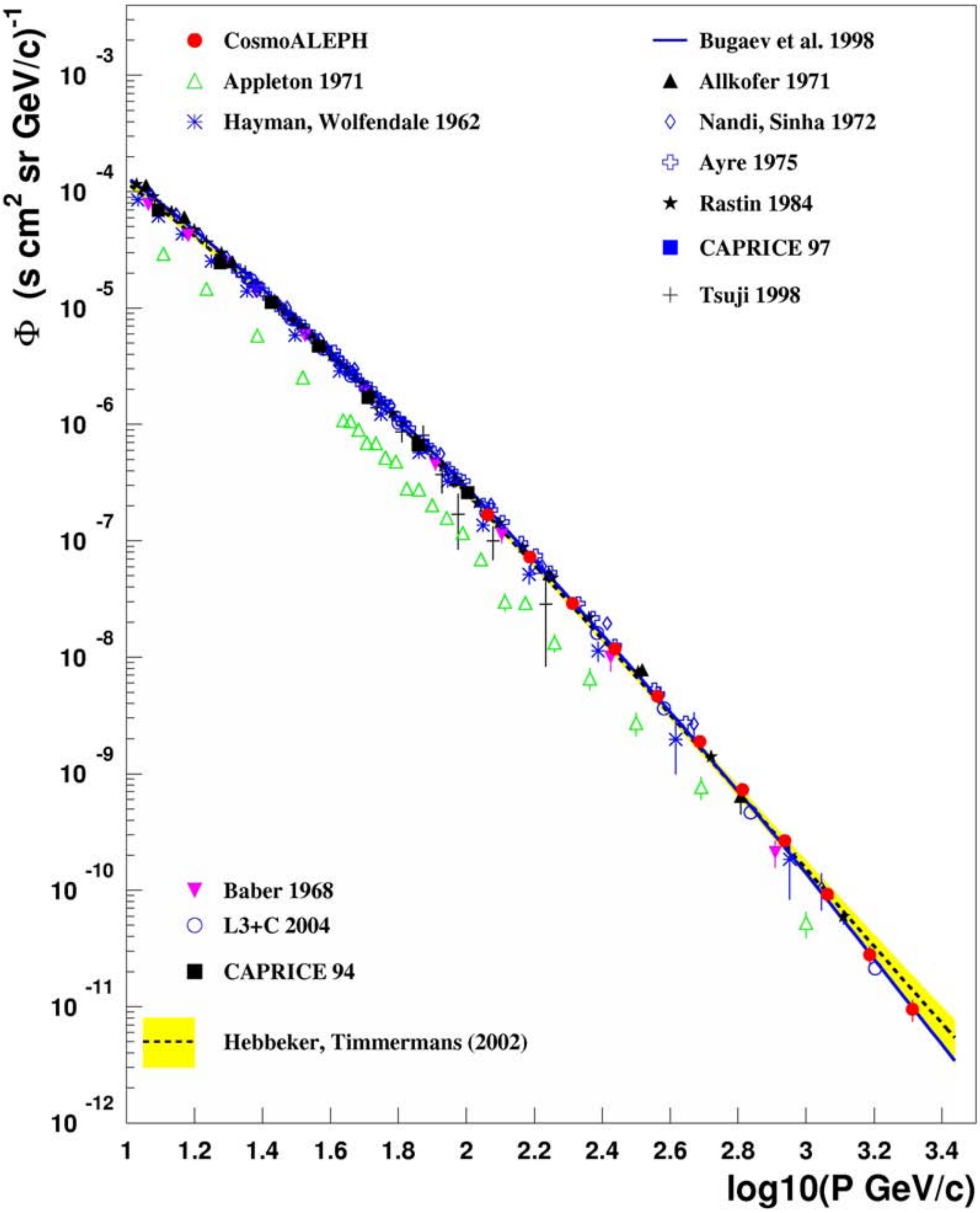

Figure 6.5: The momentum spectrum for vertical muons. The data are compared with the results of previous experiments compiled in [14] and analytical parameterisations [62].

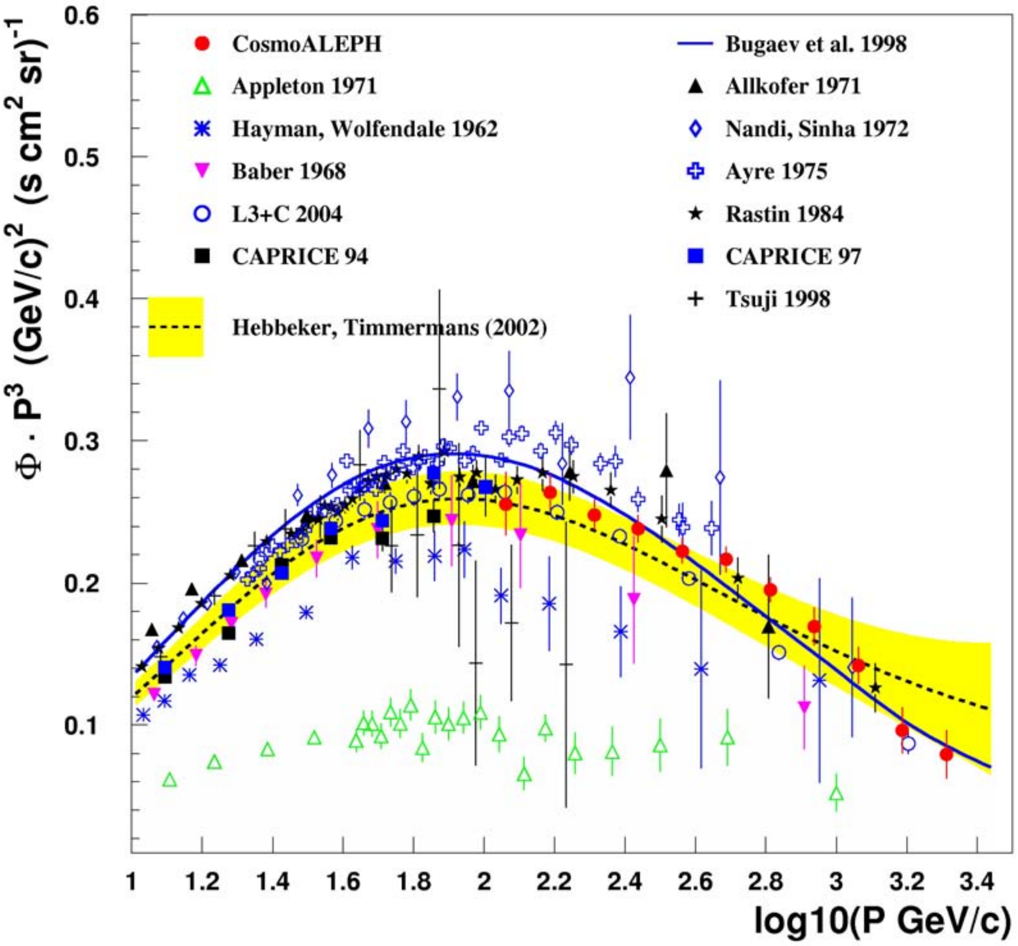

Figure 6.6: The momentum spectrum for vertical muons. The data are scaled with P^3 in order to illustrate the fine details of the spectrum. The data are compared with the results of previous experiments compiled in [14] and analytical parameterisations [62].

6.4 The Charge Ratio

Figure 6.7 shows the charge ratio of cosmic ray muons measured for zenith angles $\theta \leq 20^0$. The average value in the momentum range 80 to 2500 GeV is $R_\mu = 1.249 \pm 0.05$ with only statistical errors. Systematic uncertainties are expected to be below 10%.

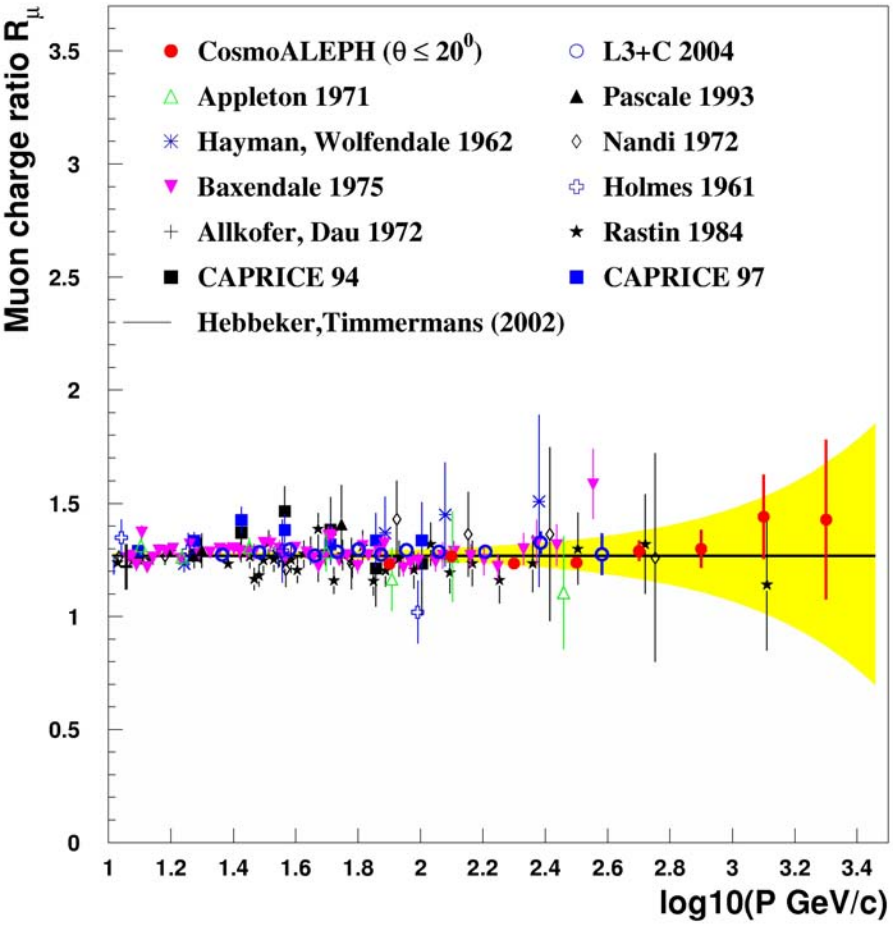

Figure 6.7: The charge ratio for vertical muons $\theta \leq 20^0$. The yellow band represents uncertainties in the parameterised of charge ratio [14]. Refrences to the data are contained in [14].

The charge ratio measured in this work is consistent with the other measurements described in [14].

The charge ratio for cosmic ray muons measured at zenith angles $\theta \leq 50^0$ is shown in Figure 6.8. The average value obtained is $R_\mu = 1.2253 \pm 0.003$ with only statistical errors. Table 6.3 shows the measured values of the charge ratios.

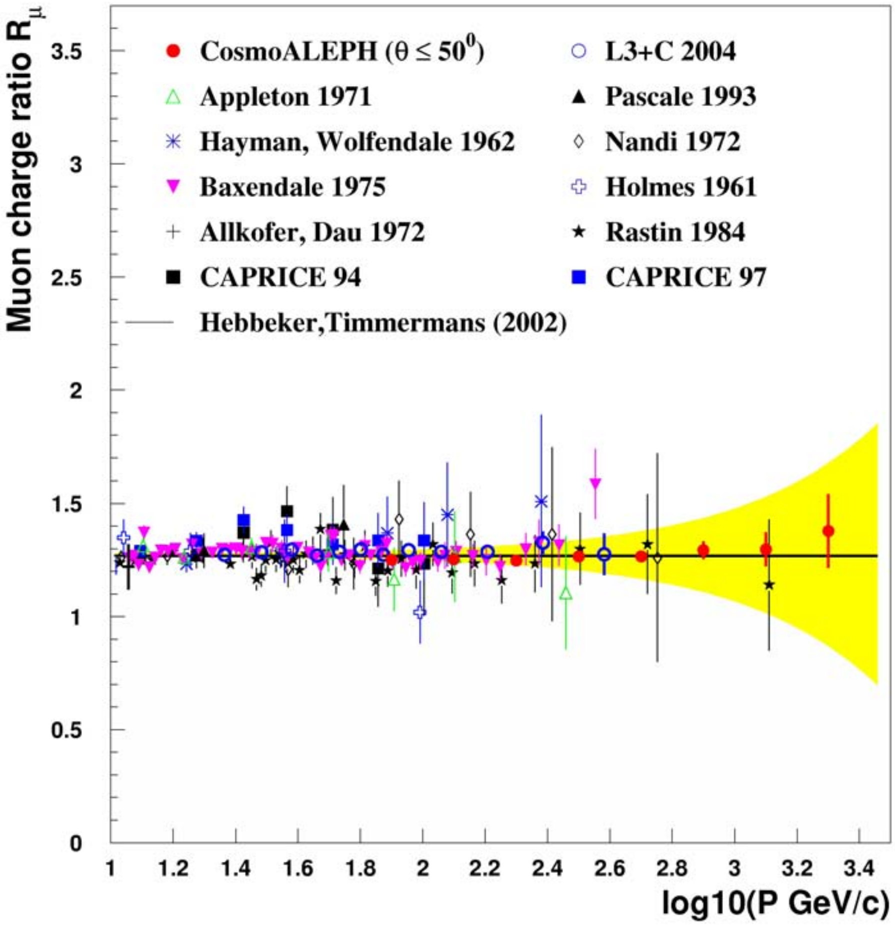

Figure 6.8: The charge ratio for inclined muons $\theta \leq 50^0$. The yellow band represents uncertainties in the parameterised of charge ratio [14]. Refrences to the data are contained in [14].

Table 6.3: The charge ratio of cosmic ray muons measured in this work. Only statistical uncertainties are indicated.

Momentum P_μ GeV/c	$\log10(P_\mu)$	Charge ratio R_μ $\theta \leq 20^0$	$\pm \Delta R_\mu$ $\theta \leq 50^0$
79 (63 − 133)	1.9	1.233 ± 0.09	1.251 ± 0.007
126 (100 − 157)	2.1	1.266 ± 0.08	1.253 ± 0.004
200 (158 − 250)	2.3	1.234 ± 0.014	1.247 ± 0.006
316 (251 − 397)	2.5	1.238 ± 0.024	1.266 ± 0.011
501 (398 − 630)	2.7	1.291 ± 0.045	1.266 ± 0.020
794 (631 − 999)	2.9	1.300 ± 0.084	1.293 ± 0.039
1259 (1000 − 1584)	3.1	1.441 ± 0.186	1.298 ± 0.076
1995 (1585 − 3162)	3.3	1.429 ± 0.352	1.379 ± 0.163

6.5 Comparisons with MC Simulations

It is essential to compare the measured data with the theoretical expectations. A comparison of the preliminary data with the Monte Carlo Simulations based on different hadronic interaction models is shown in Figure 6.9.

The aim is to investigate the shape of the distributions. The models describe the momentum distribution of the measured cosmic ray muons measured. The slope of the number of muons at the surface predicted by the models agrees very well with our data. However, some systematic effects of different hadronic interaction models are evident in the calculations of the charge ratio as shown on Figure 6.10. SIBYLL, which is known to generate a relatively lower muon content[69, 70], shows systematically higher values for the muon charge ratio compared to the measurements inthis work. A similar trend is observed by the L3+C experiment at the LEP [71]. In Figure 6.11 the measured charge ratio is compared with results of Monte Carlo simulations based on the recently available models EPOS, NEXUS and QGSJET II.

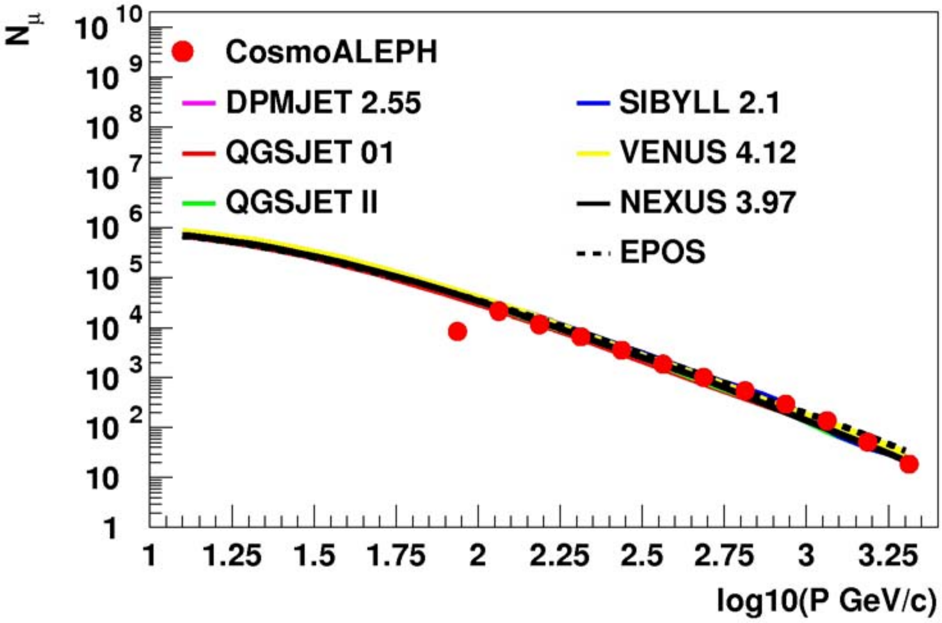

Figure 6.9: The measured momentum distribution compared with Monte Carlo simulations based on different models. Note the drop at low momenta $P \leq 100 GeV/c$ due to the energy cut-off (80 GeV) for the CosmoALEPH experiment.

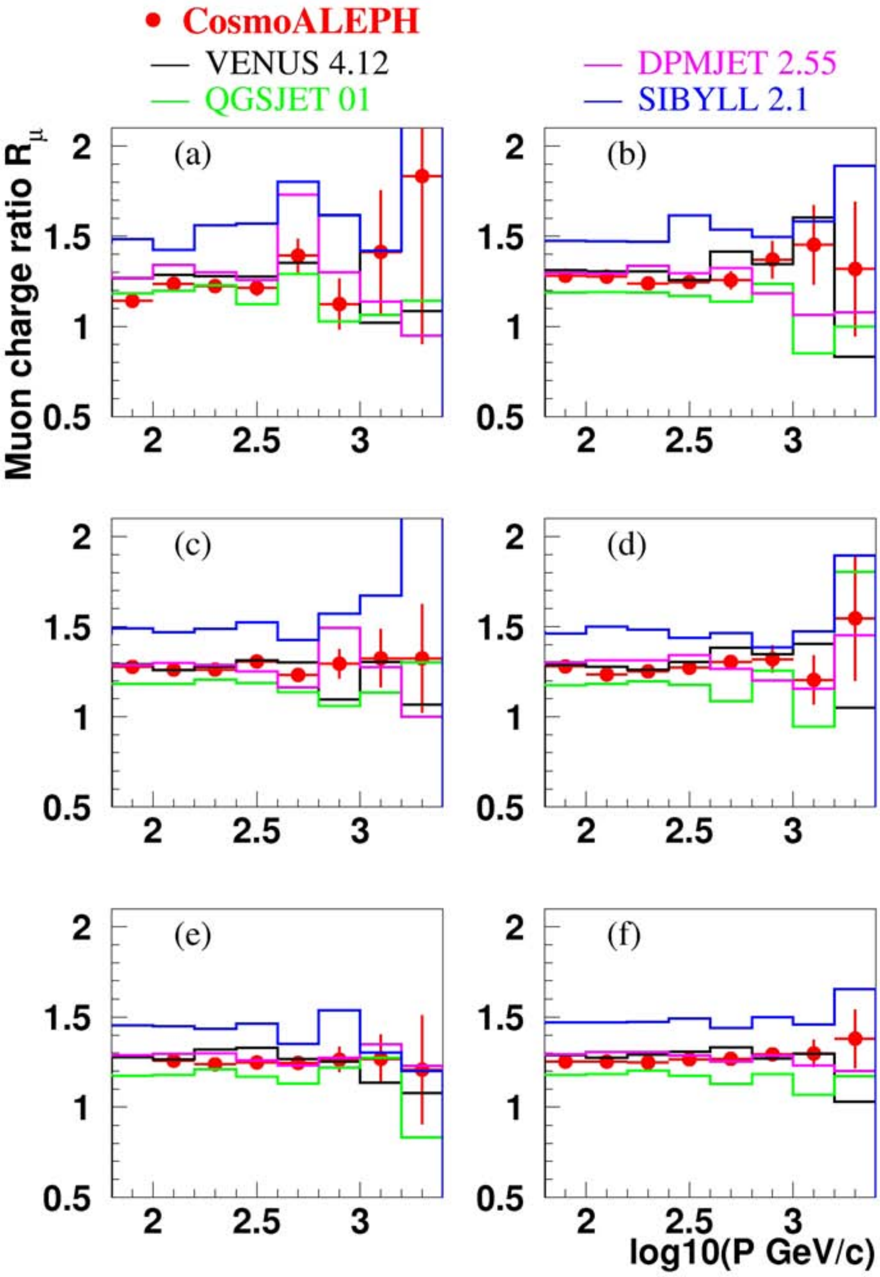

Figure 6.10: The charge ratio measured at zenith angles (a) $\theta \leq 10^0$, (b) $10^0 < \theta \leq 20^0$, (c) $20^0 < \theta \leq 30^0$, (d) $30^0 < \theta \leq 40^0$, (e) $40^0 < \theta \leq 50^0$, (f) $\theta \leq 50^0$. A comparison is made with MC Simulations based on different hadronic interaction models

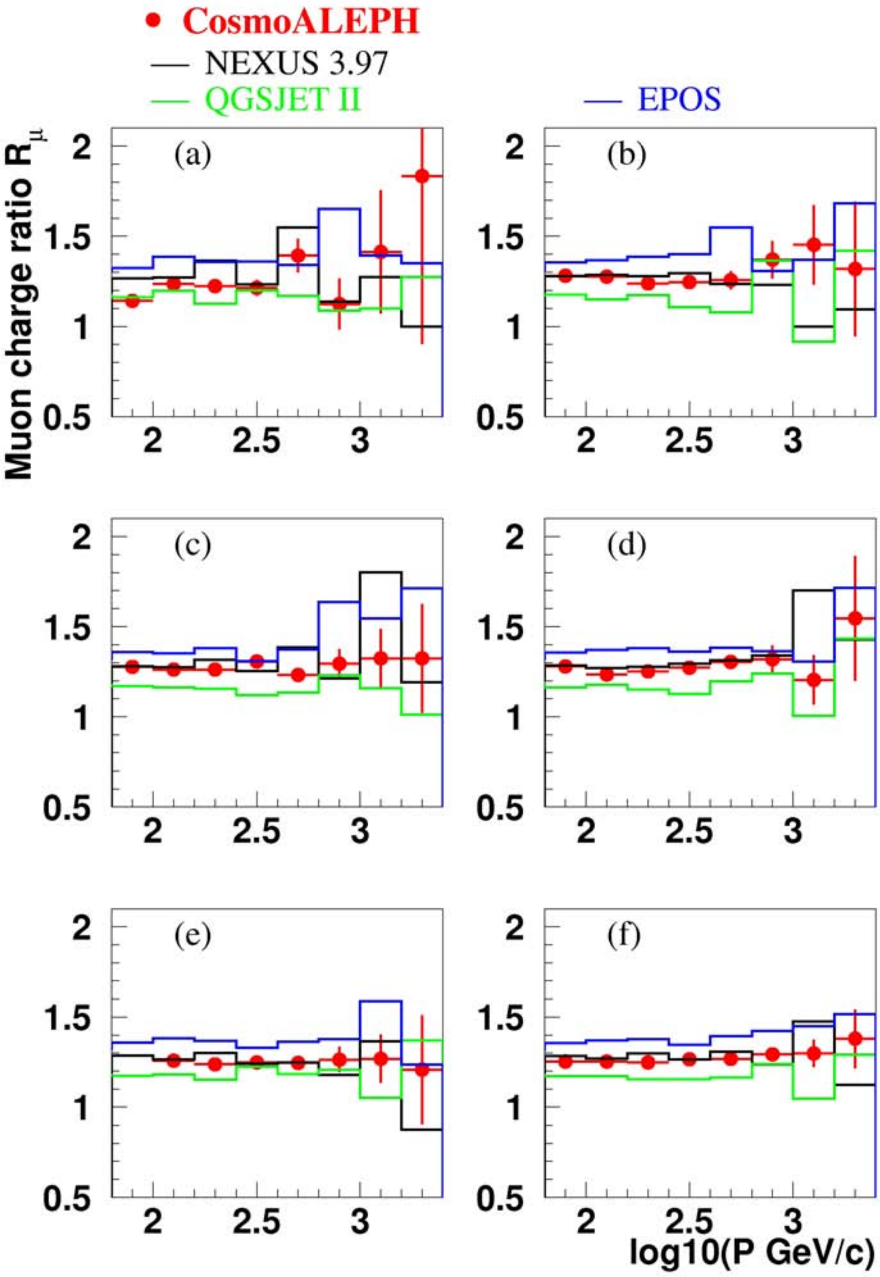

Figure 6.11: The charge ratio measured at zenith angles (a) $\theta \leq 10^0$, (b) $10^0 < \theta \leq 20^0$, (c) $20^0 < \theta \leq 30^0$, (d) $30^0 < \theta \leq 40^0$, (e) $40^0 < \theta \leq 50^0$, (f) $\theta \leq 50^0$. A comparison is made with MC Simulations based on different hadronic interaction models

The Monte Carlo simulations are in progrss to increase the statistics. There is no clear trend for the charge ratio at different zenith angles. This motivates a comparison of the charge ratio for zenith angles up to 50^0 as shown in Figure 6.12.

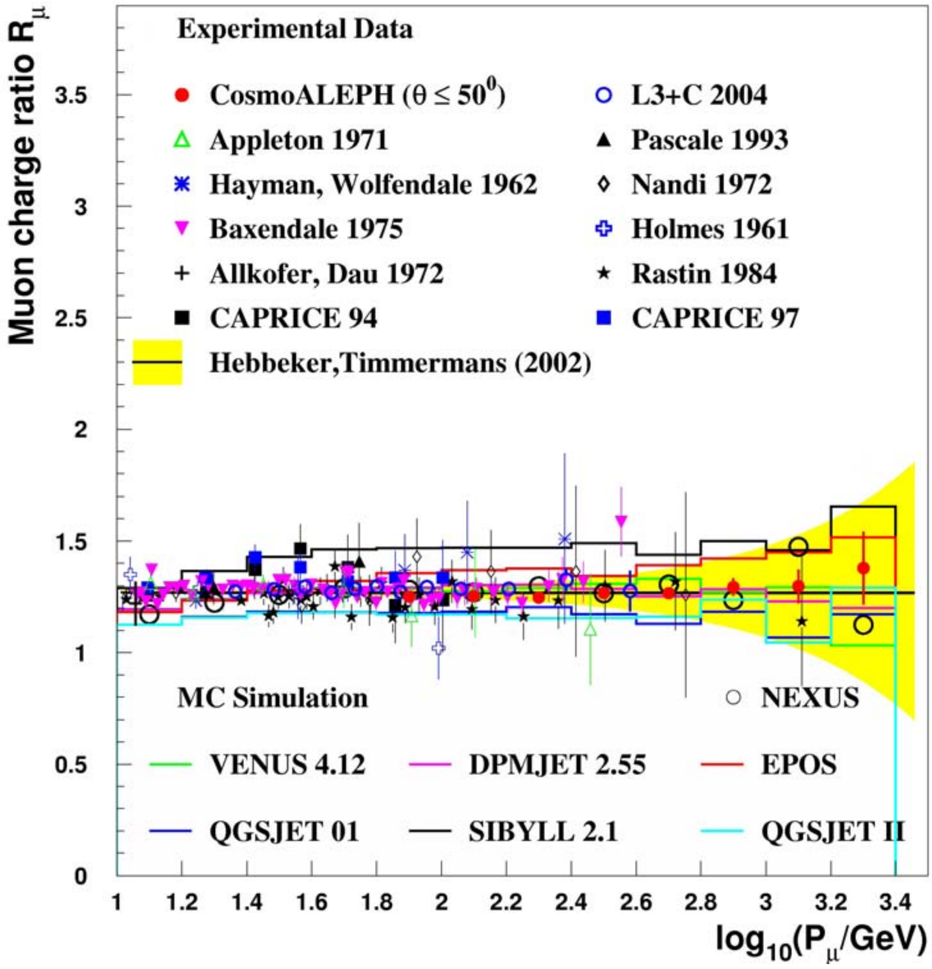

Figure 6.12: The charge ratio for inclined muons. A comparison is made with other data and also MC Simulations based on different hadronic interaction models

The muon charge ratio is shown here to be a sensitive observable for precision tests the hadronic interactions in EAS. Furthermore, this can be also used to test the models in the way they predict the production of muons in EAS [72]. As already observed in Section 2.1, atmospheric muons result mainly from the decay of the pions and kaons produced in the extensive air showers (EAS). The different predictions for kaon and pion production by the theoretical models therefore lead to variations in the production of muons. SIBYLL tends to overestimate the charge ratio of the muons.

Chapter 7

Conclusions and Outlook

Cosmic ray muon- and multi-muon events have been measured by the CosmoALEPH experiment using the ALEPH apparatus and some scintillator stations at CERN. This work concentrated on the measurement of the momentum spectrum and charge ratio of the cosmic ray muons from the dedicated CosmoALEPH data taking period of April 1999.

In oder to understand the performance of the CosmoALEPH experimental set-up and indeed the ALEPH appratus for the measurement of cosmic ray muons, detailed Monte Carlo simulations are carried out. The muon component of EAS, simulated using the CORSIKA program, is propagated through the overburden to the ALEPH apparatus. In the ALEPH appratus,the simulations are implemented using the GALEPH program, which includes the physics and technical description of the ALEPH apparatus.

The Monte Carlo simulations reproduce to a reasonable extent the measured zenith and azimuthal angle distributions. The measurements and the Monte Carlo simulations show a non-uniform zenith-azimuthal distributions due to the CosmoALEPH trigger conditions. The access shafts in the Pit 4, where ALEPH apparatus was located, result into a localised increase in the flux of cosmic ray muons with energies, E $\leq$ 200GeV.

The analysis of the simulated cosmic ray muon tracks in the ALEPH TPC, show that the central part of the TPC, i.e $|x| \leq 50$ cm and $20 \leq |z| \leq 200$cm provide the highest quality measurements. The track reconstruction efficiency for tracks in this fiducal area is $\sim$ 95% for momenta up P $\leq$ 1TeV/c and this value reduces to $\sim$ 72% for momenta P = 2TeV/C. The smearing of the reconstructed momenta for track in this fiducial area is within 10% for momenta P $\leq$ 1TeV/c and increases to $\sim$ 20% at P = 2TeV/c.

In addition, cosmic ray muon events pre-selected from the data taken during the e^+e^- data taking periods of 1999 and 2000, are used to determine the trigger efficiency of the HCAL. The analysis yields a value $\epsilon_{\text{HCAL}} = 85.5 \pm 0.6\%$ which is consistent with the documented value and previous findings.

Taking into account the muon energy losses in the overburden, the energies of the cosmic ray muons measured in ALEPH are extrapolated to the surface. This allows the calculation of the absolute muon flux and the charge ratio of the cosmic ray muons at sea level.

The results show that the momentum spectrum and the charge ratio are consistent with previous measurements. The charge ratio, though well described by Monte Carlo simulations, is however sensitive to the choice of hadronic interaction models. This work shows that the measured charge ratio for cosmic ray muons is indeed an observable in EAS that can be used for testing theoretical hadronic interaction models.

This is essential for the calculation of the other components of extensive air showers. The neutrino flux is closely related to the muon flux. Hence an accurate description of the muon flux enables a correspondingly accurate determination of the atmospheric neutrino flux. This is of special importance towards understanding the neutrino oscillations.

Therefore further Monte Carlo simulations should be carried out to calculate the muon spectrum and compare the results with the measurements of this work. This will provide a means to test the updated models for high energy interactions such as QGSJET-II [74] and NEXUS 3 [75] which have been included in the next version of CORSIKA[70, 76].

Acknowledgements

The CosmoALEPH collaboration gratefully acknowledges the help of the ALEPH collaboration, in particular the shift crew members of ALEPH, without whose support the data taking could not have been possible. The data analysis in CosmoALEPH experiment has been funded by the Deutsche Forschungsgemeinschaft under grant DFG/Gr/1796/1-3. I would like to sincerely thank the following individuals and organisations which have contributed to the success of this work,

- Prof. Dr. Claus Grupen for the opportunity to join his research group in Siegen and for the supervision of this work,
- the German Academic Exchange Service DAAD, for the academic scholarship provided,
- Prof. Dr. P. Buchholz and the computing group in Siegen for the smooth running of the computer cluster,
- Prof. Dr. Michael Schmelling for cross-checking the key steps in the analysis that guided me into the *central part of the TPC*,
- Dr. R. Engel for accepting to examine this work,
- Dr. D. Heck for providing the Figures 2.9 and 2.10,
- Dr. T. Pierog for the discussion on the EPOS model in the CORSIKA program,
- Dr. J. Hörandel and the KASCADE-GRANDE collaboration for the opportunity to take part in the calibration of their hadron calorimeter at CERN,
- Dr. A.-S. Müller for providing the Figure 1.1,

- Prof. Dr. Claus Grupen for the illustration *Master of the Muons*,
- Dr. Nigel Smale for carefully reading this work,
- CosmoALEPH collaboration for the constructive meetings,
- Max Planck Society through the Max Planck Institute for Nuclear Physics in Heidelberg for the invitation as a guest scientist,
- Wilhelm and Else Heraeus Foundation for the financial support to present the findings of this work during the Spring Meetings of the German Physical Society (2004 - 2007)
- Kenyatta University for the study leave,
- ... finally, all my friends and family for their kind support during the time of this study.

List of Figures

List of Tables

Chapter 8

Appendices

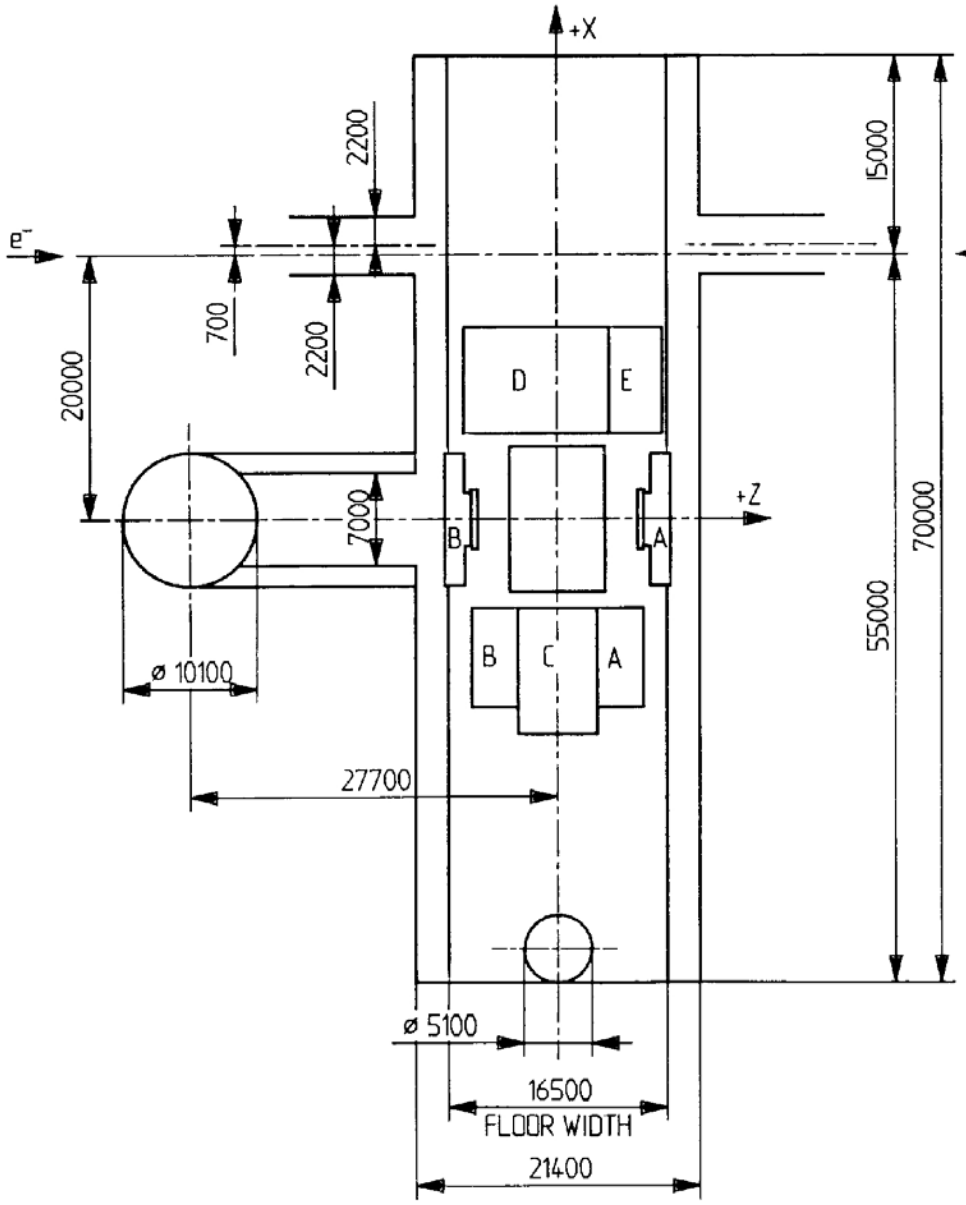

Figure 8.1: Dimensions of the experimental zone P4 where ALEPH was located [9]

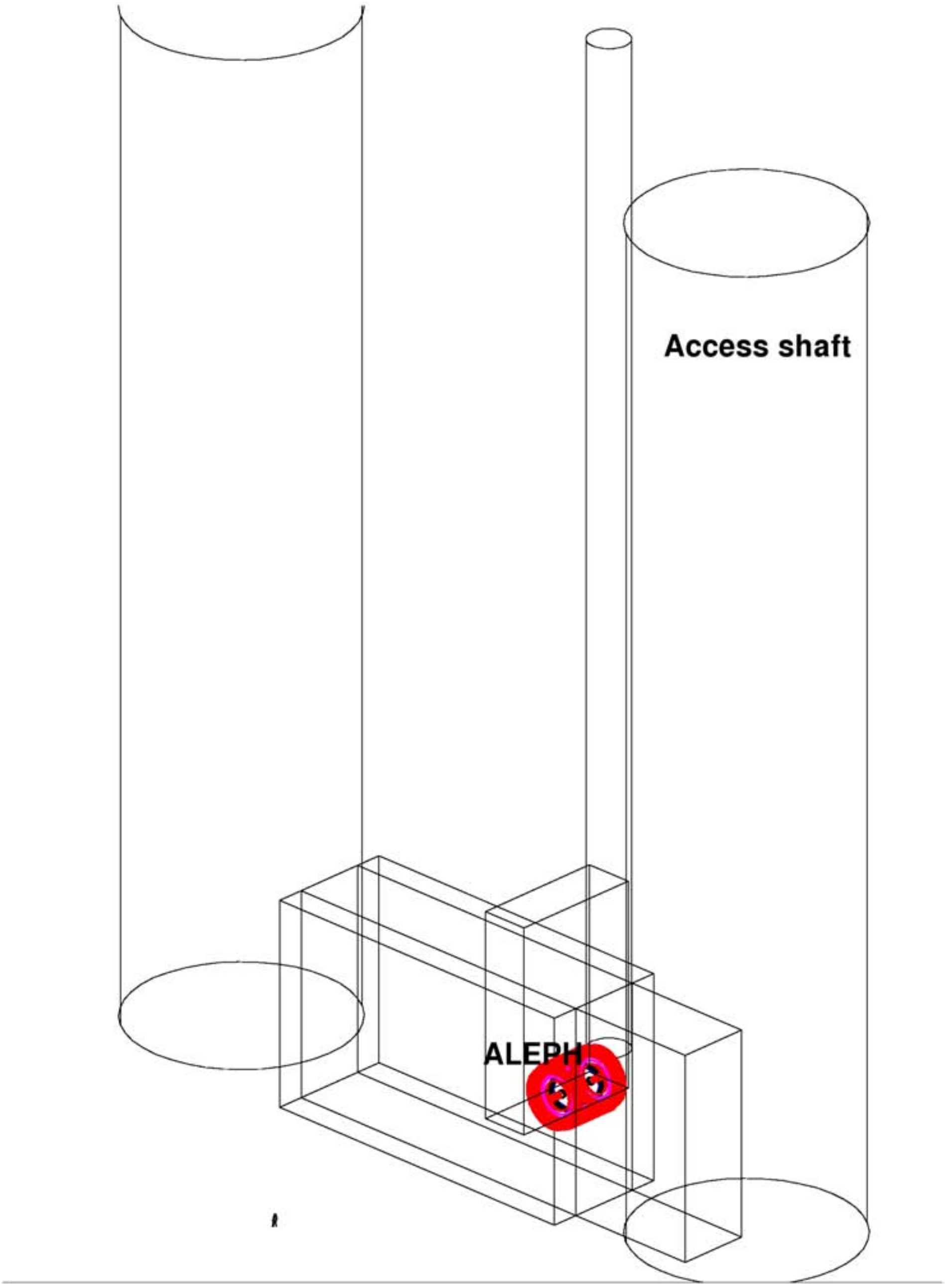

Figure 8.2: A schematic illustration of the ALEPH surroundings and the overburden implemented in GEANT.

A sample of the steering cards for EAS simulations using CORSIKA.

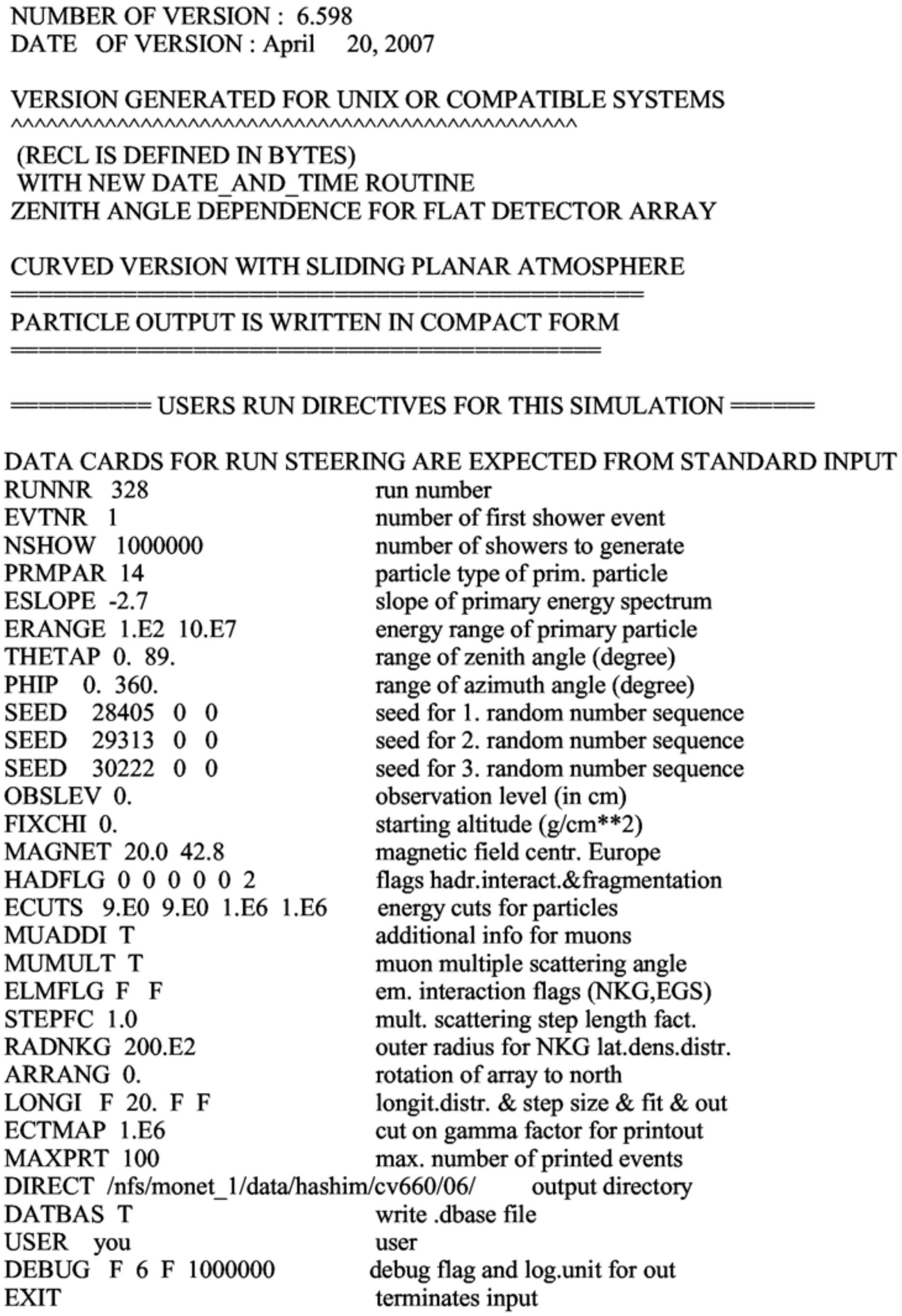

```
NUMBER OF VERSION :  6.598
DATE   OF VERSION : April     20, 2007

VERSION GENERATED FOR UNIX OR COMPATIBLE SYSTEMS
^^^^^^^^^^^^^^^^^^^^^^^^^^^^^^^^^^^^^^^^^^^^^^^^^^^^^^^^
 (RECL IS DEFINED IN BYTES)
 WITH NEW DATE_AND_TIME ROUTINE
ZENITH ANGLE DEPENDENCE FOR FLAT DETECTOR ARRAY

CURVED VERSION WITH SLIDING PLANAR ATMOSPHERE
==================================================
PARTICLE OUTPUT IS WRITTEN IN COMPACT FORM
==============================================

========== USERS RUN DIRECTIVES FOR THIS SIMULATION ======

DATA CARDS FOR RUN STEERING ARE EXPECTED FROM STANDARD INPUT
RUNNR  328                          run number
EVTNR  1                            number of first shower event
NSHOW  1000000                      number of showers to generate
PRMPAR  14                          particle type of prim. particle
ESLOPE  -2.7                        slope of primary energy spectrum
ERANGE  1.E2  10.E7                 energy range of primary particle
THETAP  0.  89.                     range of zenith angle (degree)
PHIP   0.  360.                     range of azimuth angle (degree)
SEED   28405  0  0                  seed for 1. random number sequence
SEED   29313  0  0                  seed for 2. random number sequence
SEED   30222  0  0                  seed for 3. random number sequence
OBSLEV  0.                          observation level (in cm)
FIXCHI  0.                          starting altitude (g/cm**2)
MAGNET  20.0  42.8                  magnetic field centr. Europe
HADFLG  0  0  0  0  0  2            flags hadr.interact.&fragmentation
ECUTS   9.E0  9.E0  1.E6  1.E6      energy cuts for particles
MUADDI  T                           additional info for muons
MUMULT  T                           muon multiple scattering angle
ELMFLG  F   F                       em. interaction flags (NKG,EGS)
STEPFC  1.0                         mult. scattering step length fact.
RADNKG  200.E2                      outer radius for NKG lat.dens.distr.
ARRANG  0.                          rotation of array to north
LONGI   F  20.  F  F                longit.distr. & step size & fit & out
ECTMAP  1.E6                        cut on gamma factor for printout
MAXPRT  100                         max. number of printed events
DIRECT  /nfs/monet_1/data/hashim/cv660/06/        output directory
DATBAS  T                           write .dbase file
USER    you                         user
DEBUG   F  6  F  1000000            debug flag and log.unit for out
EXIT                                terminates input
```

Bibliography

[1] V.F. Hess. Über beobachtungen der durchdringenden Strahlung bei sieben Freiballonfahren. *Phys. Zeitschr.* **13** (1912) 1084-1091

[2] C. Grupen. Astroparticle Physics. Springer-Verlag, Berlin Heidelberg, 2005. 441 p.

[3] R. Engel. Very high energy cosmic rays and their interactions. (2005) astro-ph/0504358

[4] A.-S. Müller. Erste Untersuchungen ausgedehnter Luftschauer im LEP-Tunnel. Diplomarbeit. Universität Mainz. 1996.

[5] H. Wachsmuth, Proposal to search for cosmic ray coincidences in the LEP-Detectors, Draft, 16 December 1993, CosmoLEP-Note 94.000.

[6] H. Drevermann. DALI event database.
$http : //aleph.web.cern.ch/aleph/dali/$

[7] H. Drevermann, D. Kuhn, B.S. Nilson. Event display: Can wee see what we want to see?. CERN/ECP 95-25. 19 October 1995.

[8] A. Ball, G. Bonvicini, C. Grupen et al., CERN/LEPC 94-10, LEPC/M, 1994, p 109

[9] ALEPH collaboration. Performance of the ALEPH detector at LEP. NIM A **360** (1995) 481-506.

[10] H. Wachsmuth. ALEPH goes cosmic (CosmoLEP and CosmoALEPH). Eds. C. Grupen, I. Hughes, J. Lynch and R. Settles. The ALEPH 'Experience'. (2005)

[11] D. Zimmermann et al. The cosmic muon spectrum and charge ratio in CosmoALEPH. NIM A **525** (2004) 141 - 143.

[12] N.O. Hashim, C. Grupen, S. Luitz, A. Mailov, F. Maciuc, A.-S. Müller, A.Putzer, H.-G. Sander, S. Schmeling, M. Schmelling, R. Tcaciuc, H. Wachsmuth, Th. Ziegler, K. Zuber. Momentum spectrum of cosmic muons at a depth of 320 mwe. *Proc. 29th International Cosmic Ray Conference* Pune (2005) **6** 13 -16.

[13] C. Grupen, N.O. Hashim, B. Jost, F. Maciuc, S. Luitz, A. Mailov, A.-S. Müller, A.Putzer, H.-G. Sander, S. Schmeling, M. Schmelling, R. Tcaciuc, H. Wachsmuth, Th. Ziegler, K. Zuber. Cosmic Ray Results from the CosmoALEPH Experiment. *Proc. XIV Int. Symp. on Very High Energy Cosmic Ray Interactions* (ISVHECRI 2006), Weihai, China.

[14] T. Hebbeker and C. Timmermans. A compilation of high energy atmospheric muon data at sea level. Astropart. Phys. **18** (2002) p 107-127.

[15] Original Version from S. Swordy, Chicago University.
http : //astroparticle.uchicago.edu/cosmic_ray_spectrum_picture.htm

[16] J. R. Hörandel. On the knee in the energy spectrum of cosmic rays. *Astroparticle Physics.* **19** (2003) 193-220

[17] J. R. Hörandel. Models of the knee in the energy spectrum of cosmic rays. *Astroparticle Physics* **21** (2004) 241 - 265.

[18] S.P. Swordy et al. The composition of cosmic rays at the knee. *Astroparticle Physics* **18** 129-150

[19] J. R. Hörandel. Overview on direct and indirect measurements of cosmic rays. Some thoughts on galactic cosmic rays and the knee. *Int. Journ. of Mod. Phys. A.* **20** (2005) 29

[20] T. Atoni et al. The cosmic ray experiment KASCADE. *Nucl. Instr. Meth.* **A 513** (2003) 429-675

[21] J. R. Hörandel. A review of experimental results at the knee. *Journal of Physics: Conference Series* **47** (2006) 41-50

[22] T. Stanev. High energy cosmic rays. Springer Verlag. (2004)

[23] T.K. Gaisser. Cosmic rays and particle physics. Cambridge University Press. Cambridge. (1990)

[24] H. Ulrich. Untersuchungen zum primären Energiespektrum der kosmischen Strahlung im PeV-Bereich mit dem KASCADE-Experiment. Dissertation. Universität Karlsruhe. Wissenschaftliche Berichte. FZKA 6952. Forschungszentrum Karlsruhe. Karlsruhe 2004.

[25] J. R. Hörandel, N. N. Kalmykov, A. V. Timokhin. The end of the galactic cosmic-ray energy spectrum - a phenomenological review. *Journal of Physics: Conference Series* **47** (2006) 132-141
astro-phy/0508015

[26] K. Greisen. *Phys. Rev. Lett.* **16** (1966)

[27] V. A. Kuzmin and G. T. Zatsepin. In *10th International Cosmic Ray Conference* **46** p617 (1968)

[28] T. Wibig and A. Wolfendale. At what particle energy do extragalactic cosmic rays start to predominate? *J. Phys. G: Nucl. Part. Phys.* **31** 255-264 (2005)

[29] J. H. Bahcall and E. Waxman. Has the GZK suppression been discovered?. *Phys. Lett. B* **556** 1 (2003) 1-6
hep-ph/0206217

[30] K-H. Kampert for the Pierre Auger Collaboration. The Pierre Auger Observatory - Status and prospects. *Nucl. Phys. B (Proc. Suppl.)* **151** (2006) 393-400

[31] J. Bluemer for the Pierre Auger Collaboration. Cosmic rays the highest energies and the Pierre Auger observatory. *J. Phys. G: Nucle. Part. Phys.* **29** (2003) 867-879

[32] B.G. Keilhauer. Investigation of atmospheric effects on the development of extensive air showers and their detection with the Pierre Auger Observatory. Ph.D. Thesis. Universität Karlsruhe. (2003)

[33] P. Mantsch. The Pierre Auger observatory. Progress and first results. *Proc. 29th International Cosmic Ray Conference* **10** (2005) 115

[34] C. Grupen. Electromagnetic interactions of high energy cosmic ray muons. *Fortschritte de Physik* **23** (1976) 127 - 209.

[35] V.A. Naumov, S.I. Sinegovsky and E.V. Bugaev. High-energy cosmic-ray muons under thick layers of matter. I. A method to solve transport equation. *hep-ph/9301263*

[36] S.I. Dutta, M.H. Reno, I.Sarcevic and D. Seckel. Propagation of muons and taus at high energies. *Phys. Rev. D.* **63** 094020.

[37] W. Lohmann, R. Kopp and R. Voss. Energy Loss of Muons in the Energy Range 1 - 10000 GeV. CERN 85-03.

[38] Particle Data Group. Review of Particle Physics. 24. Cosmic Rays. *Journal of Physics G - Nuclear and Particle Physics* 33 (2006) pg 245.

[39] L. I. Dorman. Cosmic Rays in the Earth's Atmosphere and Underground. Kluwer Academic Publishers. Dordrecht, The Netherlands. 2004. 855 p.

[40] D. Heck, J. Knapp, J.N. Capdevielle, G. Schatz, and T. Thouw, CORSIKA: A Monte Carlo code to simulate extensive air showers. FZKA 6019, Forschungszentrum Karlsruhe (1998). Available from
http://www-ik.fzk.de/corsika/physics_description/corsika_phys.html

[41] H. Fesefeldt. The simulation of hadronic showers: Physics and applications. **PITHA-85/02**. L3 Note 474. (1985)

[42] A. Fassò, A. Ferrari, S. Roesler, P.R. Sala, G. Battistoni, F. Cerutti, E. Gadioli, M.V. Garzelli, F. Ballarini, O.Ottolenghi, A. Empl and J. Ranft, *The physics models of FLUKA: status and recent developments*, Computing in High Energy and Nuclear Physics 2003 Conference (CHEP2003), La Jolla, CA (USA), March 24-28, 2003 (paper MOMT005); eConf C0303241 (2003); arXiv:hep-ph/0306267; http://www.fluka.org/references.html

[43] M. Bleicher, E. Zabrodin, C. Spieles, S. A. Bass, C. Ernst, S. Soff, L. Bravina, M. Belkacem, H. Weber and W. Greiner. Relativistic hadron-hadron collisions in the ultra-relativistic quantum molecular dynamics model. *J. Phys. G: Nucl. Part. Phys.* **25** (1999) 1859 - 1896.
S. A. Bass et al., *Prog. Part. Nucl. Phys.* **41** (1998) 225.

[44] J. Ranft. Dual parton model at cosmic ray energies. *Phys. Rev.* **D51** (1995) 64 - 84.
hep-ph/9911213, hep-ph/9911232

[45] H. J. Drescher, M. Hladik, S. Ostapchenko, T. Pierog and K. Werner. *Phys. Rep. 232* **350** (2001) 93.

[46] N.N. Kalmykov, S.S. Ostapchenko, and A.I. Pavlov, *Nucl. Phys. B (Proc. Suppl.)* **52B** (1997) 17
Phys. Rev. D **74** (2006) 014026

[47] S.S. Ostapchenko. *Nucl. Phys. B (Proc. Suppl.)* **151** (2006) 143, 147
Phys. Rev. D **74** (2006) 014026.

[48] R. Engel, T. K. Gaisser, P. Lipari and T. Stanev. Nucleus-nucleus collisions and inerpretation of cosmic-ray cascades. *Phy. Rev.* **D46** (1992) 5013- 5025.

[49] K. Werner. *Phys. Rep.* **232** (1993) 87.

[50] K. Werner, F. M. Liu and T. Pierog, *Phys. Rev. C* **74** (2006) 044902

[51] The ALEPH Collaboration. The ALEPH Handbook 1995. Vol. 1. Ed. C. Bowdery.

[52] V.Avati et al. CORAL. A cosmic ray experiment in and above the LHC tunnel. CERN/2001-003. SPSC/P321. CERN 2001.

[53] D. Colling and B. Wolf. First results of the ITC/TPC alignment from the 1991 cosmic run. 1991. ALEPH Note 91-65.

[54] S. Schmeling. CosmoALEPH Handbook. With Contributions from A.-S. Müller and H.Wachsmuth. CosmoALEPH 99-001. CERN.

[55] R. Tcaciuc. Lateral Distribution of Cosmic Ray Muons Underground: Results from the CosmoALEPH experiment. Ph.D. Thesis. (2006) Siegen University.

[56] CERN. GEANT 3.21. Detector description and simulation tool. CERN Library Long Write-up W5013, CERN, GENEVA. 1994.

[57] F.Ranjard. ALEPH Note 86-015.

[58] W.B. Atwood et al. Performance of the ALEPH time projection chamber. NIM A306. (1991) 446-458.

[59] J. Knobloch. JULIA Users and Programers Guide. (Version 2.41). 1990. ALEPH Note 90-115, SOFTWR 90-011.

[60] M.Schmelling. Numerische Methoden der Datenanalyse. Blockkurs Winter Semester 1997/1998. MPI-K. Heidelberg.

[61] M.Schmelling. The Method of Reduced Cross-Entropy. A General Approach to Unfold Probability Distributions. CERN Report. NIM A 340 (1994)

[62] E. V. Bugaev, A. Misaki, V. A. Naumov, T. S. Sinegovskaya, S. I. Sinegovsky and N. Takahashi. Atmospheric muon flux at sea level, underground and underwater. *Phys. Rev. D* **58** 054001 (1998)
hep-ph/9803488

[63] G. D'Agostini. A multidimensional unfolding method based on Bayes' theorem. NIM A **362** (1995) 487-498

[64] M. Schmelling et al. Studying extendend air showers with CosmoALEPH. First Arctic Workshop on Cosmic Ray Muons, Sodankylae, Finnland, April 24-29, (1999)

[65] H. Besier et al. Cosmic ray physics with the ALEPH detector. NIM A **454** (2000) 201-206

[66] C. Grupen et al. Measurements of the muon component of extensive air showers at 320 m.w.e. underground. NIM A **510** (2003) 190-193

[67] N.O. Hashim et al. Simulation of cosmic muon events in CosmoALEPH. In preparation.

[68] M. Schmelling. The CosmoALEPH Decoherence Curve. CosmoALEPH Note. (2006)

[69] J.R. Hörandel et al. Test of High Energy Hadronic Interaction Models using EAS Data. Proc. 26th Int. Cosmic Ray Conference, Salt Lake City **1** (1999) p 131 (and FZKA 6345, Forschungszentrum Karlsruhe (1999))

[70] D. Heck. The influence of hadronic interaction models on simulated air showers: A phenomenologic comparison. Lecture Notes. VIHKOS CORSIKA School 2005. May 29 - June 5 2005. Freudenstadt, Germany.

[71] P. Le Coultre, on behalf of the L3+C collaboration. L3+C - The atmospheric muon momentum spectrum. Nucl. Phys. B (Proc. Suppl.) **145** (2005) 136-140

[72] J. Wentz, A. F. Badea, A. Bercuci, H. Bozdog, I. M. Brancus, H-J. Mathes, M. Petcu, H. Rebel and B. Vulpescu The relevance of the muon charge ratio for the atmospheric neutrino anomaly. *J. Phys. G: Nucl. Part. Phys.* **27** (2001) 1699-1708.

[73] The L3 Collaboration. Measurement of the atmospheric muon spectrum from 20 to 3000 GeV. *Phys. Lett.* **B598** (2004) 15-32.
CERN-PH-EP-2004-023. June 1, (2004)

[74] S. Ostapchenko. Non-linear effects in high energy hadronic interactions. hep-ph/0501093 Jan. 2005.

[75] K. Werner et al. A new string model: NEXUS 3. hep-ph/0306151 June 2003

[76] D. Heck et al. Influence of low-energy hadronic interaction programs on air shower simulations with CORSIKA. Proc. 28th ICRC, Tsukuba, Japan, **1** (2003) 279

[77] D. Heck. Private Communication. (2006)